

REPORT DOCUMENTATION PAGE

Form Approved
OMB NO. 0704-0188

Public Reporting burden for this collection of information is estimated to average 1 hour per response, including the time for reviewing instructions, searching existing data sources, gathering and maintaining the data needed, and completing and reviewing the collection of information. Send comment regarding this burden estimates or any other aspect of this collection of information, including suggestions for reducing this burden, to Washington Headquarters Services, Directorate for Information Operations and Reports, 1215 Jefferson Davis Highway, Suite 1204, Arlington, VA 22202-4302, and to the Office of Management and Budget, Paperwork Reduction Project (0704-0188), Washington, DC 20503.

| | | | |
|---|---|--|----------------------------------|
| 1. AGENCY USE ONLY (Leave Blank) | 2. REPORT DATE 1 Dec 03 | 3. REPORT TYPE AND DATES COVERED Final Progress Report: 1 July 00 – 31 Aug 03 | |
| 4. TITLE AND SUBTITLE Electronically Integrated Active Compliant Transmission (ACT) Actuation Technologies Proof-of-Concept Investigation of Active Velcro for Smart Attachment Mechanisms | | 5. FUNDING NUMBERS 6 – DAAD 19-00-1-0441 | |
| 6. AUTHOR(S) Diann Brei, Douglas Lindner, Mary Frecker, Chris LaVigna, Joe Clement | | | |
| 7. PERFORMING ORGANIZATION NAME(S) AND ADDRESS(ES) Mechanical Engineering Department, University of Michigan Ann Arbor, MI 48109-2125 | | 8. PERFORMING ORGANIZATION REPORT NUMBER F003271 | |
| 9. SPONSORING / MONITORING AGENCY NAME(S) AND ADDRESS(ES) U. S. Army Research Office P.O. Box 12211 Research Triangle Park, NC 27709-2211 | | 10. SPONSORING / MONITORING AGENCY REPORT NUMBER 41377.1 - EG | |
| 11. SUPPLEMENTARY NOTES The views, opinions and/or findings contained in this report are those of the author(s) and should not be construed as an official Department of the Army position, policy or decision, unless so designated by other documentation. | | | |
| 12 a. DISTRIBUTION / AVAILABILITY STATEMENT Approved for public release; distribution unlimited. | | 12 b. DISTRIBUTION CODE | |
| 13. ABSTRACT (Maximum 200 words) This report provides a summary of the motivation, methodology and research results for two different projects supported under this effort. In <i>Electrically integrated active compliant transmission (ACT) Actuation Technologies</i> two different actuation approaches were developed, modeled, fabricated and experimentally validated: 1) a d31-approach based on the Recurve architecture that generates higher forces and 2) a d33-approach based upon a compliant mechanism that provides more amplified strain. A first-generation power amplifier was designed that efficiently swaps energy allowing low voltage batteries to produce high voltage drive signals. Both piezoceramic actuation systems were integrated into the INertially STAbilized Rifle (INSTAR) to eliminate aiming errors by stabilizing the barrel assembly providing a significant advancement in small arms. In the second project, <i>Proof-of-Concept Investigation of Active Velcro Autonomous Docking of Micro- and Nano-Satellites</i> , a new connection methodology, Smart Attachment Mechanism (SAM) technology, was invented, modeled and experimentally characterized that possesses the ability to actively connect two surfaces (engagement, retention, release) and effect relative planar motion between them (translation, rotation). This work laid the necessary foundation for further development of this unique paradigm which is useful for any unstable environment (space, fluidic, moving, vibration, etc) where active connection and motion is simultaneously required. | | | |
| 14. SUBJECT TERMS Actuator, Piezoelectric, Shape Memory Alloy, Smart Attachment Mechanism, Fastener, Velcro, Rifle, INSTAR, Compliant Mechanism, Recurve, Piezoceramic, Sniper, Marksman, Expert | | 15. NUMBER OF PAGES 100 | |
| | | 16. PRICE CODE | |
| 17. SECURITY CLASSIFICATION OR REPORT UNCLASSIFIED | 18. SECURITY CLASSIFICATION ON THIS PAGE UNCLASSIFIED | 19. SECURITY CLASSIFICATION OF ABSTRACT UNCLASSIFIED | 20. LIMITATION OF ABSTRACT UL |

NSN 7540-01-280-5500

Standard Form 298 (Rev.2-89)
Prescribed by ANSI Std. Z39-18
298-102

FORWARD

This report provides a summary of the motivation, methodology and research results for two different projects supported under this effort: Electrically integrated active compliant transmission (ACT) Actuation Technologies and Proof-of-Concept Investigation of Active Velcro Autonomous Docking of Micro- and Nano-Satellites.

Electrically integrated active compliant transmission (ACT) Actuation Technologies

The aim of this project was the synergistic development of complete piezoelectric actuation systems with integrated electronic drivers, material transduction and Active Compliant Transmissions (ACT). The goal was to achieve a compact lightweight actuation family capable of large strokes concurrent with high forces, while maintaining the fast response and large bandwidth of the piezoelectrics, thereby attaining high power density and specific work. In addition, this actuation family would come with high efficiency switching power electronic drivers that minimize the size of the actuation package while requiring minimal energy usage. As a means to demonstrate the usefulness of these type of actuators, an INertially STAbilized Rifle (INSTAR) was developed that eliminates aiming error sources by stabilizing the barrel assembly (2 DOF), effectively compensating for small user induced disturbances. Two very different actuation approaches were developed, modeled, fabricated and experimentally validated within the INSTAR demonstration platform: 1) a d31 approach based on the Recurve architecture with focus on generating higher forces than is common for d31 actuators and 2) a d33 approach based upon a compliant mechanism designed using topology optimization with focus on providing more amplified strain than is common for d33 actuators. Both approaches were successful in meeting the INSTAR requirements each with their own advantages and disadvantages.

Proof-of-Concept Investigation of Active Velcro Autonomous Docking of Micro- and Nano-Satellites.

This research presents a paradigm shift in connection methodologies which are typically passive. The specific goal of this research was to create and demonstrate a fundamental Smart Attachment Mechanism (SAM) technology that possesses the ability to actively connect two surfaces (engagement, retention, release) and effect relative planar motion between them (translation, rotation). A snap-fit design analogous to Velcro was developed with a densely distributed array of SMA actuated compliant mechanism for positioning. “Active Velcro” is a general technology which can be applied at different scales (micro- to macro-) for different required performance by tailoring a multitude of geometric and material design variables. An extensive modeling effort was performed and experimentally validated for the basic operations (engagement, retention/release, positioning) to provide synthesis and analysis tools. Several different scaled prototypes were fabricated and experimentally characterized successfully demonstrating usable engagement, retention and positioning forces and feasible speeds. This work laid the necessary foundation for further development of this unique paradigm which is useful for any unstable environment (space, fluidic, moving, vibration, etc) where active connection and motion is simultaneously required.

TABLE OF CONTENTS

| | <u>Page</u> |
|--|-------------|
| FORWARD..... | I |
| TABLE OF CONTENTS | II |
| LIST OF ILLUSTRATIONS AND TABLES, SECTION 1 | V |
| LIST OF ILLUSTRATIONS AND TABLES, SECTION 2 | VII |
| SECTION 1. ELECTRICALLY INTEGRATED ACTIVE COMPLIANT TRANSMISSION (ACT) ACTUATION TECHNOLOGIES | 1 |
| 1.1. INTRODUCTION | 1 |
| 1.1.1. Motivation | 1 |
| 1.1.2. Research Overview..... | 2 |
| 1.2. INSTAR..... | 4 |
| 1.2.1. INSTAR System Description..... | 5 |
| 1.2.2. INSTAR Actuation Specifications | 6 |
| 1.2.3. Actuation Downselection Overview..... | 8 |
| 1.3. INTERNALLY LEVERAGED d31 MODE ACTUATION..... | 9 |
| 1.3.1. INSTAR Recurve Design Synthesis..... | 10 |
| 1.3.2. Loss Mechanism Study | 11 |
| 1.3.3. Recurve Prototype..... | 13 |
| 1.3.4. Dynamic Benchtop Characterization | 14 |
| 1.3.5. Quasi-static Benchtop Characterization | 14 |
| 1.4. EXTERNALLY LEVERAGED d33 MODE ACTUATION..... | 16 |
| 1.4.1. Design Synthesis | 16 |
| 1.4.2. Material Study | 18 |
| 1.4.3. Bonding Layer Study | 19 |
| 1.4.4. d33 Prototype..... | 20 |
| 1.4.5. Dynamic Benchtop Characterization | 21 |
| 1.4.6. Quasi-static Benchtop Characterization | 22 |
| 1.4.7. Actuation Systems Discussion | 23 |
| 1.5. ELECTRONIC SYSTEM | 23 |
| 1.5.1. Power Electronic Architecture..... | 23 |

| | |
|--|-----------|
| 1.5.2. Benchtop Characterization | 24 |
| 1.5.3. Energy Study | 25 |
| 1.6. INSTAR DEMONSTRATION..... | 26 |
| 1.7. CONCLUSIONS | 28 |
| 1.8. REFERENCES, SECTION 1..... | 31 |
| SECTION 2. PROOF-OF-CONCEPT INVESTIGATION OF ACTIVE VELCRO FOR SMART ATTACHMENT MECHANISMS..... | 33 |
| 2.1. INTRODUCTION | 33 |
| 2.1.1. Motivation..... | 33 |
| 2.1.2. Research Goals and Objectives..... | 36 |
| 2.1.3. Report Overview | 36 |
| 2.2. ACTIVE VELCRO DESIGN AND OPERATION | 37 |
| 2.2.1. Active Velcro Architecture..... | 38 |
| 2.2.1.1. Connection Topology..... | 39 |
| 2.2.1.2. Surface Pattern | 40 |
| 2.2.1.3. Actuation System | 43 |
| 2.2.2. Active Velcro Operation | 43 |
| 2.2.2.1. Gait 1..... | 44 |
| 2.2.2.2. Gait 2..... | 45 |
| 2.2.2.3. Advanced Multi-Post Functionality | 45 |
| 2.2.2.3.1 Rotation Generation | 46 |
| 2.2.2.3.2 Increased Positioning Speed..... | 47 |
| 2.2.2.3.3 Increased Reliability | 47 |
| 2.3. OPERATIONAL MODELS AND VALIDATION..... | 47 |
| 2.3.1. General Model Structure..... | 48 |
| 2.3.1.1. Unassembled Stiffness Matrix | 50 |
| 2.3.1.2. Compatibility Matrix..... | 51 |
| 2.3.2. Engagement Model..... | 52 |
| 2.3.2.1. Loading Conditions | 53 |
| 2.3.2.2. Final Engagement Model | 54 |
| 2.3.3. Retention Model | 55 |
| 2.3.3.1. Loading Conditions | 56 |
| 2.3.3.2. Final Retention Model..... | 56 |
| 2.3.4. Multi-cell Positioning Model | 58 |

| | |
|---|----|
| 2.3.4.1. Loading Conditions | 59 |
| 2.3.4.2. Final Positioning Model | 61 |
| 2.3.5. Experimental Model Validation..... | 61 |
| 2.3.5.1. Test Samples..... | 62 |
| 2.3.5.2. Experimental Procedure | 63 |
| 2.3.5.3. Single-Cell Behavior Experimental Results | 64 |
| 2.3.5.4. Engagement Experimental Results | 65 |
| 2.3.5.5. Retention Experimental Results..... | 66 |
| 2.3.5.6. Positioning Force Experimental Results..... | 68 |
| 2.4. PROOF OF CONCEPT DEMONSTRATION AND EVALUATION..... | 69 |
| 2.4.1. Pattern Refinement | 69 |
| 2.4.2. Large-Scale Prototype Test Bed..... | 71 |
| 2.4.2.1. Large-Scale Prototype Fabrication | 71 |
| 2.4.2.2. Procedure..... | 73 |
| 2.4.2.3. Translation Experimental Results..... | 74 |
| 2.4.2.4. Rotation Experimental Results..... | 74 |
| 2.4.2.5. Discussion | 74 |
| 2.4.3. Reduced-Scale Unified-Host Test Bed..... | 75 |
| 2.4.3.1. Reduced-Scale Prototype Fabrication | 75 |
| 2.4.3.2. BASIC Stamp Control System | 76 |
| 2.4.3.3. Experimental Procedure and Results | 80 |
| 2.4.3.4. Discussion | 81 |
| 2.5. CONCLUSIONS | 83 |
| 2.6. REFERENCES, SECTION 2..... | 85 |
| SECTION 3. PUBLICATIONS, TECHNICAL REPORTS, AND INVENTIONS..... | 88 |
| SECTION 4. SCIENTIFIC PERSONNEL..... | 90 |

LIST OF ILLUSTRATIONS AND TABLES, SECTION 1

Section 1: Electrically Integrated Active Compliant Transmission (ACT) Actuation Technologies

| <u>List of Figures</u> | <u>Page</u> |
|---|-------------|
| Figure 1: INSTAR Design | 5 |
| Figure 2: INSTAR Barrel Movement | 6 |
| Figure 3: INSTAR Requirements..... | 6 |
| Figure 4: INSTAR System Model..... | 7 |
| Figure 5: Required INSTAR Actuator Force-Deflection Performance..... | 8 |
| Figure 6: Recurve Actuation Architecture and Operation | 9 |
| Figure 7: Recurve Conventions | 10 |
| Figure 8: End Cap Effect on Stiffness Experimental Study | 11 |
| Figure 9: Segmentation/Layering Effect on Stiffness Experimental Study..... | 12 |
| Figure 10: Recurve Prototype for INSTAR..... | 13 |
| Figure 11: Dynamic Test Results for Recurve Actuator | 14 |
| Figure 12: Quasi-Static Experimental Results for Recurve Actuator | 15 |
| Figure 13: INSTAR Design Problem..... | 16 |
| Figure 14: Discretized Design Domain..... | 17 |
| Figure 15: Optimal Topology Solution (a), and Interpretation (b) | 18 |
| Figure 16: Symmetric Design Displacement During Positive and Negative Actuation (deformations magnified 25 times) | 19 |
| Figure 17: Solid Model with Bonding Layers | 19 |
| Figure 18: d33 Prototype Actuator | 20 |
| Figure 19: Dynamic Test Results for d33 Actuator | 21 |
| Figure 20: Quasi-Static Experimental Results for d33 Actuator | 22 |
| Figure 21: Block Diagram for Power Electronics | 24 |

| | |
|--|-----------|
| Figure 22: Prototype of the Power Electronics for INSTAR | 24 |
| Figure 23: Switching Amplifier Output Voltage..... | 25 |
| Figure 24: Switching Amplifier Frequency Response | 26 |
| Figure 25: Power Loss | 26 |
| Figure 26: Number of Shots/Battery Comparison of Switching and Linear Amplifier | 27 |
| Figure 27: Prototype 7.62 mm Rifle with Actuator Mounted in Housing | 28 |
| Figure 28: INSTAR Prototype Test Results for Recurve Actuator | 29 |
| Figure 29: INSTAR Prototype Test Results for d33 Mode Actuator..... | 29 |

| <u>List of Tables</u> | <u>Page</u> |
|---|--------------------|
| Table 1.1: INSTAR Actuator Requirements | 7 |
| Table 1.2: Passive Material Variation Study..... | 18 |
| Table 1.3: FEA Results with Bonding Layers | 20 |

LIST OF ILLUSTRATIONS AND TABLES, SECTION 2

Section 2: Proof-of-Concept Investigation of Active Velcro for Smart Attachment Mechanisms

| <u>List of Figures</u> | <u>Page</u> |
|--|-------------|
| Figure 2.1: Active Velcro System Overview | 39 |
| Figure 2.2: Connection Topology Requirements | 40 |
| Figure 2.3: Sample Connection Topology | 41 |
| Figure 2.4: Linear vs. Saw-toothed Motion | 41 |
| Figure 2.5: Hexagonal Repeat Unit | 42 |
| Figure 2.6: Cell Connections..... | 43 |
| Figure 2.7: Single-Cell Grasping Action | 44 |
| Figure 2.8: Local Prong Operation: Gait 1 | 45 |
| Figure 2.9: Local Prong Operation: Gait 2 | 46 |
| Figure 2.10: Variable Dimensional Parameters | 49 |
| Figure 2.11: Global Displacements vs. Local Deformations | 49 |
| Figure 2.12: Engagement Phases | 52 |
| Figure 2.13: Retention | 56 |
| Figure 2.14: Positioning Force | 61 |
| Figure 2.15: Experimental Test Sample Designs | 62 |
| Figure 2.16: Surface Finish Improvement..... | 63 |
| Figure 2.17: Experimental Test Setup | 63 |
| Figure 2.18 Experimental Input/Output Parameters | 64 |
| Figure 2.19: Single Cell Kinematics and Stiffness at the Actuation Triangle Experimental Results..... | 65 |
| Figure 2.20: Engagement Force Experimental Results | 66 |

| | |
|--|-----------|
| Figure 2.21: Retention Force Experimental Results..... | 67 |
| Figure 2.22: Positioning Force Experimental Results | 68 |
| Figure 2.23: Interference During Translation..... | 70 |
| Figure 2.24: Interference During Rotation..... | 70 |
| Figure 2.25: Sample Results of Pattern Refinement..... | 72 |
| Figure 2.26: Large-Scale Prototype..... | 73 |
| Figure 2.27: Reduced-Scale Test Bed..... | 76 |
| Figure 2.28: Demonstration Guest Surfaces..... | 77 |
| Figure 2.29: Control Unit..... | 78 |
| Figure 2.30: Control System Flow Chart..... | 79 |
| Figure 2.31: Preferred Goal Orientations | 81 |
| Figure 2.31: Refined Host Surface Topology | 83 |

| <u>List of Tables</u> | <u>Page</u> |
|---|--------------------|
| Table 2.1: Relevant State of the Art Distributive Manipulation Systems | 35 |
| Table 2.2: Performance Metrics for the Large-Scale Test Bed | 74 |
| Table 2.3: Performance Metrics for the Reduced-Scale Test Bed..... | 80 |
| Table 2.4: Host Surface Refinement Results | 84 |

SECTION 1. ELECTRICALLY INTEGRATED ACTIVE COMPLIANT TRANSMISSION (ACT) ACTUATION TECHNOLOGIES

Investigators:

Diann Brei, PI, Associate Professor, Mechanical Engineering Department, University of Michigan, Ann Arbor, MI 48109-2125

Douglas K Lindner, Associate Professor, Bradley Department of Electrical and Computer Engineering, Virginia Polytechnic Institute and State University, Blacksburg, VA, 24061

Mary Frecker, Associate Professor, Department of Mechanical and Nuclear Engineering, Pennsylvania State University, University Park, PA, 16802

Chris LaVigna, President, TechnoSciences, Inc., Lanham, MD, 20706

1.1. INTRODUCTION

1.1.1. Motivation

Good marksmanship is well recognized by the military as essential for the success of modern infantry forces in combat. It is indispensable for effective infantry operations in urban environments, believed by most to be the most likely places in which future U.S. military operations are to occur for (Doctrine for Joint Urban Operations, 2002). Combat in these urban warfare environments place high demands on accurate fire due to the intermingling of civilians and combatants, the close proximity of enemy forces, and the ever varying urban landscape. In such environments, good marksmanship skills significantly improve a soldier's survivability. This was one of the most important lessons learned from the battle in Mogadishu, Somalia, in 1993, where well-aimed, accurate fire enabled a small, highly trained U.S. force to hold off thousands of Somali militiamen during urban combat operations there (David, 1995). It is important to note that the soldiers who participated in the Somalia operation were elite forces including elements of the Delta Force, Seals and Army 10th Mountain division. Their considerable marksmanship skills significantly exceed those of the average infantry soldier.

The U.S. Army has long recognized the importance of good marksmanship skills as they relate to soldier survivability and has established Marksmanship training and Qualification programs to teach these skills to the infantry soldier. However, attaining and maintaining proficiency in marksmanship is a costly, resource and time consuming process with varying degrees of effectiveness. Even with the extensive training, only a small fraction of soldiers are able to attain the Expert, or highest level of marksmanship qualification. It has been shown that in actual combat situations (which cannot be effectively simulated in training) even for the best trained and talented shooters, it is often difficult to perform the fundamentals inherent in good

marksmanship techniques: assuming and maintaining a steady position, aiming, controlling breathing and executing a proper trigger squeeze (FM3-22.9 Rifle Marksmanship, 2003; FM 23-10 Sniper Training, 1994).

The primary purpose for each of these techniques is to enable the shooter to control the gun point of aim and minimize its motion relative to the intended target so as to maximize the probability of round impact on that target. The steady position technique teaches the shooter to assume a conformable steady position (prone is steadiest) with muscles relaxed and body preferably braced against supports such as sandbags, logs, stumps, etc. The aiming technique teaches the shooter to align the rifle with the target. And both the breathing and trigger squeeze techniques teach the shooter when and how to squeeze the trigger relative to the breathing cycle in order to minimize upset of the gun aim.

Yet in combat situations these fundamental techniques cannot always be executed. For example, terrain and time frame of the immediate circumstance often dictate the choice of shooting position including the availability of steadyng supports. Because of this, the shooter does not always have the time or luxury of choosing a steady prone position with sandbag support for the weapon. He or she must react to the situation and assume the most expedient position from which to deliver fire. Often this means employing a position that is not optimal from a steadyng standpoint, making it more difficult and time consuming to steady the rifle for fire. Studies have also shown that the heart beat of a soldier during combat can reach upwards to 300 beats per minute making it difficult to carry through with proper trigger squeeze techniques.

The U.S. Army has identified a deficiency in marksmanship at the squad level, in particular the ability to engage targets between the maximum range of the average soldier, 300 meters, and the typical range of trained snipers, 600 meters and beyond (FM3-22.9 Rifle Marksmanship, 2003). To address this need the U.S. Army has developed the Squad Designated Marksman Program (SDM). The primary mission of the SDM is to deploy as a member of the rifle squad. The SDM is not a squad sniper but fires and maneuvers with his squad and performs all of the duties of a rifleman. His/her secondary mission is to engage targets from 300-500 meters with effective, well aimed fires using a standard weapon and ammunition. The SDM may not have an optic sight and therefore, must possess a significant mastery of marksmanship. In order to meet the personnel needs arising from placing an SDM in each squad, a significant number of soldiers highly skilled and trained in marksmanship will be required.

1.1.2. Research Overview

In order to address these issues there exists a need to improve the shooting performance of these lesser skilled soldiers by methods other than the standard formal marksmanship training. One concept is to improve the weapon to be easier to control and accurately aim in adverse conditions. In this research effort, an INertially STabilized Rifle (INSTAR) was developed that incorporates an active suspension that eliminates aiming error sources by stabilizing the barrel assembly, effectively compensating for the small user induced disturbances. INSTAR operates similar to a video camera with a simple feedback control system that rejects any tracking commands at lower frequencies and compensates for the jitter disturbances at higher frequencies. This revolutionary gun system has the potential to improve aiming and hit performance of all skill levels (expert, sharpshooter, and marksman, etc.), thereby providing engagement of targets

at greater ranges. Lesser skilled and trained shooters will be able to meet mission requirements previously assigned to higher skilled/trained personnel leading to greater soldier survivability with less ammunition expended, to reduced training requirements and to warfighting with less collateral damage.

The critical design driver for the INSTAR active suspension is the “complete” actuation system that includes not only the actuator but also the related driving electronics and power supply. This was the focus of this research. The actuation system presents many engineering challenges which are faced by many other applications today. For example, the space is very constrained and eliminates conventional technology. In INSTAR, the only space available for the full actuation system is the base and stock of the rifle which is awkward and small. As with several applications, the overall specific work, required precision and frequency response is within the range of piezoceramics, unfortunately the force and stroke required is moderate and out of the range of off-the-shelf actuation systems calling for a custom architecture. While the drive electronics for any piezoelectric actuator requires almost zero real power, piezoceramics require a large amount of reactive power with high voltages due to the capacitive nature of the material. Linear power amplifiers have a good frequency response and no voltage noise, but they are usually very bulky and have low efficiency because they dissipate the regenerative power as heat. Therefore, an approach based upon switching power electronics was adopted. Obviously, any increase in the weight should be minimal. This demands an efficient transfer of energy through the system, initiating from the power source, modulated by the electronics that provide it to the smart material that transforms it via the actuation architecture into controlled displacements of the barrel. While the energy source (battery) must be small and light to minimize the weight for the soldier, at the same time the system must have an acceptable lifetime.

Since space and energy cannot be wasted, a synergistic design of the complete actuation system is essential. This research effort began with identifying the primary specifications for INSTAR via a simple analytical model for the suspension system which set the actuation requirements. The selection of an amplification scheme is clear when either high forces or high displacements are required, but it is much more difficult when both are simultaneously required. Thus, two very different actuation approaches were explored within the INSTAR demonstration platform: 1) a d31 approach based on the Recurve architecture with focus on generating higher forces than is common for d31 actuators and 2) a d33 approach based upon a compliant mechanism designed using topology optimization with focus on providing more amplified strain than is common for d33 actuators. Concurrently, electronic driving circuit especially suitable for low input DC bus, high-voltage PZT actuators was created based upon a two-stage circuit including a flyback circuit for the first stage and a half-bridge circuit as the second stage. Both circuits are switching circuits that use PWM technology. Each type of actuator scheme was developed and experimentally characterized on the benchtop. To confirm the actuation authority, range-of-motion experiments were conducted on a full-scale, 1 degree-of-freedom INSTAR prototype incorporating in both actuators. Even though the INSTAR requirements were challenging, both approaches were successful in meeting the INSTAR requirements, yet each had its own advantages and disadvantages which will need to be considered when applied to other applications. This report gives a summary of the development and proof-of-concept experimental characterization of INSTAR with focus on the actuation system.

1.2. INSTAR

It is estimated by the Army that 90% of the errors contributing to a shooter missing his or her intended target in range qualification can be attributed to aiming errors which include including shooter induced disturbances, inaccurate range and wind estimation, and weapon anomalies. In these non-combat situations, shooter induced disturbances account for approximately 20% of this error. Further complicating the shooting task is that, when subjected to the stress of combat, the shooting accuracy of all soldiers degrades. According to U.S. Army Small Arms Program personnel, the levels of shooter induced disturbances in combat situations are typically at least an order of magnitude higher than those seen in non-combat situations (FM3-22.9 Rifle Marksmanship, 2003). This is echoed by U.S. Army Joint Service Small Arms Program (JSSAP) program manager Steve Mango when describing the effects of combat stress on the soldier's performance using the M16, "The M16 is a very accurate weapon. However, when it is placed in the hands of an individual under combat-stress conditions, its performance is reduced dramatically."

In combat, physiological responses with direct effect on gun aiming performance such as heart beat, respiration, and muscle jerk motion interfere with a soldier's ability to keep the gun aimed on target. For example, studies have shown that the heart rate of a soldier in combat can reach upwards of 300 beats per minute, well above the typical maximum of approximately 200 beats per minute experienced by athletes in major competitions such as the Olympics (FM3-22.9 Rifle Marksmanship, 2003). In order to attain accurate fire from small arms weapons, such as assault or sniper rifles, the shooter must maintain extremely precise control over the weapon point of aim during the aiming and firing process. For example, to hit a standard military man-sized target silhouette at 300 m, the shooter must control the deviation in the gun angular orientation (both elevation and azimuth angles) to within ± 0.83 mrad ($\pm 0.09^\circ$) of the nominal orientation (rifle aim point at the center of target). Of course, in combat enemy forces are usually concealed and present a much smaller target than the standard silhouette shape thereby requiring substantially more precise control of weapon for the round to hit the target.

Reducing or eliminating the shooter induced disturbances, especially in combat situations, can have a substantial impact on the accuracy of fire. Despite all the advances in technology over the past century, there have been very little changes introduced into military rifles to address this problem. The INSTAR system in this research is a technology solution that is applicable to small arms systems such as the U.S. Army M24 Sniper Rifle System and the M16Ax series of rifles. It provides an alternative to the training based approach and enables an average shooter to improve shot accuracy to the next level through the use of active stabilization technology. Because the proposed INSTAR system employs active stabilization to reduce or eliminate shooter induced body muscles motions transfer to the gun barrel, a steady position is not as critical to deliver accurate fire. This means that by using the INSTAR system, the shooter has many more options for the choice of body position and can react to deliver fire quicker in response to the ever changing action inherent in combat. Furthermore, the use of the INSTAR system can help to mitigate the effects of both improper breathing and improper trigger squeeze techniques which contribute to upset of the gun aim prior to firing. The use of INSTAR technology throughout infantry units would result in a significant improvement in overall marksmanship and better enable them to meet mission requirements previously assigned to higher skilled or trained personnel and increase soldier survivability.

1.2.1. INSTAR System Description

The goal of INSTAR is to enable precision shooting even under combat stress by decoupling shooter-induced disturbances from the gun “point of aim”. To accomplish this, the barrel-action-scope assembly is inertially stabilized via an active suspension with integrated actuators and sensors enabling controlled motion of the gun barrel muzzle. The 7.62 mm tactical rifle, Figure 1, is outfitted with a two dof system controlled by three actuators: two opposing actuators that move the barrel in the azimuth direction and one actuator with return springs used to move the barrel in the elevation direction while keeping the line of sight clear. The control system is a simple closed-loop feedback controller, similar in concept to that utilized in video cameras. Sensors are used to detect the shooter-induced disturbances and the controller separates in the frequency domain between the desired tracking commands (lower in frequency – subhertz), which are left unaffected and the jitter disturbances (higher in frequencies – approximately 1 to 10 Hz), which are to be compensated for by the controller.

While the sensor and controller technology is readily available, the actuation system required for the active stabilization was not and needed to be custom designed. To compensate for any additional weight from the active stabilization system, the normally heavy barrel was exchanged for a lightweight composite barrel providing 2 kg for the actuation system. The actuator must provide stroke perpendicular to the barrel axis as shown in Figure 2. As such the actuator must fit into directly in the stock along the barrel at the point of motion, giving an upper constraint on the package of 140 mm x 25 mm x 30 mm. This is an awkward package with the shortest distance along the actuation path. In contrast, the electronics (battery, power amplifiers, signal conditioning electronics and microprocessor) were not needed at the point of action and could be located in the larger base. To be easily transportable the actuator must run off of a battery. Since the electronic transformer size is a function of the voltage, minimization of voltage is desired with a maximum voltage constraint of ± 300 V. When the actuator is off, it must rest at the neutral horizontal position so the gun will function as a normal gun in case of failure. This was a critical and defining requirement because it precludes the use of a DC offset and eliminates many of the existing high stroke piezoceramic actuators that depend on unidirectional materials at high electric fields. The energy requirements dictate that the system needs to be off except when firing and the system would be activated just prior to the trigger pull.

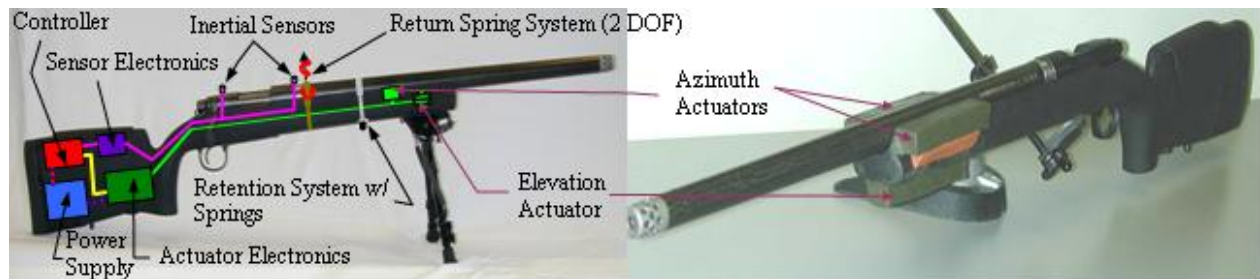


Figure 1: INSTAR Design.

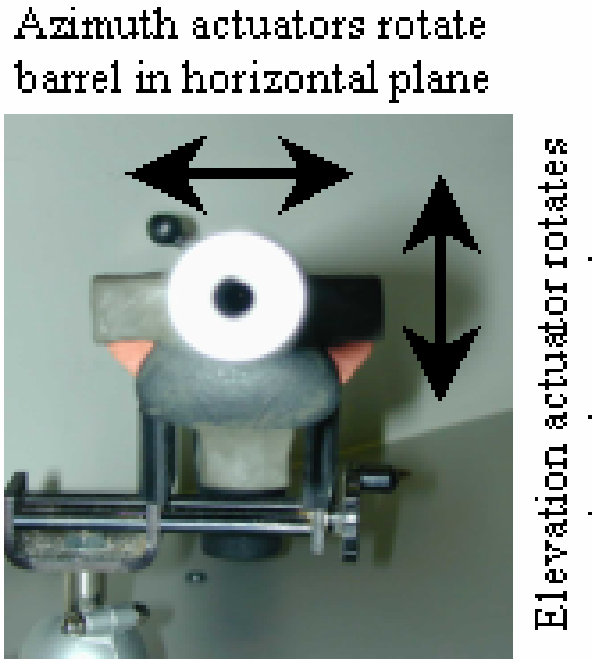


Figure 2: INSTAR Barrel Movement.

1.2.2. INSTAR Actuation Specifications

According to specifications set by the Advanced Drives and Weapon Stabilization Lab (ADAWS) at Picatinny Arsenal, INSTAR was designed to isolate a shooter-induced disturbance from the gun barrel point-of-aim for a stationary shooter with disturbance amplitude of 1.5 to 3 silhouettes at the range of 400 m assuming no wind conditions, Figure 3. While the final INSTAR system is intended to move in both the azimuth and elevation directions, the proof-of-concept prototype was simplified to demonstrate the most difficult direction - the elevation controlled by only one actuator to lift and springs to return the barrel.

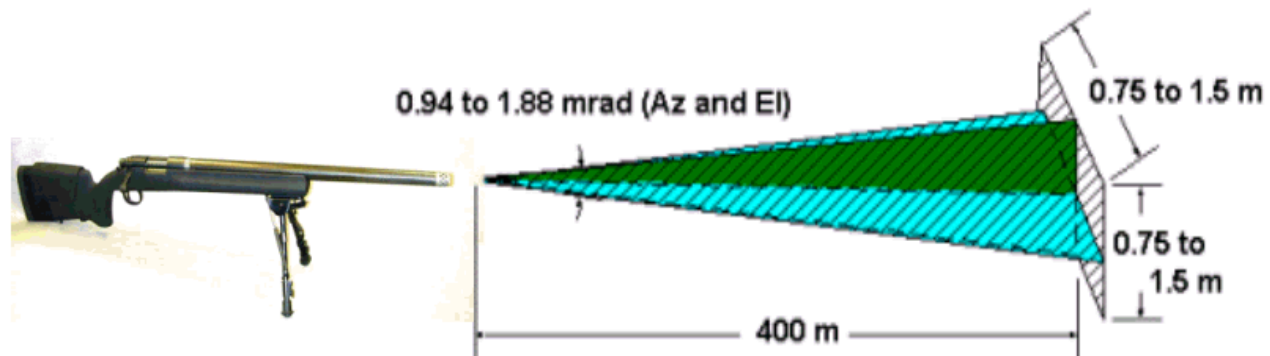


Figure 3: INSTAR Requirements.

Table 1.1: INSTAR Actuator Requirements.

| Silhouettes | Operational displacement | Operational force (up position) | Operational force (down position) |
|-------------|--------------------------|---------------------------------|-----------------------------------|
| 1.5 | ± 200 microns | 22.25 N | 3 N |
| 3 | ± 400 microns | 44.5 N | 6 N |

For this direction, to determine the actuator requirements, the suspension was modeled as a simple spring system shown in Figure 4. Since the frequencies are relatively low (below 10 Hz), the system was assumed to be quasi-static. Summing moments about the pivot yields

$$(\Delta X_s + l_s \theta)K_s l_s + Wl_w = ((\Delta X_a - l_a \theta)K_a + F_a)l_a \quad (1.1)$$

where ΔX_s is the compression of the springs, K_s is the stiffness of the springs, l_s is the distance from the pivot to the springs, W is the weight of the barrel, l_w is the distance from the pivot to the center of mass of the barrel. The actuator was modeled as a spring with stiffness, K_a , and an imposed force, F_a produced by the piezoelectric effect. The actuator located at a distance, l_a , deforms within the active suspension spring system a displacement of ΔX_a . Since the springs are nonlinear with a unique profile this was solved numerically and then approximated by the linear load-deflection diagram for the actuator, shown in Figure 5, assuming the actuator acts as a spring with constant K_a . These specifications correlate into actuator requirements given in Table 1.1, assuming a horizontal neutral position. According to Giurgiutiu, et. al., 1997, the most effective actuator in energy transfer is one that will match the system stiffness, in this case 48 N/mm.

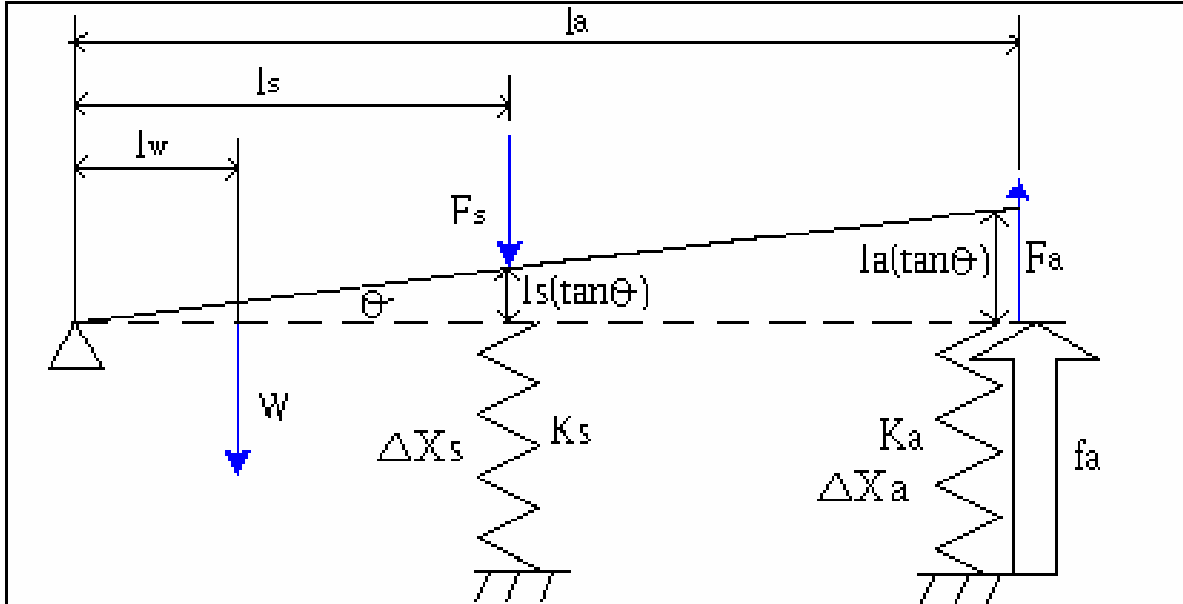


Figure 4: INSTAR System Model.

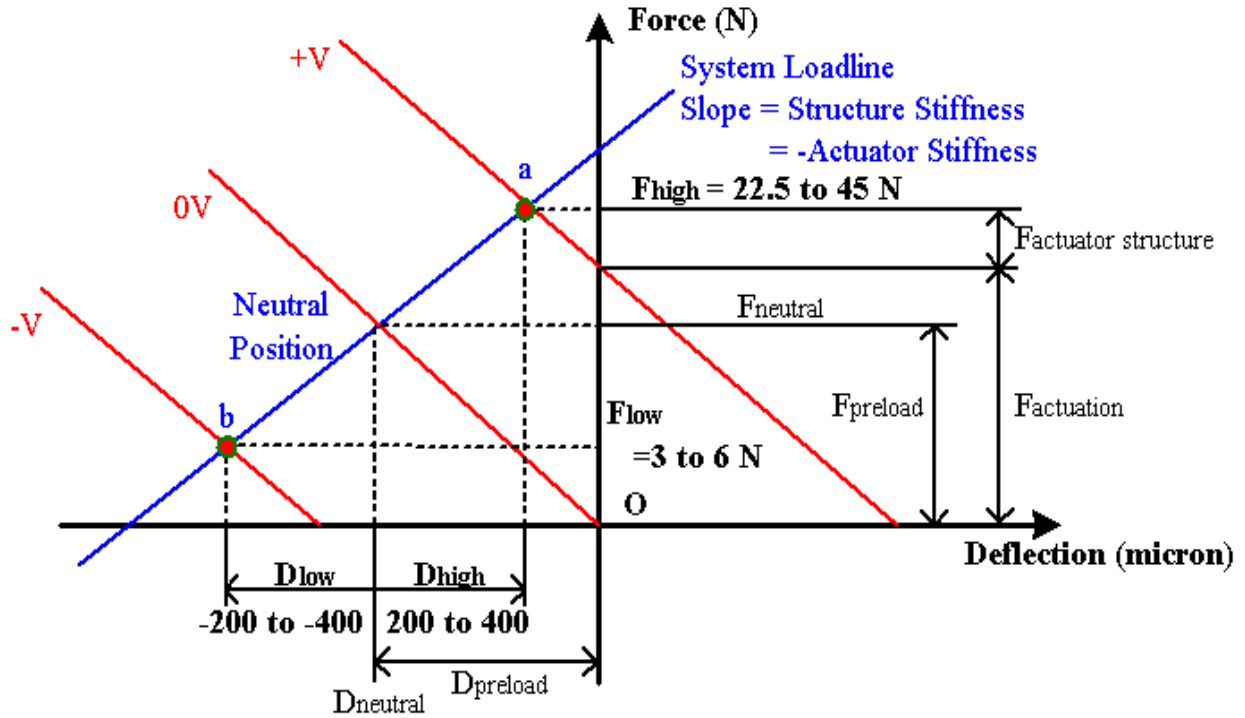


Figure 5: Required INSTAR Actuator Force-Deflection Performance.

1.2.3. Actuation Downselection Overview

The INSTAR application has severe volume and weight constraints while demanding high performance, which immediately eliminates conventional technology. For example, while electromagnetic actuators such as solenoids may meet the package and performance criteria, they are infeasible because they draw constant current that will drain the battery in approximately 15 minutes. Fortunately, the specific work and energy density metrics of most smart materials can fulfill the requirements if the actuation architecture can efficiently transform the material output into the proper force-displacement form required. Because the frequency and the high precision required was outside the typical range of shape memory alloys, piezoelectrics were chosen but will operate close to a static or DC state. In the selection of an actuation architecture, the stroke requirements immediately eliminated stacks and the force requirement eliminated benders. The package volume that this actuator must fit into is very awkward and makes it difficult to use most externally leveraging scheme since the translational motion is along the shortest direction. Since the gun must move both up and down and be in the center position when off, the current amplification systems that exploit very high energy density materials (such as EC98 by EDO Inc.) can't be utilized due to the single directionality and required DC offset of these materials. Two different approaches were explored to meet this need: 1) a d31 approach based on the Recurve architecture with focus on generating higher forces than is common for d31 actuators and 2) a d33 approach based upon a compliant mechanism designed using topology optimization with focus on providing more amplified strain than is common for d33 actuators. It should be

emphasized that while the work/energy metrics based on volume and weight constraints were kept in mind, the primary goal to both approaches was to effectively transfer energy by matching the stiffness of the INSTAR system while delivering both the force/displacement requirements in Table 1.1.

1.3. INTERNALLY LEVERAGED D31 MODE ACTUATION

For the internally leveraged architecture, a Recurve was selected because the architecture is flexible in meeting awkward packages and challenging performance requirements due to its tailorability afforded by the building-block elements. The basic Recurve building-block element is a straight bender comprised of multiple piezoceramic layers. Because of a unique electroding/poling scheme, two different moments are established across the span of the bending beam, Figure 6a. When energized, these moments generate relative linear motion at the tip but cancel all rotational motion. Some energy is stored within the actuator substructure during bending but this energy is recoverable on the back stroke to the power source through two-way high efficiency electronics enabling an extended battery life (Brei et. al., 2003).

Since individual Recurve elements produce linear tip displacement without rotation, they can be efficiently interconnected in series and/or parallel, Figure 6c, to increase deflection and/or

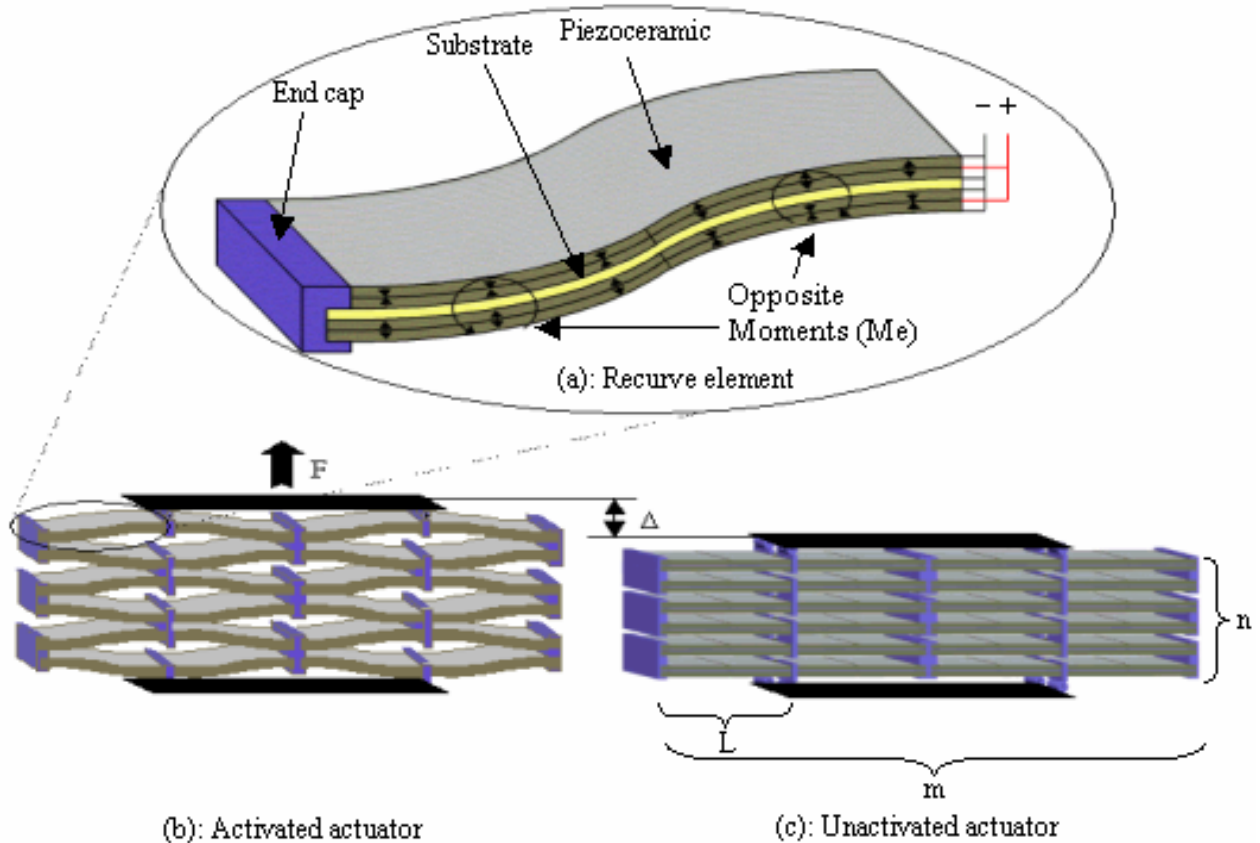


Figure 6: Recurve Actuation Architecture and Operation.

force output. This leads to a highest work per volume actuator (Ervin, 1999) in the high displacement regime. When this distributed array is energized it produces a net “push” and/or “pull” motion, Figure 6b, without transmission losses commonly experienced by externally leveraged architectures. As elements are combined, the force and deflection can be increased in a predefined manner enabling the stiffness of the actuator to be matched to the suspension system for optimal energy transfer. In addition the building block concept allows for several different configurations to meet the same force-deflection requirements, enabling the package shape to be tailored to the INSTAR volume constraint. This design flexibility is extremely important for any application requiring compact actuation simultaneously with high performance.

1.3.1. INSTAR Recurve Design Synthesis

Since the actuator is intended to operate below the first natural frequency, the design parameters were chosen based upon the quasi-static model presented in Ervin and Brei, 1998,

$$\frac{\Delta}{n} = \frac{-F}{m} \frac{L^3}{12D} + \frac{M_e L^2}{4D} \quad (1.2)$$

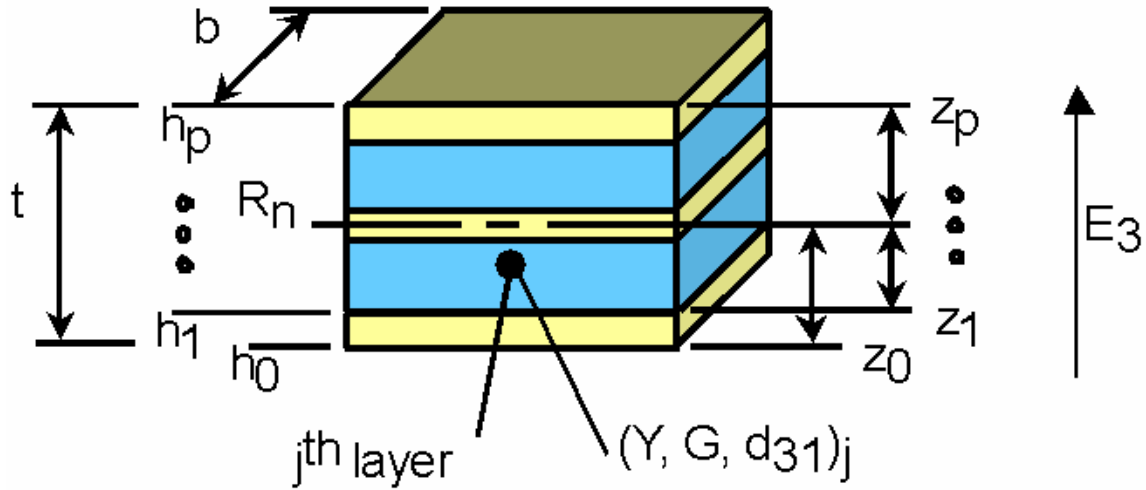
where F is the applied force, Δ is the deflection, m and n are the number of Recurve elements in parallel and series, respectively, L is the length of each Recurve element, M_e is the internal moment,

$$M_e = \sum_{p \text{ layers}} (Yd_{31}E_3)_j \frac{(z_j^2 - z_{j-1}^2)}{2} \quad (1.3)$$

and D is the composite beam stiffness is,

$$D = \sum_{p \text{ layers}} (Yb)_j \left(\frac{z_j^3 - z_{j-1}^3}{3} \right) \quad (1.4)$$

where each layer of general thickness has width, b, Young’s modulus, Y, and strain coefficient, d_{31} , under an electric field, E_3 (Figure. 7). Given the INSTAR requirements, a C++ program was developed which searched the entire design space (all relevant physical dimensions as well as both brass and steel substrates) and outputted all feasible designs. For the package volume dictated by INSTAR there were hundreds of feasible configurations but taking into account the desire to reduce the overall number of elements without risking buckling failure, a four (4) parallel and fourteen (14) series configuration was chosen. Each individual Recurve element has a length of 29.75 mm, a width of 21 mm, a substrate thickness of 508 μm , and 537 μm thick layers of PZT-5H on either side of the substrate.



1.3.2. Loss Mechanism Study

While the model captures the behavior of an ideal Recurve actuator, there are several pragmatic decisions that had to be made with regards to how the endcaps connected the Recurve elements and how the multiple piezoceramic layers were bonded. To assist in the selection of these practical issues, experimental studies were conducted into the loss mechanisms. First, three different endcap configurations were studied for the connection of serial Recurve elements, Figure 8. The “fully clamped” style binds the entire structure. While this method provides the

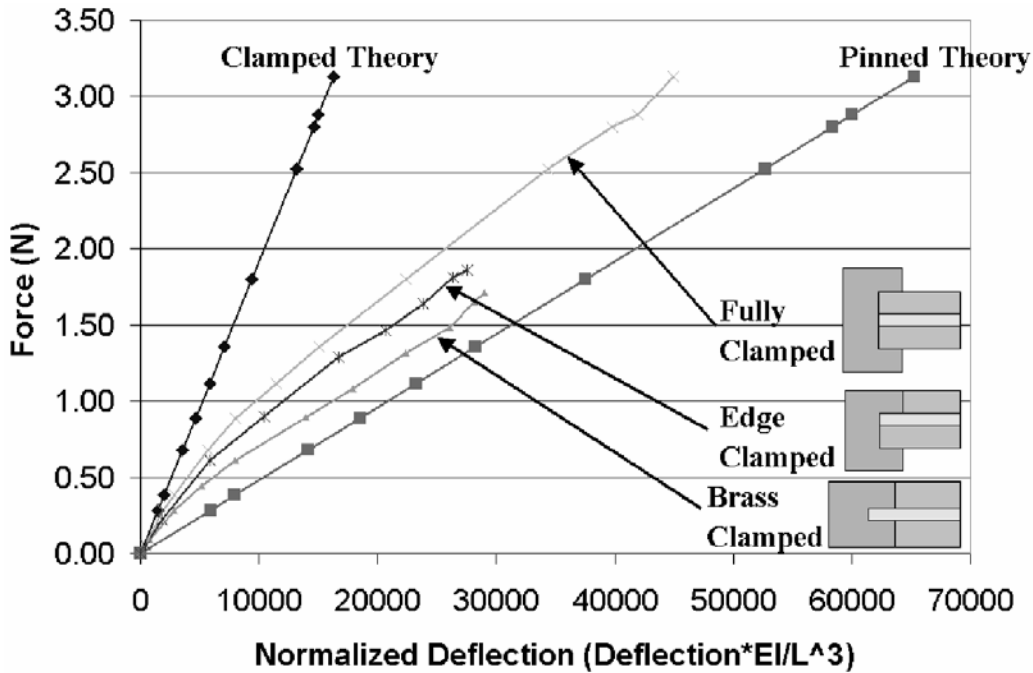


Figure 8: End Cap Effect on Stiffness Experimental Study.

closest approximation to the desired rigid end condition, the stack height of the 2x4 Recurve is increased because the end cap must be taller than the actual Recurve to clamp every layer. Because of the strict volume constraint, this extra space could not be tolerated. A second style is the “brass clamped” in which none of the piezoceramic material is within the end clamp. While this does reduce the risk of the piezoceramic cracking at the endcap, the boundary condition is closer to a pinned condition than the desired fixed end resulting in a decrease of 16.3% in the stiffness when compared to the fully clamped case. The “edge clamped” style provided a compromise. It eliminated the stack height problem associated with the fully clamped style by having the endcap flush with the outer piezoceramic layer, but provides a more rigid connection (up to 10% more) than the brass clamped because the inner piezoceramic layer is within the endcap.

To reduce the required voltage level to within the specified regime and utilize off the shelf material, two layers of standard 264 micrometer thick PZT5H were selected instead of design specified 537 micrometer single layer thickness. Additionally, the piezoelectric material was not available in lengths greater than 72 mm, which was not long enough to span the entire length of each 1x4 Recurve. Therefore, each 1x4 Recurve was built with segmented piezoceramic plates. To test the effect different segmented layups on the stiffness of the actuator, cantilever beams were constructed and their stiffness was measured. Figure 9 contains a plot of force versus deflection for various multilayered, segmented samples. While multiple layers reduce the required voltage, a significant impact on the stiffness was observed with multi-layered samples experiencing a 20.6% reduction when compared to single-layered samples. Segmentation also has a detrimental effect with single-layered samples experiencing a 12.7% reduction in stiffness due to segmentation and multi-layered samples experiencing a 9.5%

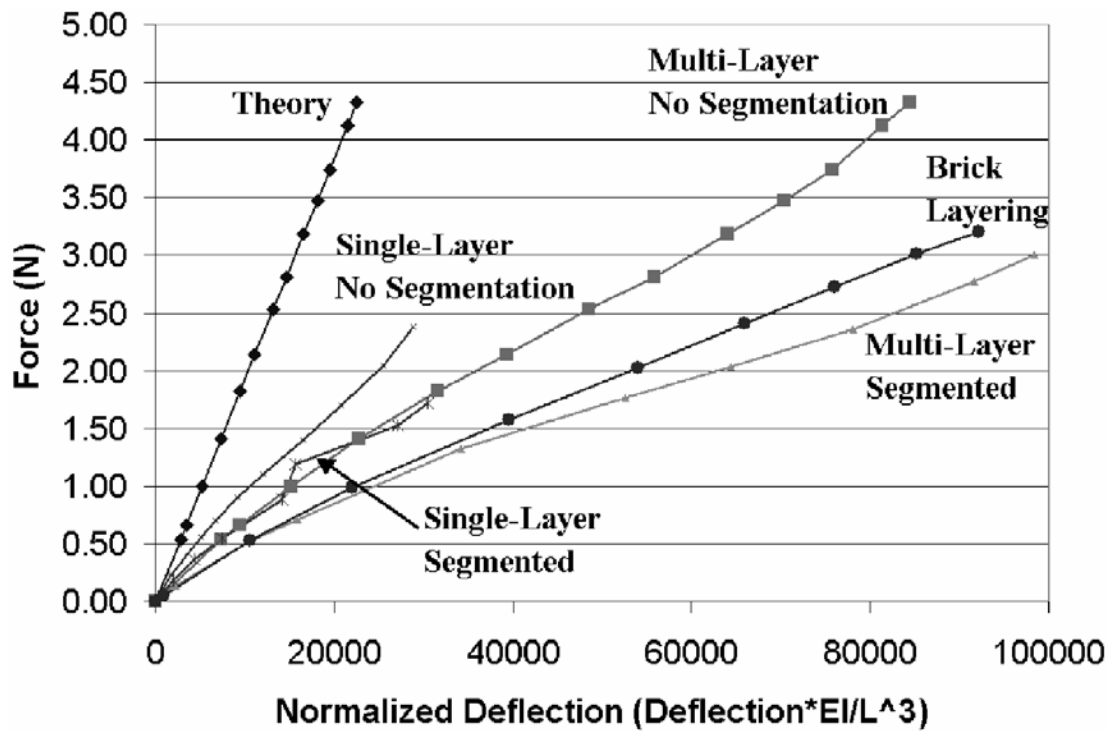


Figure 9: Segmentation/Layering Effect on Stiffness Experimental Study.

reduction in stiffness due to segmentation. A multi-layered sample was built with the piezoceramic segments staggered to produce a “brick-layering” effect. This sample only produced a 1.7% increase in the stiffness, which wasn’t significant especially with regards to the increase in complexity of the actuator. Thus, when possible single layers should be utilized, but in the absence of this option for the INSTAR demonstration, a simple segmented multilayer was chosen with edge clamped endcaps in an effort to mitigate these losses.

1.3.3. Recurve Prototype

A full scale Recurve prototype was fabricated for benchtop experimental characterization and incorporation within the INSTAR demonstration platform (Figure 10). PZT5H plates were laser machined to the proper size for segmentation and alternate sections repoled for opposite polarity to achieve the unique Recurve bending motion. Because of the available off-the-shelf thicknesses, two plates were combined to form one Recurve layer. Flex circuits, $\frac{1}{2}$ oz. copper on 50 micrometer kapton polyimid film, were etched for the electrode pattern and tabs on the edge of the circuit provided an external contact point used to connect all of the layers in the final assembly. An individual Recurve element was built up from the piezoelectric layer (2 plates bonded together) with the flex circuit electrodes bonded on either side of the brass shim with 2-part adhesive (Devcon E120HP). This Recurve unit (four in parallel, 1 in series) was placed in a 70 lb pretension jig during the curing of the epoxy to achieve a precompression in each unit for reliability. To combine the elements in series, pairs of these units were joined with steel edge-clamped end caps and spacers with cynaoacrylate adhesive (Duro QuickGEI). A wire bus was soldered to the flex circuit tab on each layer providing a hot and ground wire to the INSTAR system for activation. The resulting prototype, shown in Figure 10, was 136 mm x 22 mm x 28 mm and weighed 530 grams.



Figure 10: Recurve Prototype for INSTAR.

1.3.4. Dynamic Benchtop Characterization

While the actuator was designed to operate in the quasi-static mode, to confirm the bandwidth the actuator was experimentally characterized on the benchtop. A 10 V sine wave input signal from a dynamic signal analyzer (HP model 35670A) was sent to the clamped prototype. The frequency was swept from 10 Hz to 300 Hz, during which, the peak amplitude and phase of the free end of the actuator was measured using a Philtac model A88NE1 fiber optic probe fed back to the dynamic signal analyzer. The results are shown in Figure 11. The first resonance of the actuator is 170 Hz, and the quasi-static response is flat until 60 Hz, at which point the tip deflection increases until reaching a peak of 2.5 times the static deflection at resonance. Since the actuator is required to perform across several frequencies, resonance was not used as an amplification scheme. These tests confirm that the Recurve has more than the necessary bandwidth for up to the 10 Hz required operation and may be useful for other applications in the future such as vibration control within the barrel.

1.3.5. Quasi-static Benchtop Characterization

The real test of the actuator was if it could meet the INSTAR quasi-static requirements laid out in Figure 5 and Table 1.1. To confirm this, quasi-static force-deflection experiments were performed. The prototype was mounted in a fixture and the displacement was monitored

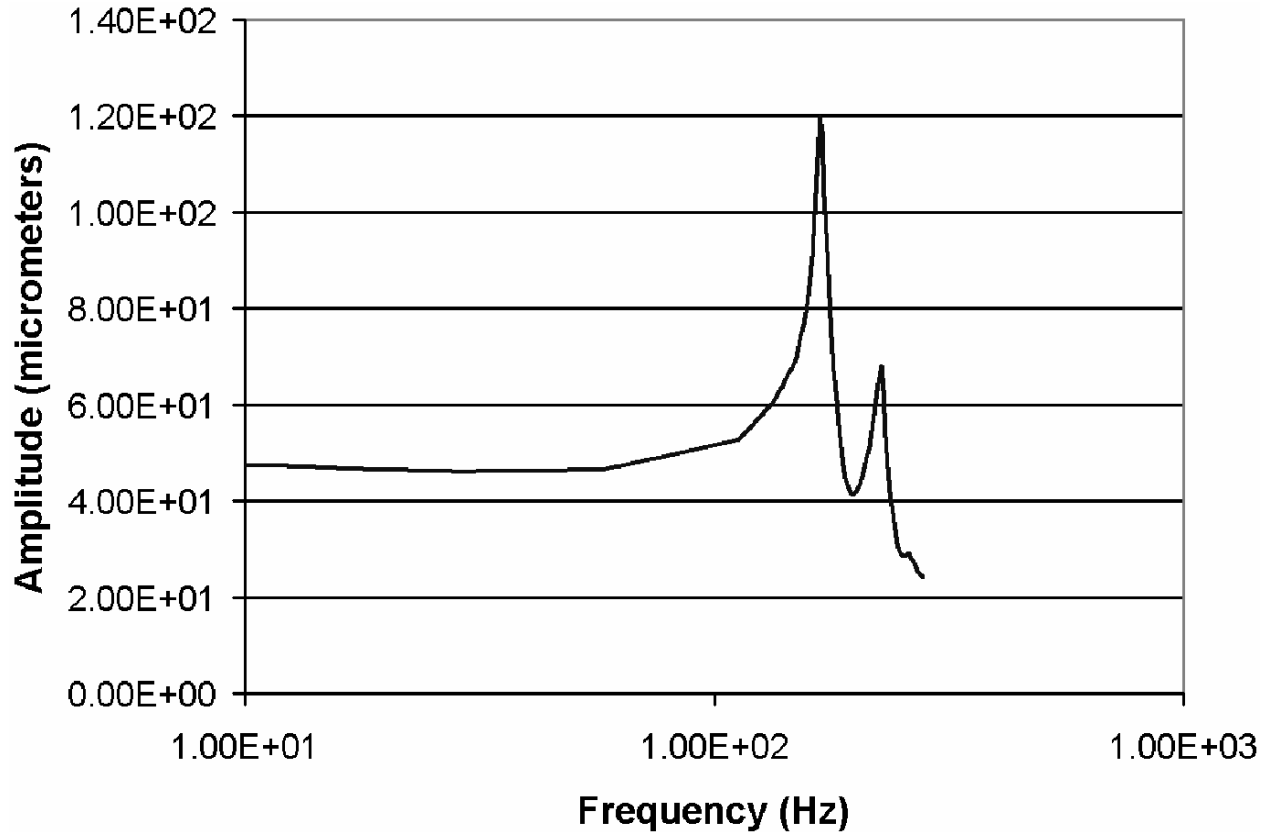


Figure 11: Dynamic Test Results for Recurve Actuator.

with a Philtex model A88NE1 fiber optic probe. Voltage was applied across each piezoceramic layer and the blocked force of the actuator was measured with a Cooper Industries LPM 530 force transducer. The force transducer was backed off incrementally until the free deflection was achieved. The direction was then reversed and the transducers were used to measure force and deflection into the negative deflection region. This procedure was repeated for several voltage levels ranging from ± 209 V (400 V/mm).

The results for the maximum positive (209 V) and negative motion (-209 V) range along with the actuator stiffness test (0V) are shown in Figure 12. While the stiffness of the actuator varied considerably through its cycle, it met or exceeds the INSTAR specifications of 48.125 N/mm. The overall structural stiffness of the actuator was 61.44 N/mm. The actuator decreased in stiffness with upward motion (43.3 N/mm), falling within 10% of the design stiffness. As expected from the endcap experiments, because the piezoceramic is not clamped in this direction, for large strokes the endcap resembles more a pinned end instead of a rigid clamp; thus, leading to a more compliant actuator. The actuator stiffness increased significantly with downward motion (327.5 N/mm). It was observed that the bonding layers between serial Recurve elements was thicker than specified in the design causing the Recurve elements to bottom out during the actuator compression leading to the sharp increase in stiffness, something that can be corrected in future generations of the actuator. Despite the changes in stiffness, the actuator was able to overcome the traditional force problems with d31 actuators and exceed the INSTAR specifications with 12.6 N of force at the downward swing of -331 micrometers from

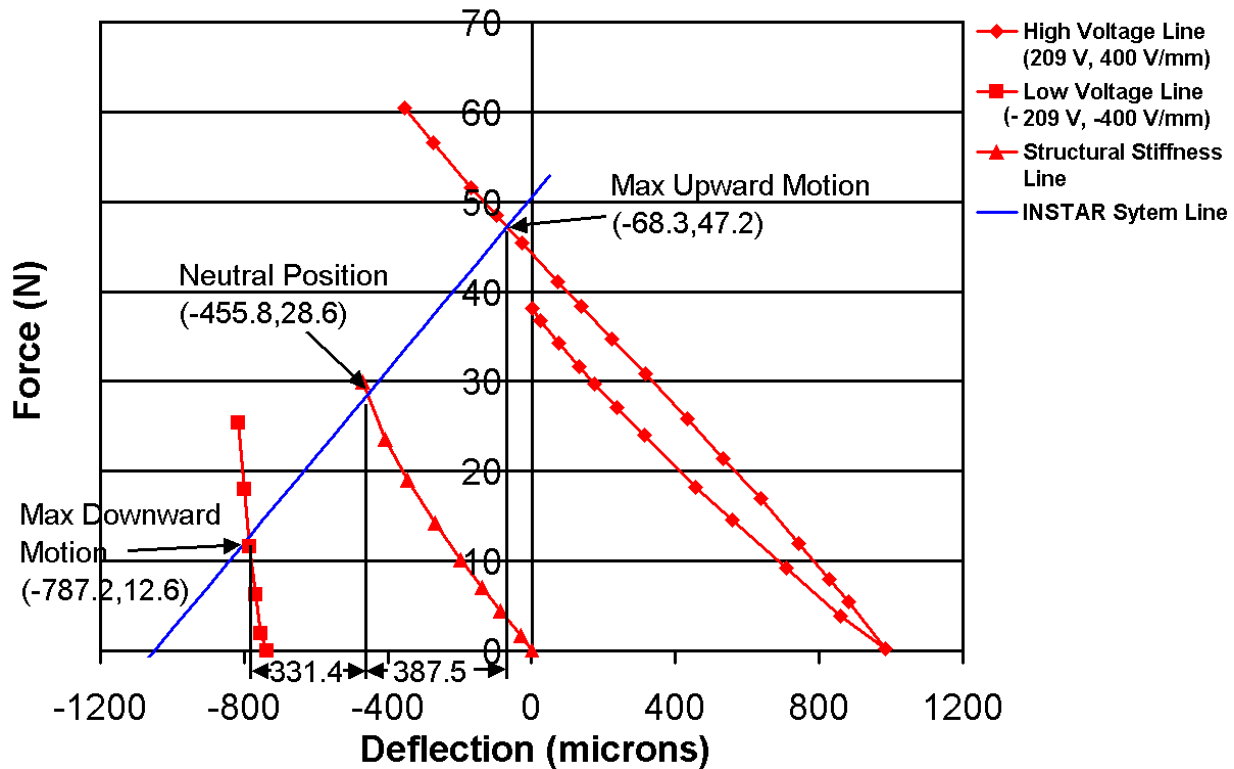


Figure 12: Quasi-Static Experimental Results for Recurve Actuator.

the neutral position (-456 micrometers, 28.6 N), and 47.2 N at the upward swing of 388 micrometers. Overall this actuator has a very large bi-directional stroke for a piezoceramic reaching +966 micrometers to -745 micrometers of free deflection providing a total tip-to-tip stroke of 1.711 mm (as much as 10 times more than comparable current state of art piezoceramic actuators).

1.4. EXTERNALLY LEVERAGED D33 MODE ACTUATION

It is clear that the displacement was available for the d31 actuator and the driver was obtaining enough force and stiffness from the actuator. A different approach to the INSTAR problem is to use a d33 mode actuator; in this case the design driver was obtaining enough displacement and making the actuator compliant. Key to leveraging in a d33 mode actuator is minimizing the losses within the external lever. Compliant mechanisms are similar to mechanical linkages without hinge joints, and eliminate many of these losses because there are no joint clearances or frictional losses. In order to design an actuator based upon compliant mechanisms, a modified version of previous topology optimization methodologies was developed (Frecker and Canfield, 2000a,b; Canfield and Frecker, 2000). The methodology developed and resulting INSTAR design and prototype results are discussed in this section.

1.4.1. Design Synthesis

The compliant mechanism topology design problem for the INSTAR application is shown in Figure 13. The design domain, or allowable space for the compliant mechanism to reside in, is represented by the 22 by 138 mm rectangle. Due to the long, narrow available volume for the INSTAR application, the piezoelectric stack actuator is placed in the horizontal direction in the center of the design domain. The equivalent force on the compliant mechanism due to the expansion of the piezoelectric actuator, f_a , depends on the applied voltage, cross-sectional area, length, and layer thickness of the stack actuator, and the material properties. The preloaded spring at the output point B is modeled as a spring of stiffness $k_{ext} = 48750$ N/m with constant downward preload force of 25.25 N.

In general, the compliant mechanism is designed to amplify the input displacement from the piezoelectric actuator as much as possible while transferring it from the input point A to the

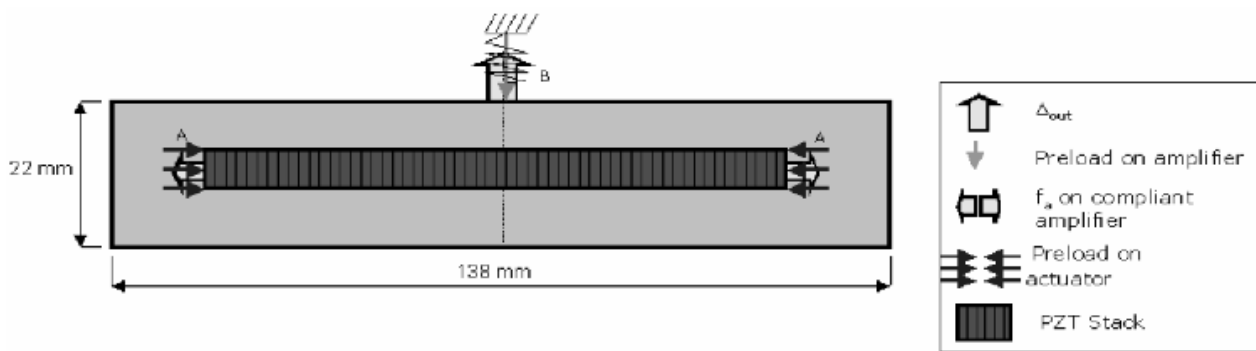


Figure 13: INSTAR Design Problem.

output point B. The output displacement (Δ_{out}) is formulated by applying a unit dummy load (f_b) at output point in the direction of Δ_{out} , and forming the mutual potential energy (MPE).

The design domain is discretized into finite elements; a ground structure of frame elements (3 dof per node) is used to model the continuous design domain, the piezoelectric actuator is modeled as a single active rod element, and the external spring stiffness is modeled as a passive rod element. The design variables are cross-section areas of the passive frame elements. Topology optimization is accomplished by allowing the cross-sectional areas of each element to vary within pre-specified lower and upper bounds with the aim of maximizing the GA. The problem formulation is given in Equation 1.5.

$$\begin{aligned} \max GA &= \frac{\Delta_{out}}{\Delta_{in}} \\ S.T : A^T L - V_0 &\leq 0 \end{aligned} \quad (1.5)$$

The lower bound on the design variables is set to a very small value and thus the elements that reach the lower bound can be ignored from the final topology. The initial discretized domain is shown in Figure 14.

Studies were conducted to determine the best location, dimensions, and number of actuator elements. The best topology in terms of output deflection is shown in Figure 15 (a). The predicted output displacement of this topology is $D_{out} = +139.7$ mm at +300V, where D_{out} represents the output displacement at the operating point.

From the results of topology optimization, a solid model interpretation was created using Pro/Engineer (Figure 15 (b)). The structural combinations of elements in the optimal topology are interpreted as solid material and the smaller groups of elements as thin sections. Figure 15 shows that the basic topology has been preserved. Detailed finite element analysis was carried out on the solid model using Pro/Mechanica. The active material (shown in red) used is Pz26 by Noliac A/s, while the passive material is Aluminum 7075. Custom Pz26 stack actuators by Noliac A/S were chosen for the INSTAR application because they can be operated by positive as well as negative voltage, and have a very small layer thickness. In the finite element model, piezoelectricity is modeled using an equivalent thermal expansion with the coefficient of thermal

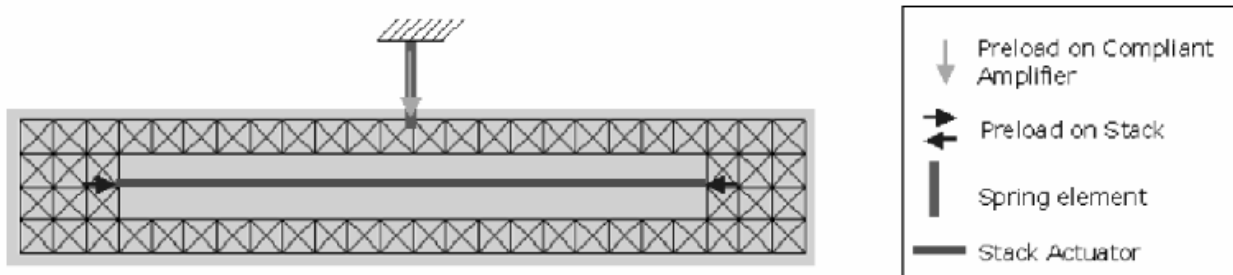


Figure 14: Discretized Design Domain.

Table 1.2: Passive Material Variation Study.

| Material | Young's Modulus (GPa) | A_{out} (μm) | Yield Strength (MPa) | Maximum Von-Mises Stress (MPa) |
|-----------------|-----------------------|----------------|----------------------|--------------------------------|
| Delrin P100P | 2.9 | -470 | 70 | 370 |
| Stainless Steel | 193 | 591 | 331 | 466 |
| Low Alloy Steel | 200 | 590 | 315 | 480 |
| Brass | 110 | 621 | 75 | 387 |
| Al 2011 – T3 | 70 | 628 | 295 | 381 |
| Al 7075 – T4 | 72 | 628 | 305 | 381 |

expansion calculated as,

$$\alpha = \frac{d_{33}n}{l} = \frac{(400E - 12)(1492)}{0.1} = 5.968E - 6 \text{ per}^{\circ}\text{C} \quad (1.6)$$

where d_{33} = the piezoelectric constant = 400 m/V, n = number of layers in the stack actuator = 1492, l = total length of the actuator = 0.1 m. The final finite element model consisted of 2940 tetrahedral solid elements. A spring of stiffness 48750 N/m was incorporated in the finite element model at the output point along with the constant downward preload of 25.25 N. The bottom surface of the compliant mechanism is constrained from moving.

Using this finite element model, the predicted output at the INSTAR operating point was $\Delta_{out} = +461.5 \mu\text{m}$ and $F_{out} = 48 \text{ N}$ at $+150 \text{ V}$. Hence the design theoretically meets INSTAR requirements; however, the piezoelectric actuator may experience bending, which could cause the stack actuator to delaminate. Therefore, the design was modified to the symmetric configuration shown in Figure 16, where actuator bending is prevented due to its symmetry. Note that the compliant mechanism was originally designed only for upward displacement at the output; it was assumed that downward displacement can be obtained by reversing the polarity of the voltage applied to the piezoelectric actuator. The predicted downward displacement is illustrated in Figure 16 (b). The predicted output for the symmetric design was $\Delta_{out} = +624.4 \mu\text{m}$ at $+150\text{V}$ (a) and $\Delta_{out} = -489.8 \mu\text{m}$ at -100V (b).

1.4.2. Material Study

A passive material variation study was performed on the symmetric design, as shown in Table 1.2. The finite element simulations were performed at 150V, using a compliant amplifier of dimensions 138 mm x 35 mm height x 22 mm width. Notice that the selection of the passive material, and hence the stiffness of the compliant mechanism has a significant effect on the

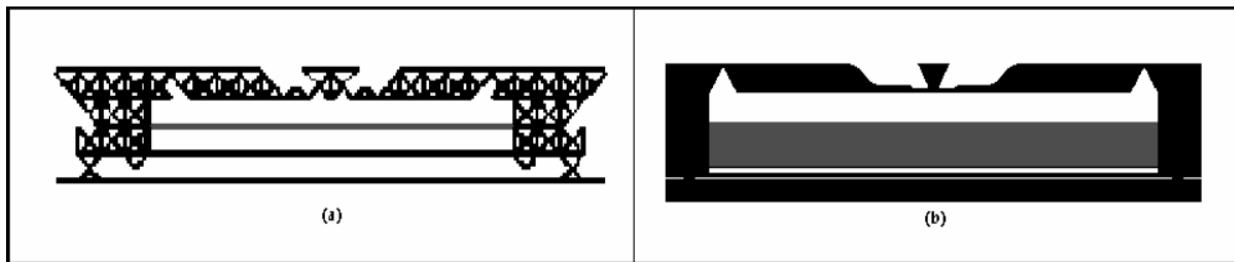
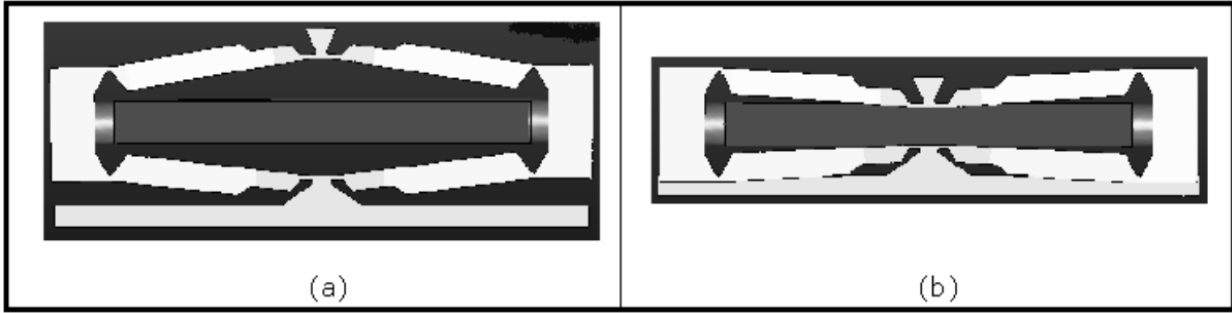


Figure 15: Optimal Topology Solution (a), and Interpretation (b).



output displacement. In some cases, e.g. Delrin, the material is so soft that the output point actually moves in the opposite direction. The best material in terms of stiffness and output displacement was determined to be aluminum (Al7075-T4), which also has a high yield stress.

1.4.3. Bonding Layer Study

As with the d31 actuator, there are losses that occur due to the pragmatic realization of the design. In this case, there will be losses due to bonding within the stack which was not accounted for in the initial compliant mechanism design. To account for these losses, the solid model was modified by adding a third material to model the bonding layers (shown in green in Figure 17). Each bonding layer of the actuator was estimated to be $20 \mu\text{m}$ thick, but the large number (1000) of thin bonding layers was modeled as 20 layers of 1 mm thickness in the finite element model. The bonding material was assumed to have Young's modulus of 2.0 GPa. The results are summarized in Table 1.3 for simulations conducted at $+150 \text{ V}$, where D_{out} and F_{out} represent the output displacement and force at the operating point, and D_{free} and F_{blocked} are the free displacement and blocked force, respectively. As expected, the absence of bonding layer

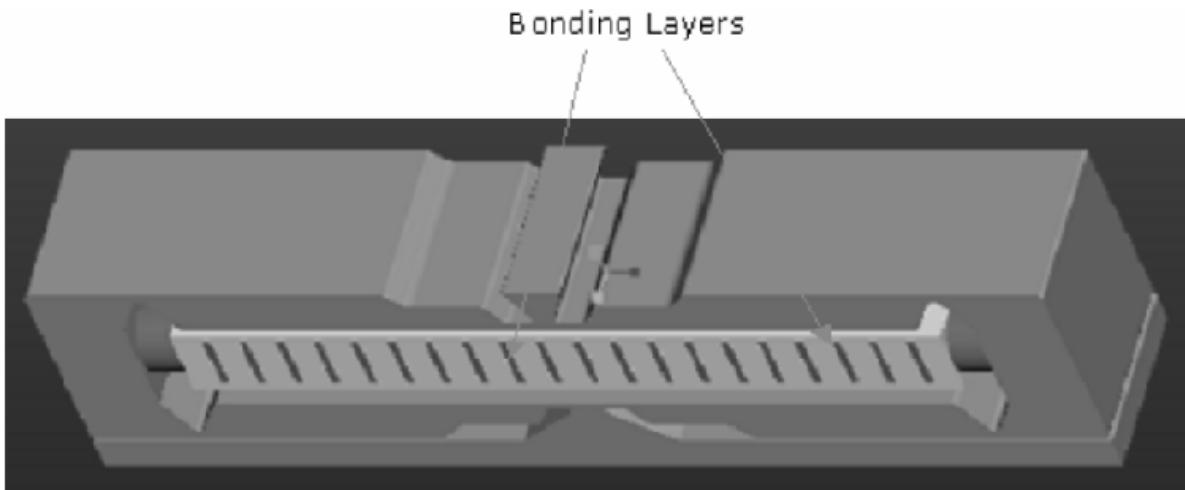


Figure 17: Solid Model with Bonding Layers.

Table 1.3: FEA Results with Bonding Layers.

| | Δ_{free} (μm) | F_{blocked} (N) | Δ_{out} (μm) | F_{out} (N) |
|-------------------------------------|-----------------------------|--------------------------|----------------------------|----------------------|
| Symmetric Model | 738.6 | 282.0 | 624.4 | 55.9 |
| Symmetric Model with Bonding Layers | 587.0 | 174.2 | 498.6 | 49.8 |

gave a finite element result that over-predicted the actual deflection by as much as 20%; the predicted deflection at +150V was +498.6 μm and the output force was 49.8 N.

It is interesting to note that a similar actuator design has been developed by Samuelson and Garcia, 1997. The actuator is called a Bi-directional Operating Actuator (BOA), and was designed based on a kinematic analysis. The two actuator designs were compared by resizing the symmetric compliant amplifier to 11mm x 28mm by 6 mm, which are the dimensions of the BOA amplifier, and the driving stack to the size of the BOA driving stack, 20mm x 5mm x 5mm. This comparison found that the scaled compliant amplifier exceeds the published results for the BOA actuator by 16.6%. For example, if a voltage of 130 V is applied to equivalent actuators, the output of the BOA would be 90 micrometers and the compliant actuator would be 105 micrometers.

1.4.4. d33 Prototype

A prototype actuator, Figure 18, was constructed for INSTAR. The compliant mechanism amplifier was fabricated from Al7075 T6 using wire EDM with a precision of 2 μm. A pair of stack actuators was placed front-to-back as shown in the figure. Each actuator was 100 mm long and had a cross-sectional area of 100 mm². Small steel end caps with screw threads were attached to both the ends of the stack actuators and then attached to the compliant mechanism amplifier using M3 screws to provide secure attachment and to prevent the actuators from slipping during actuation. The stack actuators were preloaded to 6.53 N by press fitting them

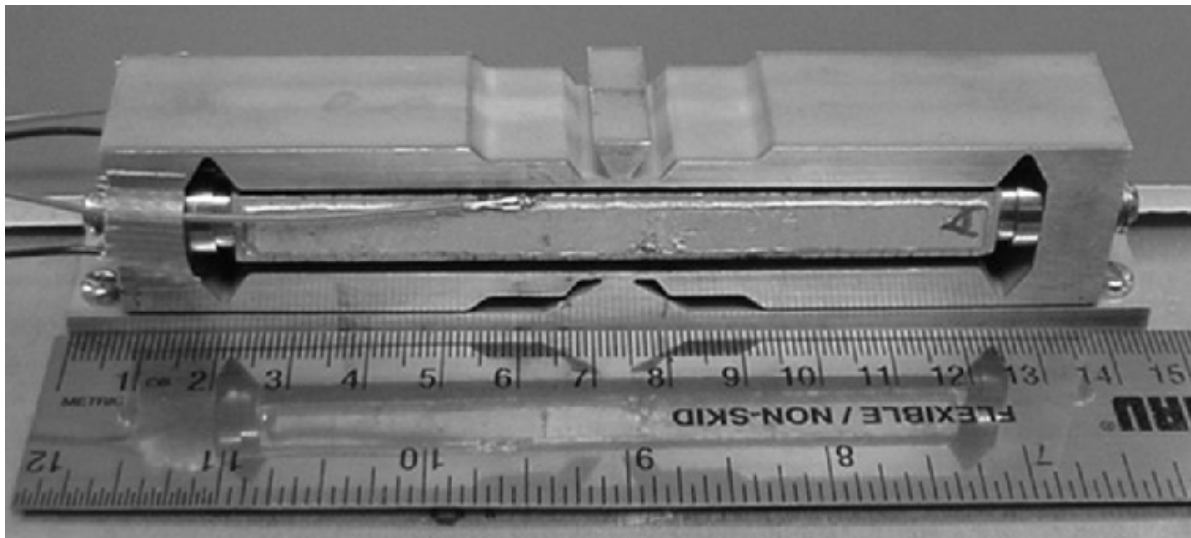


Figure 18: d33 Prototype Actuator.

into the compliant mechanism amplifier. Equal preload on each actuator was assured by measuring the voltage change due to the compressive preload and making fine adjustments with the attachment screws. The final prototype, shown in Figure 18 was 138 mm x 25 mm x 35 mm and weighed 339 grams.

1.4.5. Dynamic Benchtop Characterization

As with the Recurve, the prototype was dynamically characterized to confirm its bandwidth. A 5 V sine wave input signal from a dynamic signal analyzer (HP model 35670A) was sent to the clamped prototype. The frequency was swept from 50 Hz to 1000 Hz, during which, the peak amplitude and phase of the free end of the actuator was measured using a Philtac model A88NE1 fiber optic probe fed back to the dynamic signal analyzer. The results are shown in Figure 19. The actuator has a flat quasi-static behavior until 73 Hz, at which point the tip deflection increases until reaching a peak of 5.5 times at the first resonance of 98.5 Hz. It is interesting to note that this first resonance is less than the Recurve, resulting from compliance within the externally leveraging mechanism. As with the Recurve, this far exceeds the 10 Hz requirement for INSTAR and quasi-static performance can be assumed.

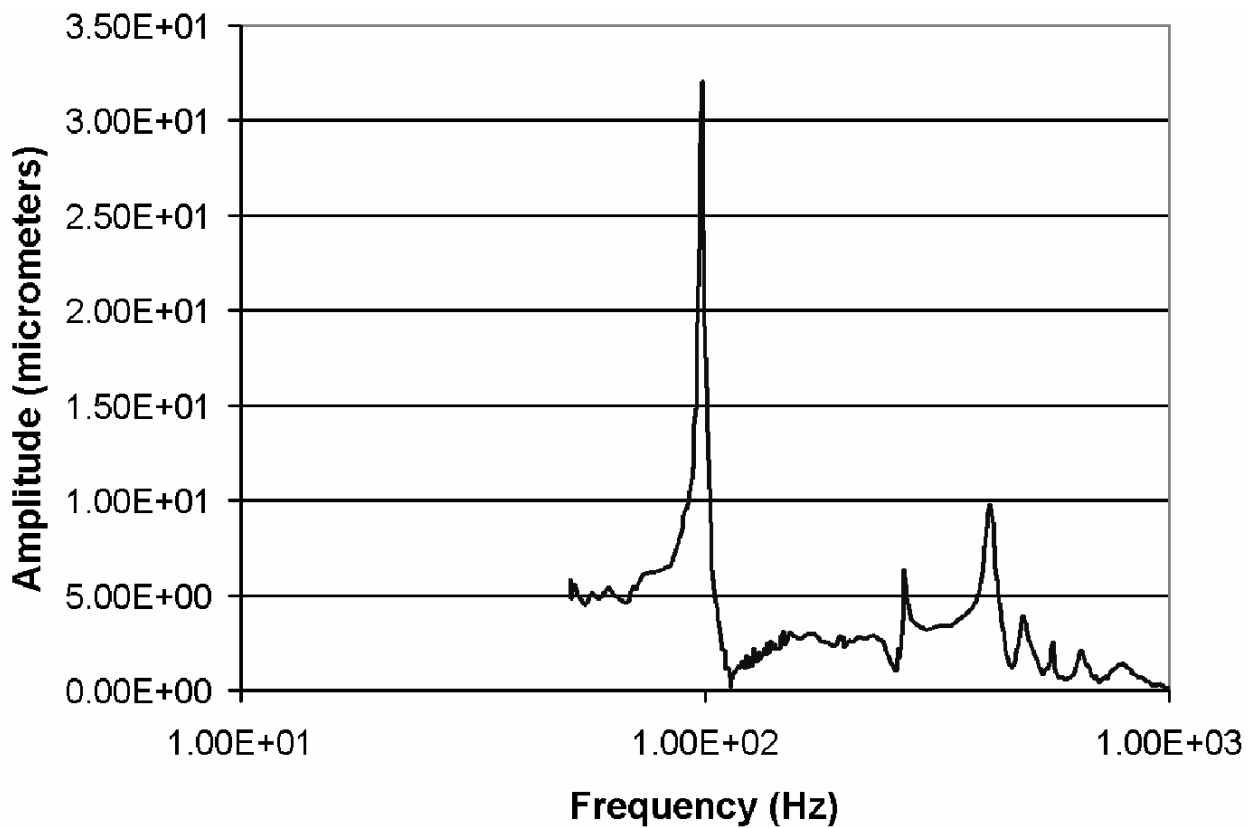


Figure 19: Dynamic Test Results for d33 Actuator.

1.4.6. Quasi-static Benchtop Characterization

The force-displacement performance of the actuator was characterized utilizing the same experimental setup and procedure as the Recurve actuator with the exception that the forces were applied using a preloaded spring. Figure 20 shows the results for the maximum upward (200V), maximum downward (100 V) and overall stiffness (0 V) tests. Note that although the same voltages were applied to the Recurve, in this case the electric fields are much higher (+2985 V/mm and -1493 V/mm) because of the thinner piezoceramic layers within the stack. The upward and downward voltages applied differed due to maximum specifications outlined by the manufacturer.

The compliant amplifier was able to meet the INSTAR requirements prescribed in Table 1.1, achieving 66 N of force with a 582 micrometer displacement from the neutral position on the INSTAR system line on the upward stroke, and 22.5 N with 324 micrometers displacement on the downward stroke. While displacements on the down stroke were similar between the Recurve and d33 mode actuator, the displacement of the d33 mode on the upward motion was considerably more, 582 micrometers compared to 324 micrometers. This led to a large tip-to-tip INSTAR stroke of 906 micrometers, very large for a d33 mode actuator. It was observed that the overall performance was nonlinear with the worst case at -100V. This non-linearity, and thus the small negative displacement, is attributed to insufficient preload on the stack actuator.

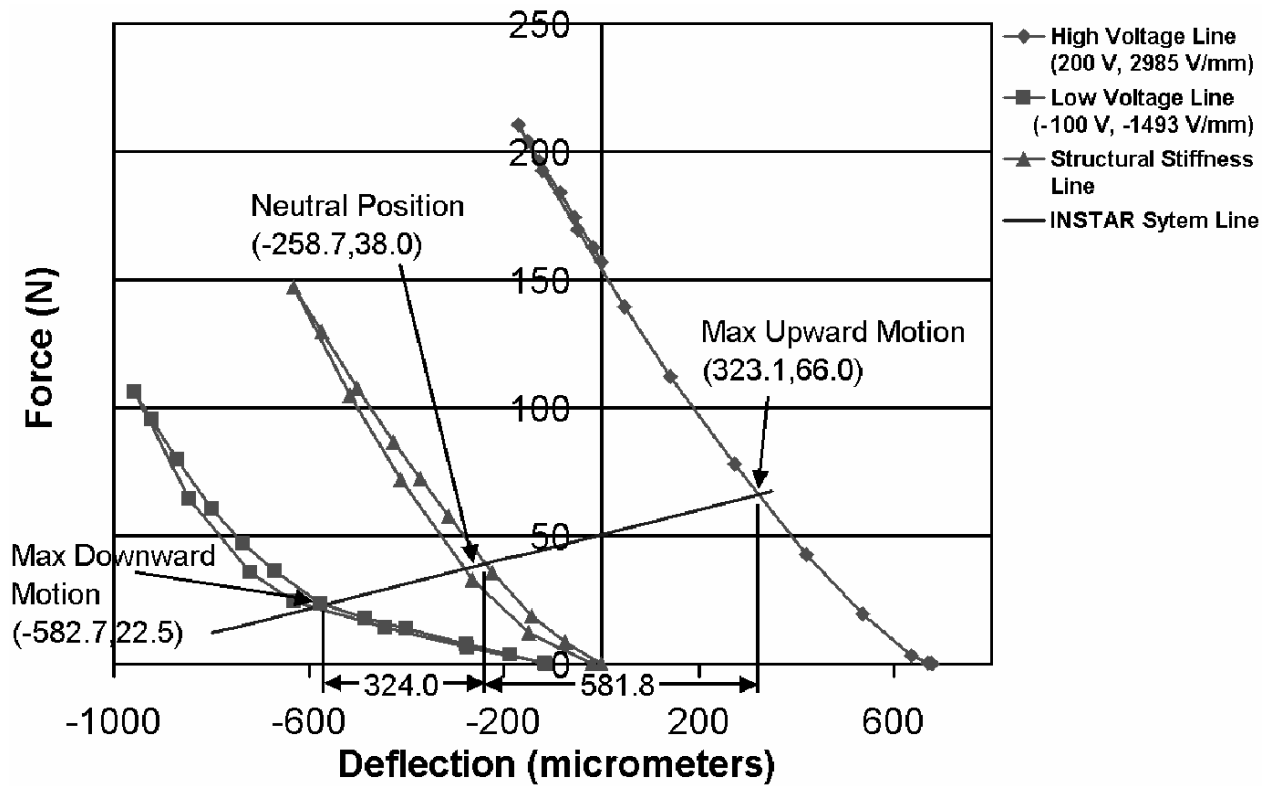


Figure 20: Quasi-Static Experimental Results for d33 Actuator.

1.4.7. Actuation Systems Discussion

It is interesting to note that the stiffness varied for the d33 mode actuator as it did with the d31 mode actuator, but opposite in this case, the actuator became stiffer as it traveled from the downward stroke (48.3 N/mm) to the upward stroke (237.5 N/mm). While the downward motion met the INSTAR stiffness requirement well, the structural stiffness and upward motion stiffness was considerably higher, a common side effect of d33 mode actuators. Another interesting difference is that the d33 mode actuator operates on the upward stroke in the first quadrant, leading to a higher blocked force (157 N) than operating force (66 N). On the other hand, the d31 mode actuator operated in the second quadrant giving a blocked force (41.8 N) lower than the operating force (47.2 N). As would be expected from this, the free displacement of the d31 mode actuator (966 micrometers) is significantly higher than the d33 mode actuator (679 micrometers). As expected, the weight of the d33 mode actuator was less because the density of the aluminum is much less than the piezoceramic. In contrast, the volume of the Recurve was less because of the higher specific work of the architecture. All of this stems from the primary design drivers. For the d33 mode, the primary design driver is obtaining stroke (goal of making the actuator more compliant); whereas for the d31 mode the primary design driver is obtaining force (goal of making the actuator stiffer). This highlights how the two approaches come from different ends of the design space to meet the INSTAR requirements.

1.5. ELECTRONIC SYSTEM

The second key element in INSTAR is the drive electronics for the Recurve actuators. These power electronics must satisfy several key criteria. They must fit entirely into the stock of the gun. In particular, the power source is constrained to be a low voltage battery. Second, they must manage the energy consumption such that the system has an acceptable lifetime. Third, they must deliver the electrical energy to the actuator in the proper form (e.g.. appropriate voltage level and bandwidth). The specifications for the amplifier are drawn from the specifications for INSTAR and the specifications imposed by the Recurve prototype - maximum voltage of 200 Vp-p and a 12 μ F load. The INSTAR control system requires the amplifier to have a bandwidth of 10 Hz to compensate for ergonomic disturbances.

1.5.1. Power Electronic Architecture

A simplified diagram of the power electronic system for INSTAR is shown in Figure 21. The flyback converter generates a high voltage output signal, required by the piezoelectric actuator, from the low voltage battery that supplies the power. This converter is connected to the half-bridge amplifier that delivers electrical energy to the actuator in response to a command or reference signal. Both of these electronic components are based on switching technology. This technology insures a high efficiency energy transfer between the battery and the piezoelectric actuator through high frequency pulse width modulation. In addition, the electronics contain a storage capacitor at the input of the half-bridge amplifier. The switching amplifier is so configured, that it allows for an energy exchange between the piezoelectric actuator and the storage capacitor. This configuration boosts the efficiency of the overall system, and allows for the extended life of the battery. More details for this design are given by Lindner, et. al, 2002.

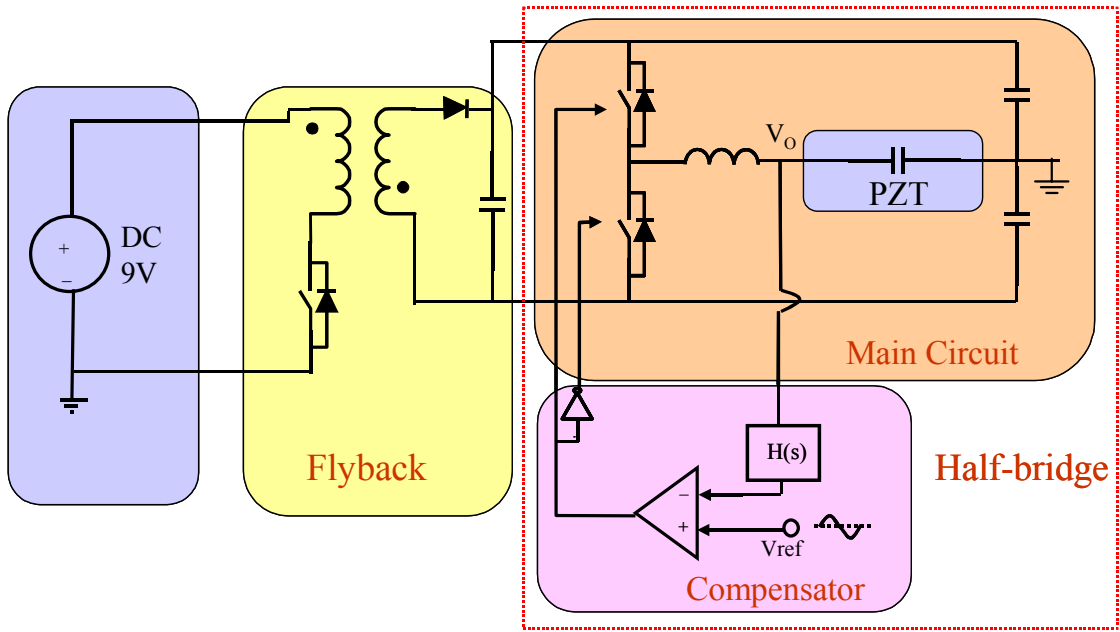


Figure 21: Block Diagram for Power Electronics.

1.5.2. Benchtop Characterization

A prototype of this amplifier was fabricated (Figure 22) and experimentally characterized on the benchtop. Given a sinusoidal reference voltage, the output voltage of this amplifier is 184 Vp-p sinusoid and the output waveform has low distortion and low noise as shown in Figure 23. The frequency response, shown in Figure 24, is flat well beyond the required bandwidth of 10 Hz. The measured power losses for a purely capacitive load are shown in Figure 25. These losses, which are rather low, may be expected to increase slightly with the Recurve actuator

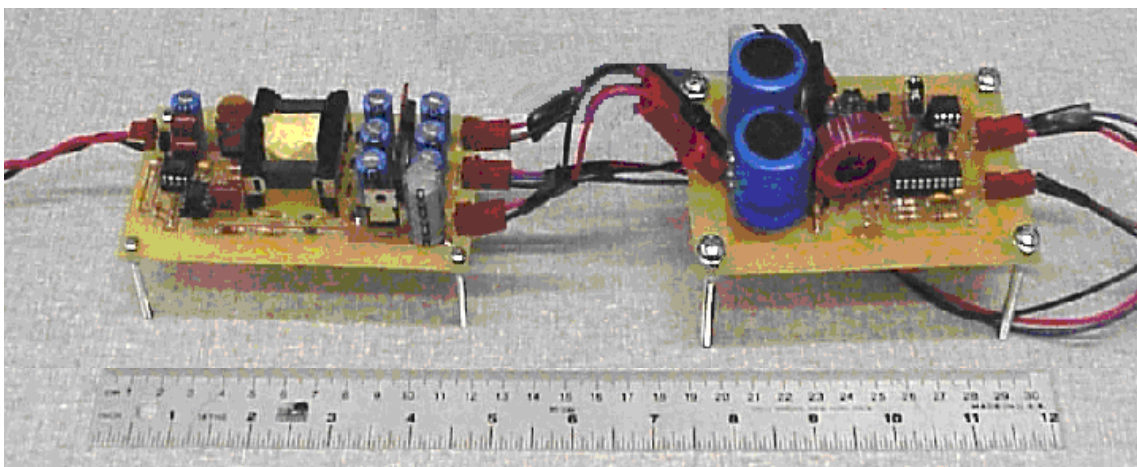


Figure 22: Prototype of the Power Electronics for INSTAR.

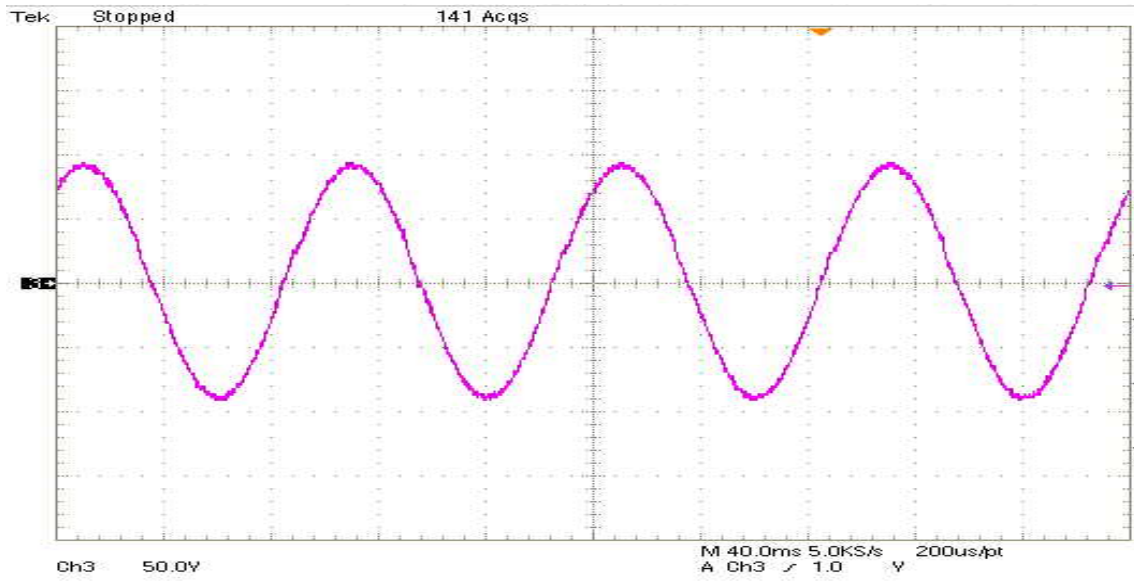


Figure 23: Switching Amplifier Output Voltage.

because of the mechanical losses in the actuator and the losses due to the net work done by the actuator.

1.5.3. Energy Study

The energy consumption of the electronics and its impact on the performance of the INSTAR system can be estimated by a simple loss calculation assuming that the voltage source is a standard 9V battery and the flyback converter has a fixed efficiency of 80%. The half bridge switching amplifier drives the Recurve actuator (modeled as a capacitor) with a sinusoidal signal. During the activation of the actuator, the electronics delivers energy to the actuator. As the actuator returns to the neutral position, this energy is regenerated back to the electronics and is stored in the two storage capacitors connected to the actuator. On the next actuator cycle, the energy in the storage capacitors is used to power the actuator rather than drawing energy from the battery. It is assumed that the efficiency of the half bridge amplifier, which manages this energy exchange, is 90 %. The model ignores mechanical work produced by the actuator since calculations have shown that the electrical power delivered to the actuator is two or more orders of magnitude greater than the mechanical work done. While INSTAR is activated, the “on-time,” the electronics will dissipate this given amount of energy. The number of shots per battery can be calculated as a function of the “on-time/shot” based on the total energy in the battery. By way of comparison, this same energy calculation was repeated for drive electronics that employed a linear amplifier rather than a switching amplifier. With a linear amplifier the regenerative energy is dissipated as heat in the amplifier rather than recycled. The results for both the linear and switching amplifier is given in Figure 26. Assuming the average on-time is 2 seconds, this calculation suggests that the INSTAR system can provide thousands of shots per battery, which

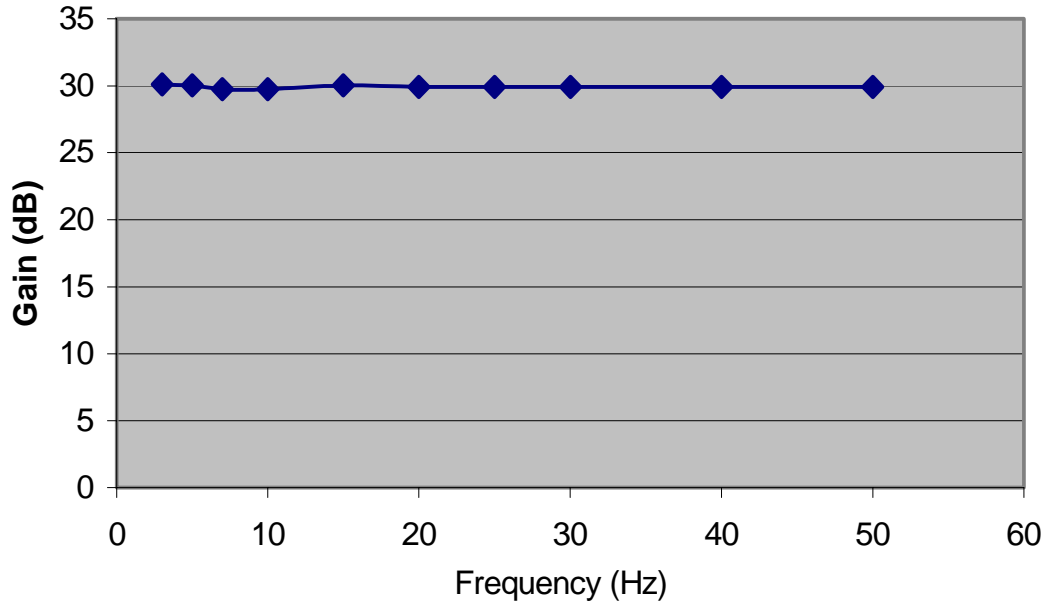


Figure 24: Switching Amplifier Frequency Response.

is very reasonable for a fielded weapon. In comparison a significant degradation in system performance is observed when the traditional linear amplifier is used.

1.6. INSTAR DEMONSTRATION

To validate the actuation system authority, the actuator was integrated into a one dof, open-loop INSTAR prototype. The actuator was contained in a 130 gram steel housing mounted

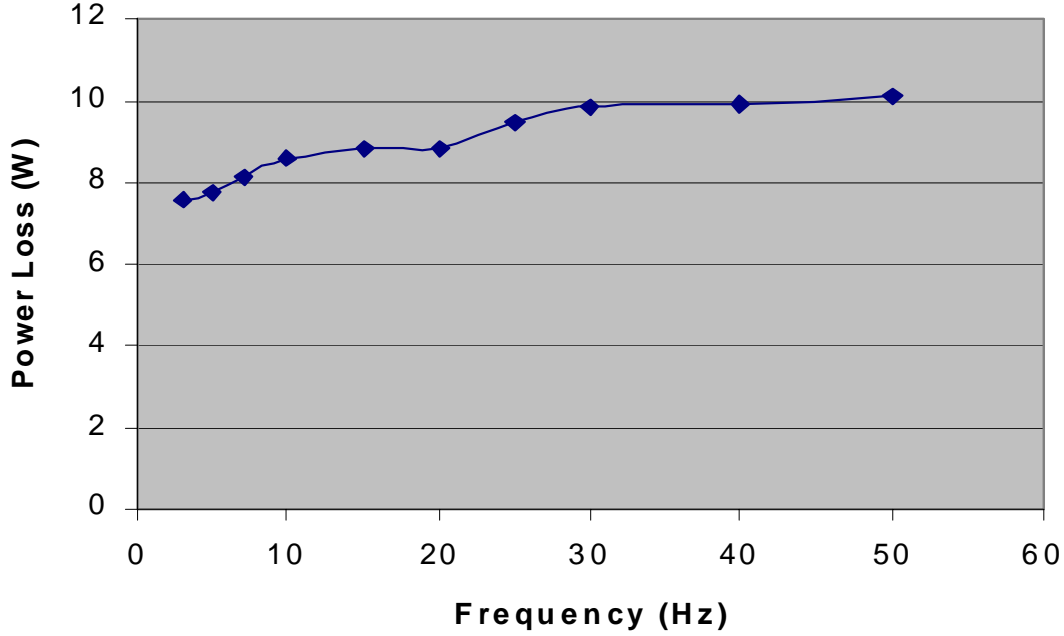


Figure 25: Power Loss.

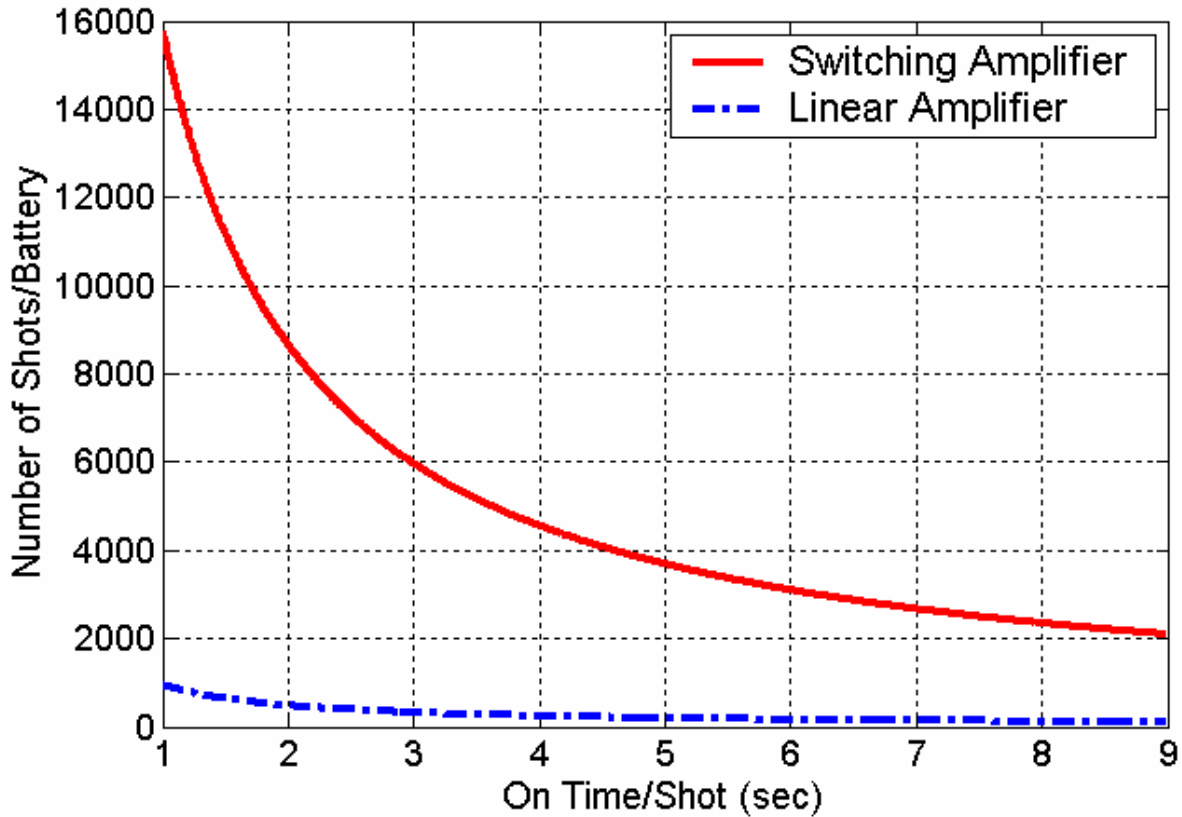


Figure 26: Number of Shots/Battery Comparison of Switching and Linear Amplifier.

to the bottom of a 7.62 mm rifle with a composite barrel (Figure 27). The stock of the rifle rested upon a fixture while the barrel was free to rotate with respect to the stock via a pivot. The force from the actuator was transferred to the barrel via a plunger, which made contact with the barrel 193 mm from the pivot. The springs were placed at a distance of 100 mm from the pivot to keep the actuator in touch with the barrel. Three tests were conducted: 1) no spring, 2) compliant spring (1.3 N/mm) and 3) stiff spring (9.1 N/mm). For each of the three tests the actuator was energized through its entire range of motion and the corresponding rifle point-of-aim motion was measured. A laser pointer was mounted to the barrel tip and the motion was detected on a wall 100 meters from the pivot point. This data was extrapolated through triangulation for 400m. All measurements were made relative to the neutral position.

For the Recurve, Figure 28, the total motion of the point-of-aim was 2.26 m with no spring, 2.05 m with the compliant spring, and 1.46 m with the stiff spring. For the d33 mode actuator, Figure 29, the measured peak-to-peak displacement was 1.91 m with no spring and 2.08 m with the compliant spring. The stiff spring experiment was not conducted for the d33 actuator because the height of the actuator exceeded the allowable space. The colored band in both graphs indicates the design target range for the point-of-aim. Both the actuators met the INSTAR requirements and on the upward stroke exceeded them (1.62 m for Recurve and 1.57 m for d33 mode with a compliant spring), thus indicating that the actuation systems have the needed control authority. As expected for the Recurve, the range of motion is higher in the

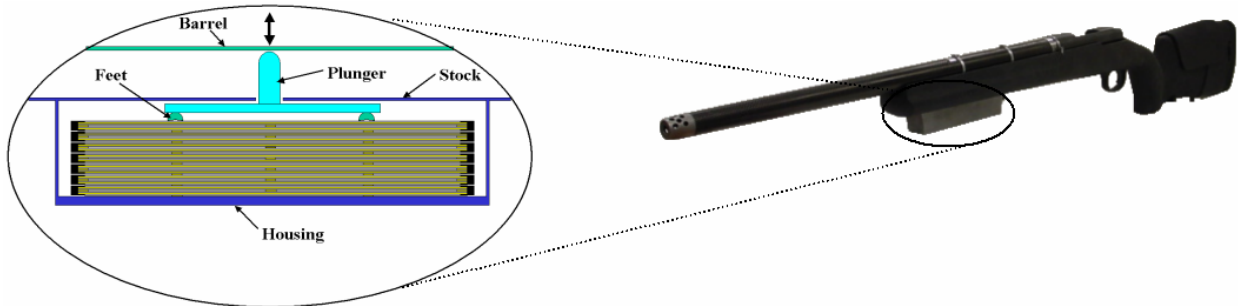


Figure 27: Prototype 7.62 mm Rifle with Actuator Mounted in Housing.

upward elevation (1.7 m no spring, 1.6 m compliant spring, 1.07 m stiff spring) because the actuator bottoms out in the downward motion (-0.561m no spring, -0.436m compliant spring, -0.394m stiff spring) as previously observed. If the bonding layers between serial Recurve elements are manufactured as designed it is expected that the point-of-aim would also exceed the specifications in this direction. It is interesting to note that although the d33 mode actuator achieved more upward stroke on the benchtop experiments, the Recurve achieved more upward stroke in the INSTAR demonstration platform because the stiffness of the Recurve (43.3 N/mm) is closer matched to the system (48.125 N/mm) than the d33 mode actuator (237.5 N/mm); thus, it transfers energy more effectively. This is further proven when the stiffness of the INSTAR system is increased. As the INSTAR spring stiffness is increased, the Recurve stroke is diminished, especially in the upward motion that was more compliant. In contrast, the d33 mode stroke increased slightly. This result is attributed to the insufficient internal preload in the compliant amplifier-actuator assembly, which is actually helped by the external preload and better stiffness matching with the INSTAR system. The selection of the spring would be dependent on the rifle manufacturer and shooter; however, in most cases the stiffer spring will be preferred.

1.7. CONCLUSIONS

The goal of this research was to develop a *complete* piezoelectric actuation system (integrated electronics, material transduction and Active Compliant Transmissions (d31 and d33)) that met the need of a broad range of applications that have very strict volume and weight constraints and require simultaneously high force and stroke. One such application is INSTAR, designed with an active suspension to eliminate aiming error sources by stabilizing the barrel assembly relative to the stock. The INSTAR application required moderate displacements (± 200 to ± 400 micrometers) with forces (6 to 44.5 N) at a quasi-static frequency (~ 10 Hz). The problem was challenging because of the constraints on volume and weight, demanding high energy density and specific work. The focus was on achieving efficient energy transfer by matching the actuator and system stiffnesses.

Two different approaches were explored to meet this need: 1) a d31 approach based on the Recurve architecture with focus on generating higher forces than is common for d31

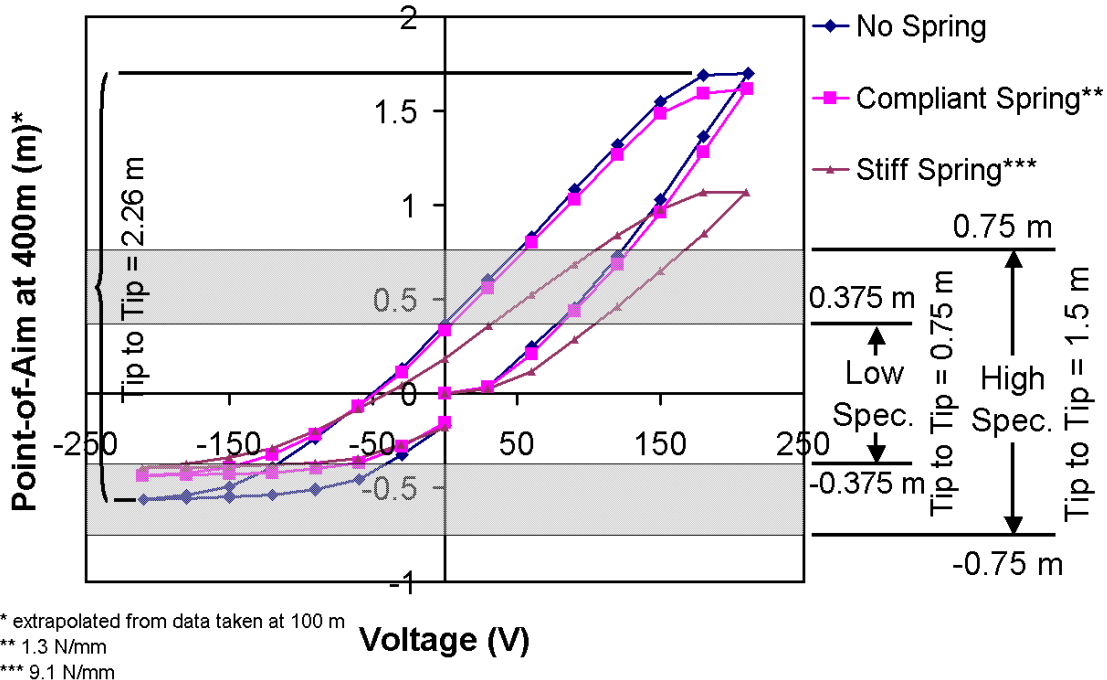


Figure 28: INSTAR Prototype Test Results for Recurve Actuator.

actuators and 2) a d33 approach based upon a compliant mechanism designed using topology optimization with focus on providing more amplified strain than is common for d33 actuators. Both actuators were optimized for this application and proof-of-concept prototypes were built.

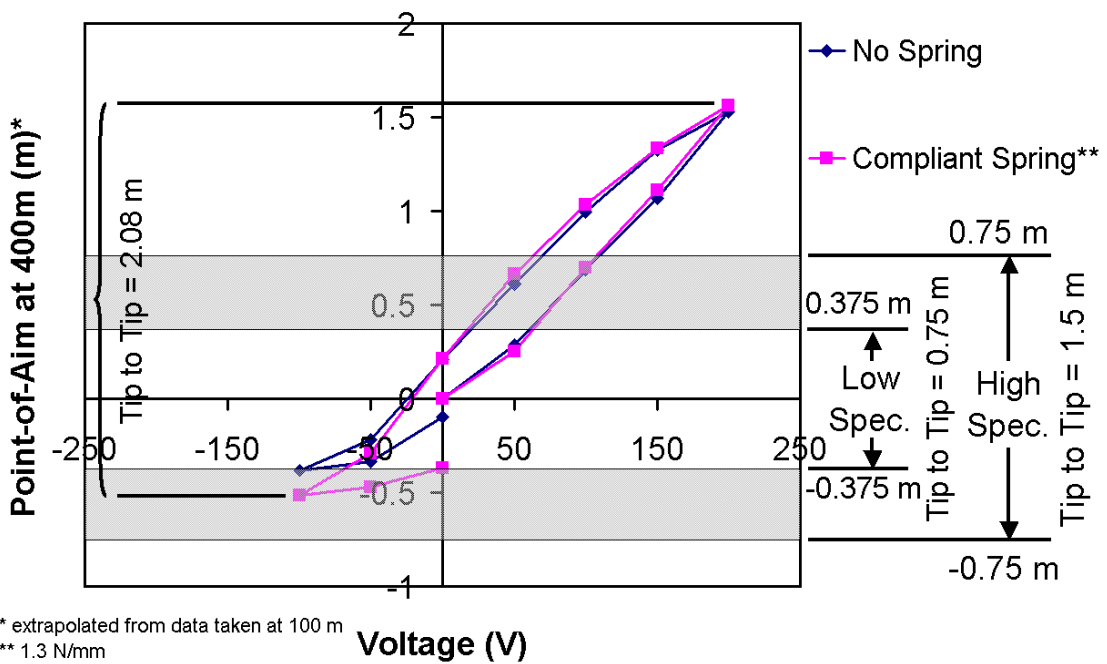


Figure 29: INSTAR Prototype Test Results for d33 Mode Actuator.

These prototypes were experimentally tested initially on the benchtop to characterize their force-displacement behavior and then integrated into the INSTAR demonstration platform for system testing. The experimental results highlighted the need for stiffness matching to achieve the best energy transfer. In benchtop testing both actuators met the force-displacement requirements, with the d33 mode actuator exceeding the Recurve on the upward motion. However, in the INSTAR demonstration platform, the Recurve achieved the highest Point-of-Aim motion (2.26 m) because its stiffness was matched closer to the INSTAR system. There were tradeoffs between the two actuators stemming from the common issues surrounding the approach utilized. For example, the d33 mode actuator provided more blocked force and was lighter –common to externally leveraged schemes. In contrast, the Recurve provided more free deflection and was more compact – common to internally leveraged schemes. *What was unique in this research was the large strokes achieved by the d33 mode actuator – over 0.9 mm and the large forces achieved by the Recurve actuator – over 45 N.* This demonstrates that either type of architectural approach can be driven to meet the requirements of midrange applications through optimal design. The supporting power electronics were based upon PWM switching technology powered by batteries. The battery life for a 9V battery with 2 sec trigger time is projected to be thousands of shots.

While this proof-of-concept study was successful, there still exists many issues that need to be investigated before this actuation system can be utilized in a fielded system. The primary issue is reliability. During the course of this research many measures were taken to mitigate mechanical failure. To offset the vulnerability of the piezoceramic in tension, it was precompressed during actuator fabrication. In addition, the housing was carefully designed to eliminate all load paths except for that perpendicular to the barrel along the line of actuation movement. This protects the actuator from recoil. Along the line of actuation, special stops were included to protect the actuator from any impact, such as that arising from a gun being used to butt in a door. However, due to the limited scope and time of this study, reliability test couldn't be performed and would be a natural extension of this work. Further work is needed to refine the electronics design to maximize the efficiency. The packaging of the electronics commensurate with the space available in the gun also needs to be addressed. Additional steps should be taken to optimize the actuation system, including integrating all the design tools developed during the course of this research into one so that the electronics and actuator mechanics can be simultaneously optimized. This will be useful for many applications beyond INSTAR that have similar needs and constraints. There are many packaging issues that remain to be addressed and many fabrication issues that once resolved could lead to as much as a 20% increase in performance. Finally, the refined actuation systems should be integrated and tested within INSTAR under firing conditions to quantify the impact of the active suspension on shooter accuracy.

It is of interest to quantify exactly what sort of effect the reduction of shooter induced disturbances will have on the average soldier. The army marksmanship unit classifies soldiers based upon a test in which the soldier shoots at pop-up targets at distances of 50 to 300 meters from a prone position and standing in a foxhole. The shooter must hit at least 23 of 40 targets to qualify as an Army Marksman. Soldiers who hit 30 targets qualify as a Sharpshooter and those who hit 36 are qualified as Expert. A soldier must qualify as an Expert in order to enter sniper training. The army has determined that 90% of errors associated with shooter accuracy are the result of aiming errors while the remaining 10% are caused by ammunition dispersion. Shooter-

induced disturbances constitute about 20-25% of the aiming error, but vary with weapon system and shooter skill. Therefore, elimination of shooter-induced disturbances can increase accuracy by up to 25%. This correlates to an improvement of 8 successful shots in the marksmanship test, which would improve the shooters qualification to the next level.

This improvement in performance will have a dramatic effect on the infantry fighting force. It would provide a much needed alternative to the training based approach. It will lead to a significant increase in overall marksmanship enabling mission requirements to be met that had previously been assigned to higher skilled or trained personnel. It will lead to an improvement in fire accuracy, especially at long ranges in combat due to improved rifle aim stability and less need for the soldier to assume and maintain a steady position. Less ammunition will be needed in combat situations enabling an increase in stowed kills and reducing the need to resupply ammunition under adverse conditions. But most importantly it will increase soldier survivability and mission effectiveness.

1.8. REFERENCES, SECTION 1

Brei, D., Vendlinski, J., Lindner, D.K., Zhu, H., LaVigna, C., 2003, "Development and Demonstration of INSTAR – Inertially Stabilized Rifle," *Proceedings of the SPIE - The International Society for Optical Engineering*, paper # 5056-33.

Canfield, S. and Frecker, M., 2000, "Topology Optimization of Compliant Mechanical Amplifiers for Piezoelectric Actuators," *Structural and Multidisciplinary Optimization*, 2000. 20(4): pp. 269-278.

David, W.C., 1995, "Preparing a Battalion for Combat: Marksmanship," *Infantry*, July/Aug 1995, pp 27-30.

Ervin, J., and Brei, D., 1998, "Recurve Piezoelectric-Strain-Amplifying Actuator Architecture," *IEEE/ASME Transactions on Mechatronics*, 3(4), pp. 293-301.

Ervin, J., 1999, Design, Characterization, and Assessment of the Recurve Actuation Architecture, PhD Dissertation, University of Michigan.

FM3-22.9 Rifle Marksmanship M16A1, M16A2/3, M16A4 and M4 CARBINE, Headquarters of the U.S. Army, April 2003.

FM 23-10 Sniper Training. Headquarters of the U.S. Army. Washington D.C. August 1994.

Frecker, M. and Canfield, S., 2000a, "Design of Compliant Mechanism Amplifiers for Piezoceramic Stack Actuators Considering Stiffness Properties," in *Proceedings ASME International Mechanical Engineering Congress and Exposition, Dynamic Systems and Control, Special session on Flexural Joints and compliance modeling*. Orlando, Florida.

Frecker, M. and Canfield, S., 2000b, "Optimal Design and Experimental Validation of Compliant Mechanical Amplifiers for Piezoceramic Stack Actuators," *Journal of Intelligent Material Systems and Structures*. 11(5): p. 360-369.

Giurgiutiu, V., Chaudry, Z., and Roger, C. A., 1997, "Design of Displacement Amplified Induced Strain Actuators for Maximum Energy Output," *ASME Journal of Mechanical Design*, Vol. 119, No. 4, December 1997, pp. 511-517.

Joint Publication 3-06, Doctrine for Joint Urban Operations, 16 September 2002, page vii.

Lindner, D.K., Zhu, H., Song, C., Huang, W., Cheng, D., 2002, "Low Input Voltage Switching Amplifiers for Piezoelectric Actuators," *Proceedings of SPIE's 2002 North American Symposium on Smart Structures and Materials: Industrial and Commercial Applications of Smart Structures Technologies*, Anne-Marie McGowen, Ed., San Diego, CA

Samuelson, M and Garcia, E., 1997, "Actuator Systems for Precise Motion Control", Advances in astronautical sciences, *Proceedings of the 1997 Annual AAS Rocky Mountain Guidance and Control Conference*, v94, Breckenridge, CO, Feb 5-9 1997.

SECTION 2. PROOF-OF-CONCEPT INVESTIGATION OF ACTIVE VELCRO FOR SMART ATTACHMENT MECHANISMS

Investigators:

Diann Brei, PI, Associate Professor, Mechanical Engineering Department, University of Michigan, Ann Arbor, MI 48109-2125

Joseph Clement, Ph.D Graduate Student, Mechanical Engineering Department, University of Michigan, Ann Arbor, MI 48109-2125

2.1. INTRODUCTION

2.1.1. Motivation

The Air Force Command Integrated Product Team for Micro-satellites Missions has identified space control, surveillance and logistics as high priority future capabilities. Micro- (< 100 kg) and nano- (<10kg) satellites address these by offering a new paradigm for how space operations are conducted. These satellites would have the same capabilities as existing satellites but would have significant reduction in cost and weight. The reduction in cost would enable a large number of them to be launched into space for operations such as distributed satellite (or constellation) systems for space surveillance and unlimited aperture sizes along with reconfigurability. The reduction in weight enables these satellites to be launched quickly from high altitude planes such as the F-15 or F-22. Thus, these satellites could be deployed anytime and anywhere to significantly assist in space control enabling satellite denial and threat warning and identifying unknown space objects launched from foreign countries. Finally, these smaller, inexpensive satellites would assist in on-orbit servicing of more expensive satellites and space systems allowing these systems to be updated by replacing outdated components, restoring expendables and inspecting the system to assess damage and estimate remaining lifetime.

On-orbit servicing will greatly increase the lifetime and long-term usability of satellites. One important key to on-orbit servicing by micro- and nano- satellites is the ability for the smaller satellite to dock to the mother satellite or space system. However, current technology (probe and cone, tether approaches, etc) can be expensive, bulky and have other difficulties such as tether dynamics, guidance, etc. This application needs: an ample target surface on the mother satellite that will reduce the guidance requirement of the micro-/nano- satellite, a mechanism to precisely guide the guest satellite to the preferred docking position while maintaining engagement, and once the task is completed a means to release the satellite.

While devices to connect objects tend to be passive and can't fit this need, there are distributed actuated surfaces have been used in the past for part conveyance, both at the micro- and macro-scales. Distributed manipulation surfaces are comprised of many actuators arranged

in a dense array. By utilizing the combined effort of the actuators, much like the manner in which the cilia of the respiratory tract translate material or the legs of the centipede generate locomotion, the surface can generate motions over greater distance with larger forces than achievable with a single point actuator while maintaining a high resolution. In addition complex motions such as orientation and path planning can be achieved. Macro-scale conveyance systems have been used for decades in manufacturing with current research in novel actuation (Tadokoro et al., 1998), self-reconfigurable robots (Yim et al., 2000) and autonomously positioning/orientation control algorithms (Luntz et al 1999a, 1999b, 2000). Both Yim and Luntz's systems can clearly handle large loads and can autonomously position, however they are also clearly too bulky, heavy, complex and inappropriate for space applications. There has been significant research in the past years on micro-scaled distributed manipulation using MEM techniques resulting in thermally activated (Suh et al., 1999; Ebefors et al., 1999; and Ataka et al., 1993), electrostatically driven (Langlet et al., 1997), magnetic levitation (Iizuka and Fujita, 1997, Nakazawa et al., 1997), resonators (Bohringer et al., 1994, and 1999) and air jet distributed surfaces (Konishi and Fujita, 1994). But as Table 2.1 summarizes, the positioning force and out-of-plane lifting is very low, typically microNewtons and a few grams, limiting their practical use.

More significantly, the approaches at both the macro- and micro- scale rely on gravity to maintain engagement between surfaces. This constrains their use to stable, horizontal, non-moving environments experiencing gravitational forces. However, there are many environments that do not fall within this constraint including low-gravity, fluidic, and vibratory environments. Additionally, inverted or vertical positioning is impossible even within a stable laboratory environment without undesired surface separation. For these environments it is necessary to maintain an explicit connection during motion. Unfortunately, no existing connection method can simultaneously achieve planar motion and none of the existing state of the art manipulation surfaces have retention capabilities.

Table 2.1: Relevant State of the Art Distributive Manipulation Systems*

| Author | Operating Principle | Maximum Speed | Lifting Capacity | Positioning Force | Notes |
|---|---|---------------|--|--------------------|--|
| Fujita et al, 1990 Iizuka and Fujita, 1997 | Superconducting Magnetic Levitation Electromagnet propulsion | 7.1 mm/s | magnets 8 - 38mg | not reported | Requires low temp < 90K 40 μ m precision 2.8 mm - stroke |
| Nakazawa et al., 1997 | Electromagnetic levitation and propulsion | 30 mm/s | magnets w/ ext. load 1.2 g | 40 mN | 40 mm ² active surface 32 turn coils |
| Pister et al., 1990 | Pneumatic levitation Electrostatic propulsion | slow | silicon wafers < 1.8 g | not reported | 1-2 Hz 100-500 μ m per cycle |
| Konoshi and Fujita, 1994 | Pneumatic levitation and propulsion | 5 mm/s | silicon wafers < 1 mg | not reported | 63 actuators 2mm x 3mm array Electrostatic micro-valves |
| Hirata et al., 1998 | Pneumatic levitation and propulsion | 50 mm/s | silicon sliders 15.3 – 60 mg | 20 μ N | Best operation with finely ridged sliders |
| Ataka et al., 1993 | Thermal bimorph | 0.5 mm/s | silicon wafers < 2.4 mg | not reported | 512 actuators 1cm x 1 cm array < 10 Hz |
| Bohringer et al., 1997 Terry et al., 2001 | Thermal bimorph | 0.24 mm/s | 250 μ N/mm ² | not reported | 1024 actuators 4 chips: 1 cm ² each |
| Suh et al., 1997, 1999 | Thermal bimorph | 0.2 mm/s | silicon wafers 8.6 mg 23 μ N/mm ² | not reported | 256 actuators 9.4 mm x 9.4 mm array |
| Ebefors et al., 1999 | Thermal multi-jointed bender | 12 mm/s | silicon wafers w/ ext. load > 2.1 g | not reported | 12 actuators 15 mm x 5 mm array < 3 Hz |
| Liu et al., 1995 | Magnetic flaps | 2.6 mm/s | silicon and glass chips < 222 g | not reported | 224 flaps 10 mm x 10 mm array |
| Inoue et al, 1996 | Electromagnetic propulsion | 79 mm/s | magnets < 1 mg | $O(10-100\mu N)**$ | ** Estimated from specified speed mass and displacement |
| Furuhashi et al., 1991 | Piezoelectric and electrostatic pin actuators | not reported | not reported | not reported | Only simple observational tests performed |
| Bohringer et al., 1994, 1999 | Electrostatic torsional resonators | slow | silicon wafers 100 μ N/mm ² | not reported | 11000+ actuators 0 – several hundred kHz |
| Tadakoro et al., 1998 | ICPF gel actuators | 0.62 mm/s | < 24 mN | not reported | Soft manipulators require liquid bath |
| Safaric et al., 2000 Ku et al., 2001 | Pneumatic levitation and propulsion | < 8 mm/s | not reported | not reported | 100 capillary tubes 4mm x 4mm array |
| Luntz et al., 1997 | Wheeled positioning | not reported | cardboard boxes | not reported | Reconfigurable 13 cm square modules with distributed control |

* Table based on the work of Ebefors et al., 1999

2.1.2. Research Goals and Objectives

This research establishes a different technology base, **Smart Attachment Mechanism** or SAM. The SAM concept is a connective device that has the ability to adjust with large motion generation while maintaining the engagement of the two bodies. This is a significant paradigm shift and opens the doors for a new class of devices and capabilities. The goal of this effort was to establish the initial foundation for this new paradigm by developing a smart attachment technology capable of actively connecting two surfaces (engagement, retention and release) and generating relative planar motion (translation, rotation) between the two connected surfaces. The specific project objectives for this three year study were:

- **Create New Technology** – Design the fundamental SAM technology that possesses the primary functions of an active connection (engagement, retention, release) and controlled motion generation during connection (translation, rotation).
- **Develop Predictive Operational Models** – For this new technology, derive the governing behavior models for the primary functions (engagement, retention/release and positioning) accounting for the highly discrete actuator array, limited available motion vectors, and the interference generated during relative motion of the host and guest surfaces. These models will be used as analytical and synthesis tools to understand engagement/retention forces, load carrying capability, positioning force, kinematics of the mechanism, and stresses generated during operation, path planning, optimal surface pattern and topology, etc.
- **Demonstrate and Evaluate Proof-of-Concept System** – Design, construct and experimentally validate a basic proof-of-concept SAM system with the primary functions: engagement, retention, release, and motion generation. Develop simple control laws (translation, rotation, path planning) and define manufacturing protocol for rapid fabrication of prototypes.

2.1.3. Report Overview

This report is organized with respect to the three objectives: Active Velcro Design and Operation, Operational Models and Validation, Proof-of-Concept Demonstration and Evaluation. *Active Velcro Design and Operation* describes the overall device structure of the chosen design, nicknamed Active Velcro, including the connection topology, surface pattern and actuation method. Primary design and research issues are discussed in detail for each key component. The primary gaits are explained along with how the device can be scaled up to multiple posts and the advantages to the increased redundancy such as damage control, reliability, and phased actuation.

An extensive part of this research was the derivation of the behavioral models presented in *Operation Models and Validation*. Analytical models capturing the quasi-static force-deflection behavior of the complex Active Velcro mechanism under general loading conditions were derived and applied for specific cases of engagement, retention and positioning. All models were based upon the Matrix Displacement approach outlined by Pestel and Leckie, 1963, which ensures straight forward scalability to capture the response of both simple single actuator devices

and complex surfaces containing many actuator elements. The scaling procedure is demonstrated for a general repeatable unit, a two actuator Smart Attachment Mechanism. The validity of the models was experimentally verified under three common operating scenarios: free deflection, surface positioning and guest surface engagement/retention. The impact of manufacturing effects, friction, and plastic deformation are discussed.

A variety of proof-of-concept prototypes were fabricated and experimentally characterized. The *Proof-of-Concept Demonstration and Evaluation* describes the initial large scale prototype fabricated from off the shelf components that demonstrated the primary functions of engagement, retention and positioning. An optimized reduced scale prototype fabricated utilizing stereolithography methods is presented with a refined guest surface pattern for improved rotational performance, implemented flexible path-planning algorithms for autonomous route finding, and a basic stamp control system with onboard power supply to enact the chosen routes forming a fully functional portable demonstration system. Both systems successfully demonstrated the primary functions with useful loads, speeds and control authority for a broad range of applications including docking of micro-/nano- satellites.

2.2. ACTIVE VELCRO DESIGN AND OPERATION

Smart Attachment Mechanisms are a new breed of connection methodology that engages two surfaces together and effects relative motion. There are three primary modes of operation depending on the active state of the two surfaces being joined:

Docking Mode

In the *Docking* mode, a large active host surface is used to manipulate a smaller inactive guest surface. With this configuration, the host surface contains all the power, actuation, and control systems while the guest surface can be made inexpensive, lightweight and small. Applications for the docking mode include the docking of satellites in space or unmanned underwater vehicles (UUVs) beneath the sea. Both these applications require a system that can manipulate objects while securing the object from separation throughout the manipulation process. In the case of satellites, a SAM would reduce the cost, weight, volume and complexity of the guidance system of the micro-satellite shifting that responsibility to the host satellite that benefits from increased adaptability and extended life. Additional applications include the sorting of materials in unstable environments such as aboard moving vessels or in low gravity environments, smart latches for weight driven applications such as gossamer structures where the ability to satisfy multiple functions (latching, deployment, and moderate position control) is crucial, or attachment points for radar antennas to form configurable arrays for the scanning of large areas.

Locomotion Mode

The roles of the host and guest surfaces can be reversed by having the active elements placed on the guest surface, which then walks along a large inactive host surface. This *Locomotion* mode is ideal for applications such as part conveyance or the inspection of large bodies. By placing the active elements on the smaller guest surface the number of actuators is reduced without impairing the ability to cover great spans. Furthermore, since the size of the active surface is limited, it may become cost effective to fabricate large numbers of guest

surface walkers to simultaneously and independently transport objects across large areas, be they factory floors for materials handling, space station exteriors for personnel or material transport, or naval ships for munitions transport. Alternatively, the locomotion mode may be employed to perform hazardous tasks such as hull inspection of ships at sea or the exploration of environmentally dangerous fluid piping systems.

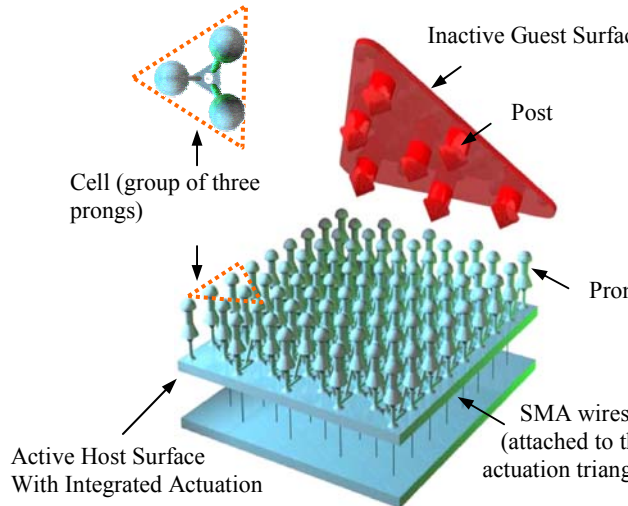
Morphing Mode

Finally, the active elements could be placed on both the host and guest surfaces. This would allow surfaces to move as needed across each other to effect radical shape change such as macro-scale adjustment of space optics or the creation of self-assembly structures. As such this mode can be termed the *Morphing* mode of the SAM. In addition to creating highly adaptable structures, the morphing mode could simply be used as a means to increase reliability since either the guest or host surface could be employed as the driver.

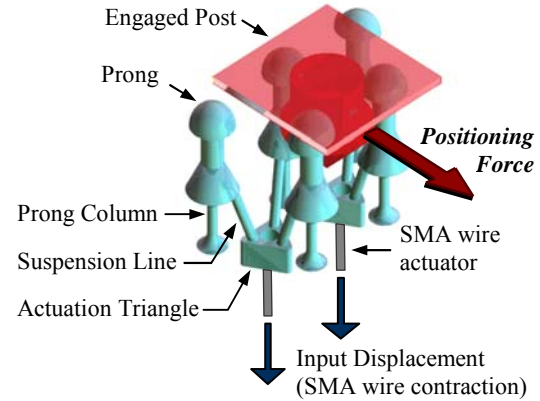
For any of these modes, smart attachment mechanisms are useful for applications where relative motion must be effected while keeping the surfaces engaged in environments such as space where gravity cannot assist or in unstable environments such as aboard a naval vessel. The specific mode of operation would be chosen based on the intended application. As a first step in the development of this new type of technology, the docking mode was explored in this research. It is foreseen that the lessons learned from the exploration of the docking mode can be applied to future studies on the potential of the locomotion and morphing modes.

2.2.1. Active Velcro Architecture

Since SAMs are a totally new technology, there has been no previous research or devices to utilize. Therefore, it was crucial to develop an initial concept to aid in the development of the fundamental operational theories. While several concepts were generated, because of the three year scope of this project they were downselected to one concept nicknamed Active Velcro. Active Velcro is a two surface mechanism designed to offer full planar translation and rotation capabilities while providing a positive retention force between the surfaces (Figure 2.1). One surface serves as the host, comprised of a highly redundant hexagonal array of active *prongs*, as well as the actuation, control, and power systems. The second surface serves as a guest, comprised solely of a sparsely patterned array of inactive *posts*. The two surfaces snap-fit together, similar to Velcro, when brought into contact by entrapping the post within a group of three prongs, termed a *cell*. Once in contact, the host surface is activated to position and orientate the guest surface to the desired location. Because the surfaces are secured to each other passively, retention requires no power and thus provides a predictable power-off hold capability. The three main system considerations for this device where the surface pattern, connection topology and actuation system.



a) Active Velcro System



b) Close-Up (Three Cells Shown)

Figure 2.1: Active Velcro System Overview. a) Active Velcro consists of two surfaces: one inactive guest surface with a sparse arrangement of posts and an active host surface with a densely distributed array of actuated prongs. The host surface contains all the actuation, power and control systems and when activated inches the guest surface to the desired position and orientation. b) The prongs are activated by straining SMA wires located at the center of alternating groups of three prongs (termed a cell). When a given SMA is energized, the deflection of the SMA wire acts on the center of the actuation triangle, which in turn distributes the work to the three attached prongs via three suspension lines.

2.2.1.1. Connection Topology

The topology of the posts on the guest and the prongs on the host interact to provide a snap-fit type of connection. For successful engagement, retention, and positioning there are a number of important design issues that must be addressed:

- When the guest surface approaches the host prong system at a random orientation and angle of incidence, each post should be guided and aligned into the center of a prong cell instead of bouncing off the surface (Figure 2.2a).
- Post engagement should require a minimum of force and occur passively so that the system doesn't always have to be powered (Figure 2.2b,c).
- The force required to separate the surfaces should be large enough and more than engagement to prevent premature separation (Figure 2.2b,c).
- Any topology that is chosen must not impede relative motion of the surfaces. Thus, the topology must allow the post to slip between the prongs during translation and rotation of the guest surface (Figure 2.2d).

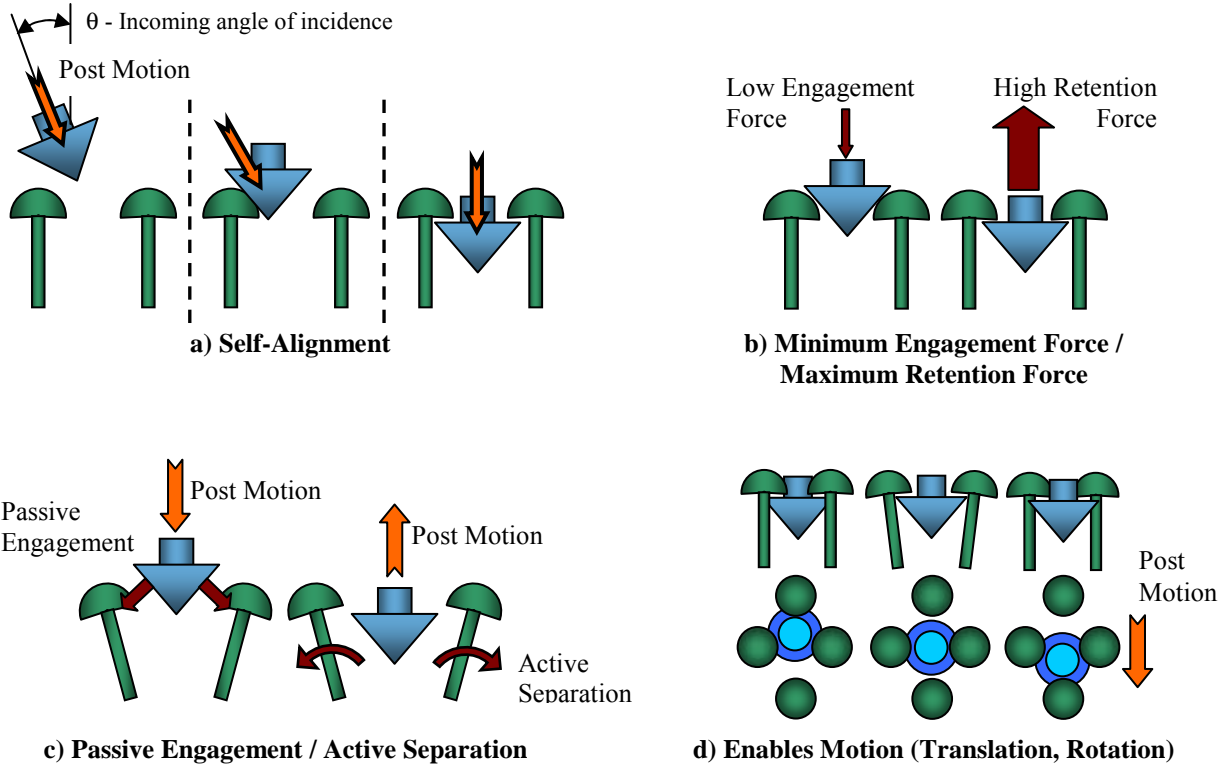


Figure 2.2: Connection Topology Requirements. **a)** The shapes of the guest surface posts and host surface prongs must permit engagement over a substantial range of incidence angles. **b)** The engagement force must be small enough to assure engagement while the retention force must be large enough to prevent undesired guest surface separation. **c)** Engagement and retention must occur passively to insure power-off capture and hold capabilities. Separation should require activation of the host surface prongs. **d)** The connection topologies must not interfere with the motion capabilities of the mechanism.

Fortunately, the connection forces (engagement, retention) and required forces for motion generation (translation, rotation) can be tailored by altering key features of the chosen connection topology. The surfaces most directly affecting connection and motion are depicted in Figure 2.3. The post and prong lead surfaces determine the engagement force. For example, elongating the lead surface of the prongs from a spherical to a conical shape reduces the engagement force without affecting either the retention or positioning forces. The trailing surfaces of both the post and prong determine the retention force. Increasing the slope of the prong's trailing surface reduces the retention force without affecting engagement or positioning forces. The support columns and diameters of the connecting heads of both the post and prong primarily impact the positioning force. Decreasing the diameter of the support column for the guest surface post with respect to a given prong head diameter increases the positioning force by allowing the post to easily slip through the channels in the host surface array, thereby reducing any interference to motion. Mathematical models for this interaction are given in *Section 2.3 Operational Models and Validation*.

2.2.1.2. Surface Pattern

The overall pattern and spacing arrangement of the prongs/posts are critical for motion and connection. Improper arrangement can lead to obstructions to motion or high actuation

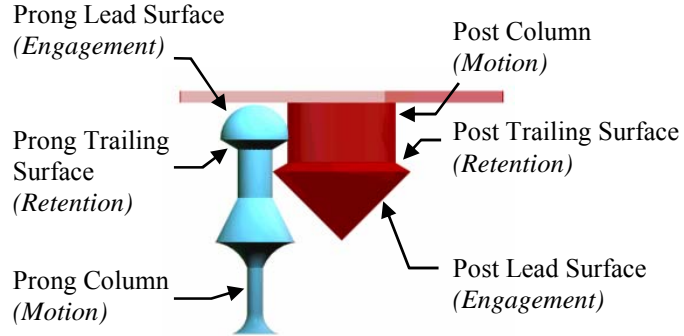


Figure 2.3: Sample Connection Topology. The surfaces most directly affecting engagement, retention, translation, and rotation can be independently tailored. For example, if the cone angle of the post's lead surface were changed, the engagement characteristics would be altered without affecting either the retention or motion characteristics of the mechanism. Increasing the slope of the prong's trailing surface reduces the retention force without affecting engagement or translation forces. Decreasing the diameter of the support column for the guest surface post with respect to a given prong head diameter decreases the required forces for translation because the post can easily slip through the channels in the host surface array.

requirements. In addition, the prongs must be positioned on the host surface in such a manner that engagement and retention are independent of guest surface location or orientation. Key is selecting a repeatable pattern that has open pathways between the connection topology so that motion is feasible, such as depicted in Figure 2.2d which allows a step of translational motion downward.

Most of the current state of the art distributed manipulation surfaces use a simple Cartesian (rectangular) or a hexagonal array of identical repeat units. The Cartesian pattern lends itself well to translational motion since the actuation elements are aligned in a rectangular array; conversely, the hexagonal array is ideal for rotation because of the circular repeat units that reduce interference. However, a hexagonal pattern can nominally overcome the translation barriers through a saw-tooth path (Figure 2.4 b) even when scaled up, whereas rotation becomes

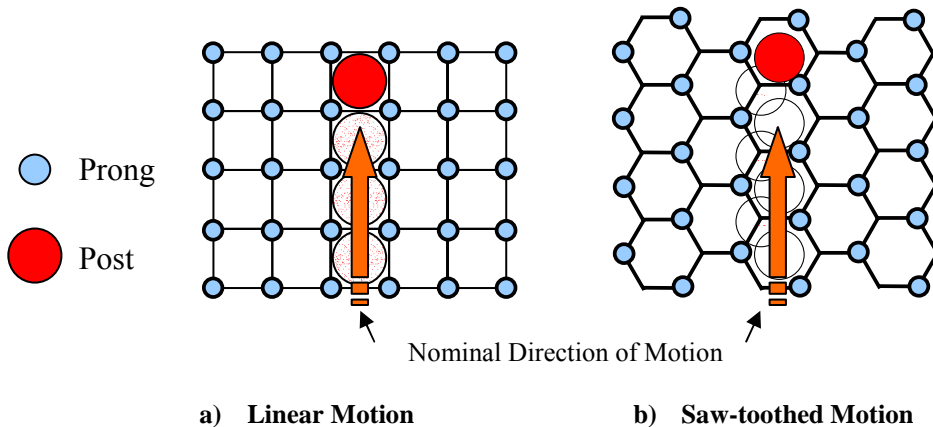


Figure 2.4: Linear vs. Saw-toothed Motion. **a)** A rectangular prong array allows purely linear translations. **b)** A hexagonal prong array does not allow for pure translation, instead requiring a saw-toothed motion.

very difficult with a Cartesian pattern when multiple posts are employed. It should be noted that a hexagon is the largest order regular polygon that can completely fill a space without leaving voids in the array. Voids are clearly undesirable since they could result in loosing a connection or stopping forward motion.

In addition to the rotational capabilities, another advantage to hexagonal patterns is that they take less power because of a small step size. Consider the Cartesian array of prongs depicted in the left side of Figure 2.5a which results from a four-pronged cell and the hexagonal array of prongs depicted in Figure 2.5b resulting from a three-pronged cell. Successful positioning requires that actuators must be able to move the guest post from one cell to the next. Thus a successful handoff requires that the centroid of the post move just over half the distance between adjacent cells after which strain energy in the prong will attempt to guide the post towards the center of the new cell. Plane geometry reveals that the minimum required positioning distance for the three-pronged cell, A_{min}^3 , is 29% smaller than that for the four-pronged cell, A_{min}^4 ,

$$A_{min}^4 = \frac{\pi}{4} (R_{prong} + R_{post}) \quad (2.1)$$

$$A_{min}^3 = \frac{1}{2} (R_{prong} + R_{post}) \quad (2.2)$$

where R_{prong} is the nominal radius of the prong, R_{post} is the nominal radius of the post. Therefore a three-pronged system reduces actuator demands by 29% while simultaneously increasing the positioning resolution by 29% for given post and prong dimensions.

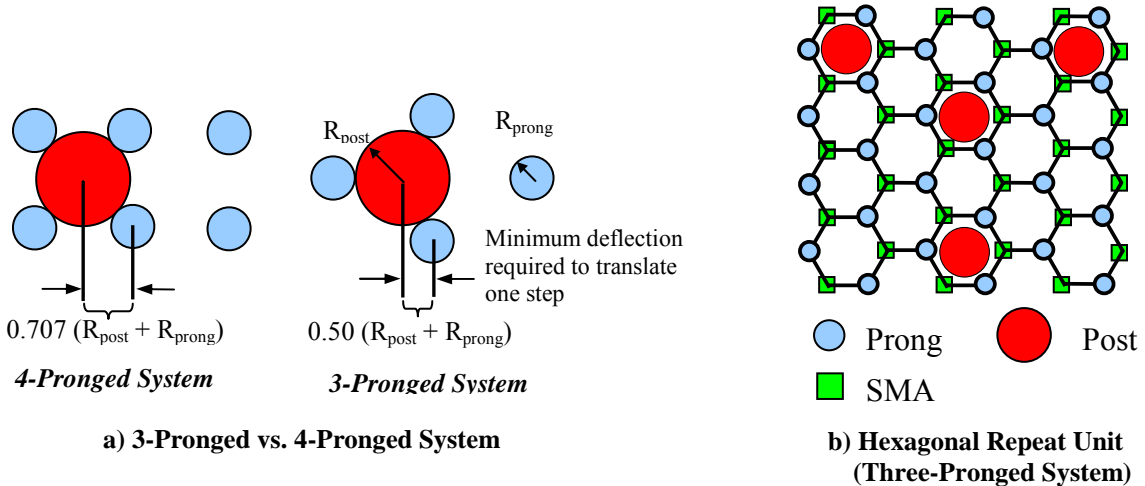


Figure 2.5: Hexagonal Repeat Unit. a) For given post and prong diameters, the three-pronged system results in a 29% improvement in system resolution with a corresponding 29% decrease in required actuator deflection when compared to a four-pronged system. b) The repeat unit of this array is a hexagon in which three corners of the hexagon are occupied by prongs and the remaining three corners are occupied by SMA wires. The hexagon is the largest order regular polygon that can be arrayed without leaving gaps in the pattern.

2.2.1.3. Actuation System

The active Velcro design achieves the hexagonal pathways through an array of hexagonal repeat units where a prong is positioned on three corners and an SMA wire at the other three corners resulting in the triangular prong cell. This array insures that the every prong is surrounded by three SMA wires arranged at 120° enabling motion in any of six directions (0° , 60° , 120° , 180° , 240° , and 300°) depending on the combination of energized SMA wires (Figure 2.6).

Each cell, cell is activated by pulling down the triangle by a linear actuator (Figures 2.1b and 2.6). The choice of actuator technology is highly dependent on the scale of the host surface elements and the required actuator force. SMA actuators were chosen because of their ability to provide the required deflections ($\sim 0.7\text{mm}$) and force ($\sim 6\text{N}$) for the both the large and reduced scale proof-of-concept prototypes in a lightweight, easily controlled, low volume package. If the Active Velcro mechanism were reduced in scale to MEMS levels, alternative actuator sources should be considered such as piezoelectric (Furuhata et al., 1991), electrostatic (Pister et al., 1990, Furuhata et al., 1991, Bohringer et al., 1994), and thermal actuation (Ataka et al., 1993, Bohringer et al., 1997, Suh et al., 1997, Ebefors et al., 1999). If the scale were increased, more traditional technologies such as solenoids, linear motors, or hydraulics may be necessary depending on the loading. While the design and models derived are generic, when necessary throughout this report SMA actuation will be considered for purposes of illustration.

2.2. Active Velcro Operation

A connecting guest surface is positioned relative to the host surface through pushing individual posts from cell to cell. Rotation is achieved by manipulating multiple posts. To

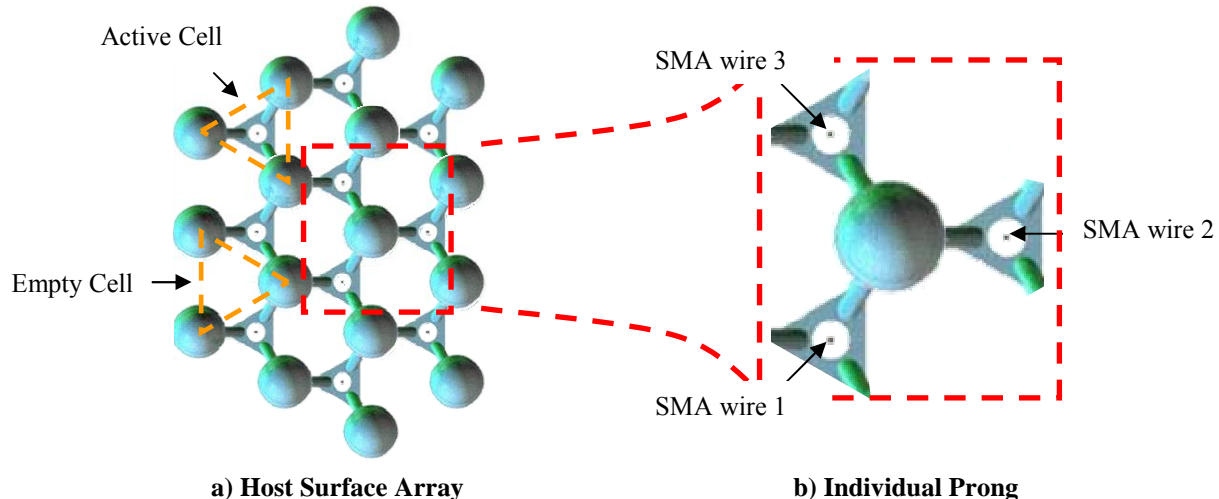


Figure 2.6: Cell Connections. **a)** All cells are linked together at the prongs such that every prong is tied to three symmetrically arranged SMA wires. Even though SMA wires are only incorporated in alternating cells, all prongs can still be deflected in any direction by energizing multiple wires simultaneously. **b)** For example, energizing SMA wire 2 causes the prong to bend to the right. Energizing SMA wires 1 and 3 causes the prong to bend to the left.

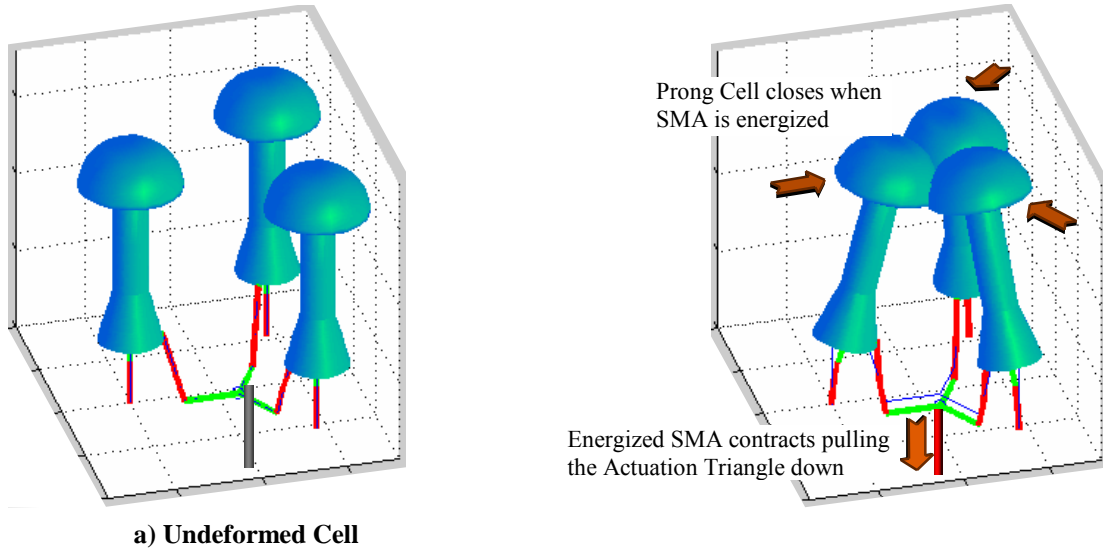


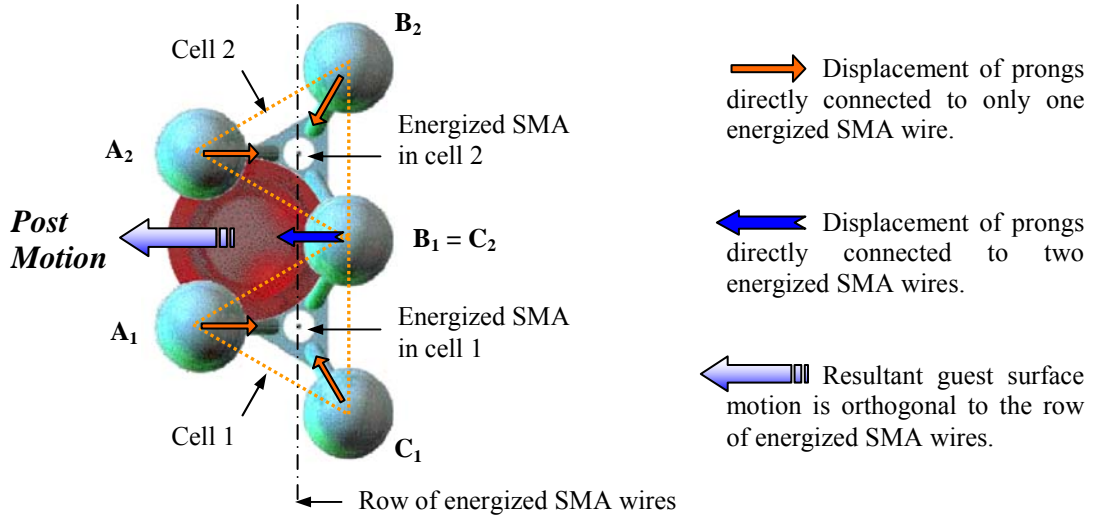
Figure 2.7: Single-Cell Grasping Action. Energizing a single SMA wire causes its cell to close in a grasping action. This action can be utilized to increase the hold on a guest surface post located in the cell.

advance a post to the next cell, the current cell is activated by electrically heating an SMA wire that is connected to the prongs via suspension lines attached to an actuation triangle (Figure 2.1b). When energized, the SMA wire contracts pulling down on the actuation triangle and the cell closes in a grasping action (Figure 2.7). The grasping action created by heating the SMA wire can be employed to increase the hold on a guest surface but by itself is insufficient to create relative motion between the two surfaces.

However, the interconnectivity of cells within the host surface can be exploited to create the more complex prong motions necessary to move the guest surface (Figure 2.6). SMA wires are only located in every other cell but because each cell is linked to its neighbors; all prongs are still directly connected to three SMA wires. Thus, a given prong can be deflected in any direction by energizing one, two or all three of the attached SMA wires. When two adjacent SMA wires are activated, both cells will attempt to close with the same grasping action of Figure 2.7, but the prong shared by both will move according to the resultant force vector which is oriented perpendicular to the line connecting the two energized SMA wires. Two basic gaits are used to generate motion in the guest surface depending on the location of the post.

2.2.2.1. Gait 1

The first gait, depicted in Figure 2.8, occurs when a post is located inside an *empty* cell (one without an SMA wire). If the SMA wires from the adjacent active cells are energized, the adjacent cells will attempt to close with the same grasping action, but the prong shared by both cells ($B_1 = C_2$) will move according to the resultant force vector which is oriented perpendicular to the line connecting the two energized SMA wires. This prong (B_1) pushes the post to the next cell completing one step of translation.



Post is located in Cell 3 (Not highlighted for clarity)

Figure 2.8: Local Prong Operation: Gait 1. If the post is located in a cell without an SMA wire it can be translated to the left of the figure by energizing two SMA wires. When the two SMA wires are energized prongs A_1 , C_1 , A_2 , and B_2 will deflect towards their respective attached and energized SMA wires. Both SMA wires act upon prong B_1 ; therefore its deflection is given by the resultant force vector created by the energized wire. As a result of the individual prong motions, prong B_1 pushes the post between prongs A_1 and A_2 to complete the translation. A similar process can be employed when the post is located in a cell containing an SMA wire only it requires the activation of three SMA wires to generate guest surface motion.

2.2.2.2. Gait 2

After this translation, the post is located in an active cell with an SMA wire and the second gait is employed (Figure 2.9). For this gait, three collinear SMA wires are energized simultaneously creating two shared prongs (B_1 and B_2). These two prongs, which had originally entrapped the post, will move perpendicular to the row of activated SMA wires and out of the way of the advancing post. The post is advanced by the unshared prong (A_2) which still deflects to the center of its cell; thereby pushing the post between prongs B_1 and B_2 and into the next cell. This new cell is empty and requires the first gait; thus, the cycle repeats.

2.2.2.3. Advanced Multi-Post Functionality

This process is continued over and over to inch the guest surface to the desired location in a saw-toothed motion (Figure 2.4b) and can be applied to one or many posts on the guest surface. There are many advantages to utilizing guest surfaces with multiple posts. First, all the forces increase linearly leading to scalability - positioning force for larger load carrying capabilities and retention force for higher hold ability- but it comes at the cost of increased engagement force (although this can be tailored down). Yet, multi-post guest have many other advantages including rotation due to post pairs, higher reliability and increased speed due to redundancy and phased activation.

→ Displacement of prongs directly connected to only one energized SMA wire.

↔ Displacement of prongs directly connected to two energized SMA wires.

↔ Resultant guest surface motion is orthogonal to the row of energized SMA wires.

The two empty cells ($A_1 - B_1 - A_2$, and $A_3 - B_3 - B_2$) are not highlighted for clarity

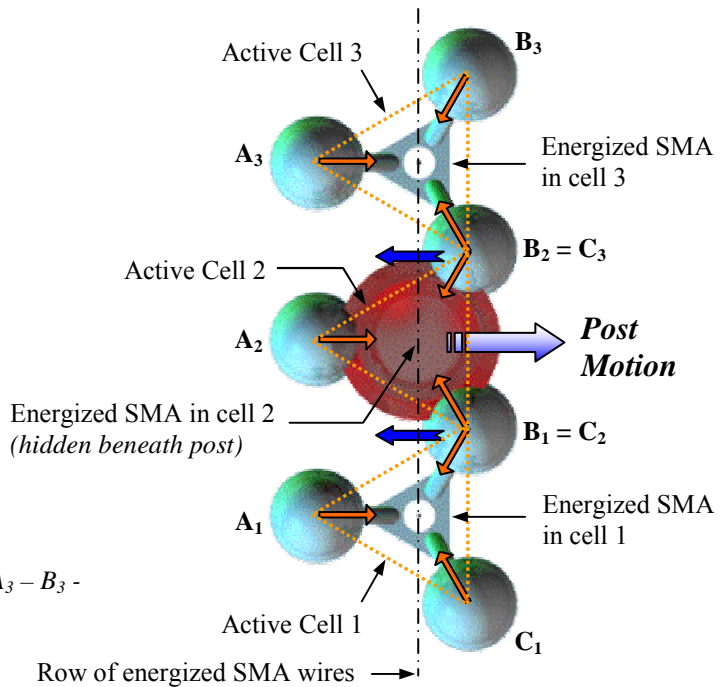


Figure 2.9: Local Prong Operation: Gait 2. If a post is located in an active cell directly above a SMA wire, it can be translated to the right of the figure by energizing a vertical row of three adjacent SMA wires. In this case, the three prongs on the left side of the figure (prongs A_1 , A_2 , A_3) all deflect towards the right with prong A_2 pushing directly on the post. Prongs C_1 and B_3 both deflect towards their respective attached and energized SMA wires. Prongs B_1 and B_2 are each acted upon by multiple SMA wires and therefore their motion is given by the resultant force vector created by the energized wires (towards the left side of the figure). As a result of the individual prong motions, prong A_2 pushes the post between prongs B_1 and B_2 to complete the translation of one step.

2.2.2.3.1 Rotation Generation

While guest positioning requires only a single post, orientation control requires at least two. By altering the timing and directions of positioning forces applied to each guest surface post, rotation can be achieved. The hexagonal host surface pattern employed by Active Velcro does impose one significant limitation on guest rotations. While 360° of rotation are possible it can not be accomplished purely, that is translation must be mixed in with rotations. More specifically, at most 60° of pure rotation are possible before requiring a translation of the guest centroid. This limitation is a product of the 60° anti-symmetry of the Active Velcro host surface. After 60° of CCW rotation a prong will necessarily impede continued rotation. At this point, a translation in any of the three available directions (right, up-left, down-left) will eliminate the interference and continued CCW rotation is possible. The anti-symmetry is the product of arraying a hexagonal repeat unit (which would lead to 60° symmetry) but only placing prongs on every other corner of the hexagon (resulting in 120° symmetry and 60° anti-symmetry).

2.2.2.3.2 *Increased Positioning Speed*

With multiple posts, increased speed may be possible since sequential steps can be achieved without requiring any SMA wire to cool prior to the next step. This is accomplished by energizing only enough SMA wires to directly push a subset of the total engaged posts forward. Because all posts are rigidly connected together, the remaining posts are pushed (or pulled) along into the next cell even though their respective cells were not energized. Motion can continue immediately by heating a different subset of cooled SMA wires; thereby eliminating the slow cooling response of the SMA wires from the sequence. Operation in this **phased activation** manner allows an SMA wire to cool for several steps while other SMA wires are performing the motion. Speed is now only a function of the heating response time of the SMA wires, which increases the potential speeds by approximately an order of magnitude (depending on the SMA characteristics) when compared to situations requiring complete SMA cooling between steps. For example, according to the wire manufacturer, Dynalloy, and experimental confirmation by the author, a 15 mil (0.38 mm) diameter SMA wire heats in less than 1 second under the application of 2.75 A at room temperature. Conversely, the same wire requires approximately 9 seconds to cool down, thus the cycle time under room temperature conditions without forced airflow is approximately 10 seconds. Remove the cooling time from the equation and effective cycle times may be reduced to the heating time, or less than 1 second. In fact, the heating time of the wire can be very quick as long as the power is present. Research independent of this project has confirmed 15 mil wire responses of a few milliseconds. However, for this research the manufacturer recommended currents were applied which are conservative.

2.2.2.3.3 *Increased Reliability*

Because of the distributed actuation along the surface, reliability can be increased through a number of means. First, there are generally many paths between two locations on the host surface enabling the circumvention of localized damage. This property exists for both single and multi-post guests with Active Velcro. However, the phased activation approach can be exploited to pass the guest directly through certain types of damaged regions or to continue operation even in the event of power reductions. For example, if a four post guest can be manipulated in the phased activation method by only pushing on two posts at a time, the power consumption is cut in half. More importantly, the positioning occurs without the need for functional actuators on the dragged posts. Thus a guest can be manipulated through regions which have lost actuator control because of fatigue, power loss, control system failure, or other damage as long as the pathways for motion have not been impaired. This robustness gained by the redundancy in the system is unique to this type of actuation system and very useful for critical applications such as space applications where maintenance of the surface would not be possible.

2.3. OPERATIONAL MODELS AND VALIDATION

Active Velcro is a general technology which can be applied to different applications by tailoring a multitude of geometric and material design variables. This design freedom necessitates accurate models capable of predicting the operational characteristics (engagement/retention/positioning force, load carrying capability, and stress levels) to guide the

engineer. This section presents the development of designs tools in the form of analytical behavioral models. Analytical models were chosen over alternative approaches such as Finite Element Analysis (FEA) due to their flexibility. With over 13 dimensions required to fully define the host and guest surfaces, a large battery of FEA models would be required to capture the impact of each variable dimension on the engagement, retention, and positioning behaviors. In contrast, an analytical model is applicable for innumerable combinations of host and guest surface geometries.

Building upon the well established Matrix Displacement approach outlined by Pestel and Leckie in 1963, analytical models capturing the force-deflection behavior of a single-cell Active Velcro host surface under generalized loading conditions were derived. The resulting single-cell stiffness matrix representation was expanded to capture the response of any number of linked prong cells by exploiting the hexagonal symmetry of the host surface. This procedure is demonstrated for a three-cell host surface, the simplest surface capable of positioning a guest. Loading conditions specific to engagement, retention, and position including the presence of sliding friction at all interfaces were applied to capture the three primary behaviors of the Active Velcro technology. The validity of the models was experimentally verified under three common operating scenarios: free deflection, surface positioning and guest surface engagement/retention.

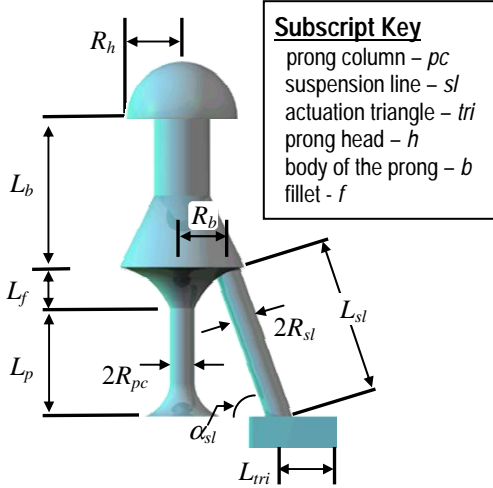
2.3.1. General Model Structure

Key to capturing the general quasi-static behavior (engagement, retention, positioning) for the entire host surface is an understanding of how the prongs and actuation triangle within an individual cell move under applied loads. An individual cell was modeled with two types of elements: 1) flexible elements (prong column and suspension line) denoted by subscript i , that store strain energy and 2) rigid elements (actuation triangle and all other elements within the prong) that provide connectivity for the transmission of forces and displacements. The geometric terminology for the prongs and the actuation triangle elements is shown in Figure 2.10a. The guest surface consists only of rigid identical posts. Three parameters are required to define the pertinent dimensions of each post, the radius of the support column, R_{po-sc} , the half-angle of the conical connection topology, χ , and the outermost radius of the connection topology, R_{po} (Figure 2.10b).

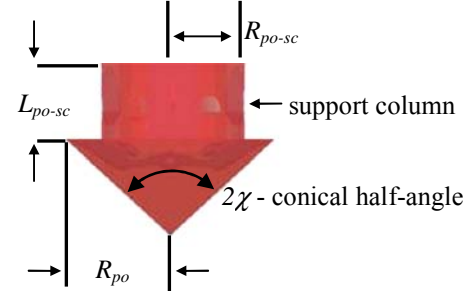
The host surface was modeled with a system stiffness matrix, \mathbf{K}_{net} , that relates the vector of externally applied loads, \mathbf{F} , to the global displacements, \mathbf{D} ,

$$\{\mathbf{F}_1 \ \dots \ \mathbf{F}_j \ \dots \ \mathbf{F}_s\}^T = \mathbf{K}_{net} \{\mathbf{D}_1 \ \dots \ \mathbf{D}_j \ \dots \ \mathbf{D}_s\}^T. \quad (2.3)$$

Generally the prongs and actuation triangles are able to move with six degrees of freedom, thus \mathbf{F}_j and \mathbf{D}_j are actually 6x1 vectors (Figure 2.11). As prongs are added to the host surface, the size of the stiffness matrix will increase to $6*s \times 6*s$ where s is the total number of actuation triangles and prongs. Because of the numerous host surface cell interactions, \mathbf{K}_{net} is not easily obtained directly. However, it can be obtained indirectly using the Matrix Displacement approach as outlined by Pestel and Leckie by defining \mathbf{K}_{net} in terms of two matrices, the unassembled stiffness matrix, \mathbf{K}_u and the compatibility matrix, $\mathbf{\epsilon}$,



a) Host Surface



b) Guest Post

Figure 2.10: Variable Dimensional Parameters. a) Ten parameters are required to fully define the host surface geometry. For the modeling effort, only the prong column and suspension line were considered flexible elements (geometry denoted by the subscripts *pc* and *sl* respectively). b) Four parameters are required to define each guest surface post.

$$\mathbf{K}_{net} = \boldsymbol{\epsilon}^T \mathbf{K}_u \boldsymbol{\epsilon}. \quad (2.4)$$

The role of the compatibility matrix is to ensure that the local deformations of all the flexible elements throughout the mechanism, \boldsymbol{v} , are consistent with the applied global displacements, \mathbf{D} , ensuring system integrity under load (Figure 2.11)

$$\boldsymbol{v} = \boldsymbol{\epsilon} \mathbf{D}. \quad (2.5)$$

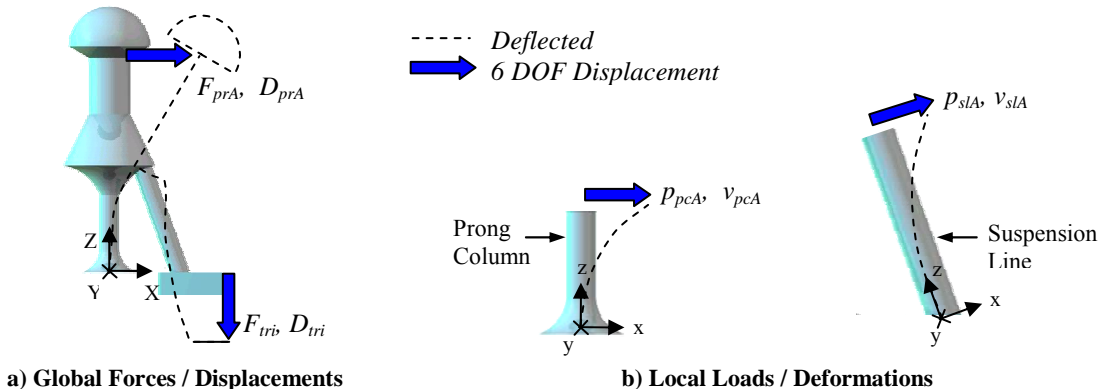


Figure 2.11: Global Displacements vs. Local Deformations. (only one prong shown for clarity) a) The model permits the application of globally defined forces and displacements at the actuation triangles (\mathbf{F}_{trb} , \mathbf{D}_{trb}) and the center of each prong head ($\mathbf{F}_{prA,B,C}$, $\mathbf{D}_{prA,B,C}$). b) The compatibility equations convert these globally defined forces and displacements into the locally defined loads and deformations at the flexible prong columns and suspension lines ($\mathbf{p}_{pcA,B,C}$, $\mathbf{v}_{pcA,B,C}$, $\mathbf{p}_{slA,B,C}$, $\mathbf{v}_{slA,B,C}$).

The transpose of the compatibility matrix relates the externally applied forces, \mathbf{F} , to the locally defined elemental loads, \mathbf{p} , using equilibrium constraints

$$\mathbf{F} = \boldsymbol{\epsilon}^T \mathbf{p} . \quad (2.6)$$

Thus the compatibility matrix, $\boldsymbol{\epsilon}$, contains all the connectivity information for the entire host surface. The unassembled stiffness matrix, \mathbf{K}_u , contains only the locally defined force-deflection relationships for the flexible elements comprising the surface. By isolating the force-deflection information from the connectivity information, the net system stiffness matrix, \mathbf{K}_{net} , can be readily computed regardless of surface complexity.

2.3.1.1. Unassembled Stiffness Matrix

The unassembled stiffness matrix, \mathbf{K}_u , is a simple block diagonal matrix of the general form

$$\mathbf{p} = \begin{Bmatrix} \mathbf{p}_1 \\ \mathbf{p}_2 \\ \vdots \\ \mathbf{p}_i \\ \vdots \\ \mathbf{p}_n \end{Bmatrix} = \begin{bmatrix} [\mathbf{K}_1] & & & & & \\ & [\mathbf{K}_2] & & & & \\ & & \ddots & & & \\ & & & \mathbf{0} & & \\ & & & & [\mathbf{K}_i] & \\ & & & & & \ddots \\ & & & & & & [\mathbf{K}_n] \end{bmatrix} \begin{Bmatrix} \mathbf{v}_1 \\ \mathbf{v}_2 \\ \vdots \\ \mathbf{v}_i \\ \vdots \\ \mathbf{v}_n \end{Bmatrix} = \mathbf{K}_u \mathbf{v} , \quad (2.7)$$

where \mathbf{p} is a vector of locally defined load vectors applied to all n flexible elements (prong columns and suspension lines) of the structure and \mathbf{v} is a vector of the locally defined displacement vectors of all n flexible elements. Note that \mathbf{K}_u is a block diagonal matrix and thus represents only a collection of unassembled element stiffness matrices \mathbf{K}_i . The unassembled elemental stiffness matrix, \mathbf{K}_i , was derived for each flexible element using classical beam and bar theory for a generalized cantilevered beam assuming that the locally defined loads \mathbf{p}_i (shears - V_x , V_y , tip moments - M_y , M_x , axial load - N_z , and axial torque - T_z) act independently and can be decoupled. These loads are related to the locally defined deformations \mathbf{v}_i (transverse deformations - w_x , w_y , tip rotations - ψ_y , ψ_x , axial deformation - μ_z , and twist - ϕ_z ,) through the elemental stiffness matrix \mathbf{K}_i

$$\mathbf{p}_i = \begin{Bmatrix} N_z \\ T_z \\ V_x \\ M_y \\ V_y \\ M_x \end{Bmatrix} = \begin{bmatrix} \frac{E\Lambda}{L} & 0 & 0 & 0 & 0 & 0 \\ 0 & \frac{GJ}{L} & 0 & 0 & 0 & 0 \\ 0 & 0 & \frac{12EI}{L^3} & \frac{-6EI}{L^2} & 0 & 0 \\ 0 & 0 & \frac{-6EI}{L^2} & \frac{4EI}{L} & 0 & 0 \\ 0 & 0 & 0 & 0 & \frac{12EI}{L^3} & \frac{6EI}{L^2} \\ 0 & 0 & 0 & 0 & \frac{6EI}{L^2} & \frac{4EI}{L} \end{bmatrix} \begin{Bmatrix} u_z \\ \phi_z \\ w_x \\ \psi_y \\ w_y \\ \psi_x \end{Bmatrix} = \mathbf{K}_i \mathbf{v}_i , \quad (2.8)$$

composed of geometry (L - length of the element, Λ - cross sectional area, I - area moment of inertia, and J - polar moment of inertia) and material parameters (E - Young's modulus, G -

shear modulus). Since the boundary conditions and material for the prong columns and suspension lines are identical, their elemental stiffness matrices differ only in the geometric parameters.

2.3.1.2. Compatibility Matrix

The compatibility matrix, ϵ , holds all the connection information and thus is dependent on the specific formation of elements comprising the structure. It will be different depending on how many cells are considered. The form of the single-cell compatibility matrix is presented here; however, the symmetry in the structure allows this solution to be expanded easily to capture the behavior of any number of cells.

For each cell under general loading conditions, \mathbf{F} , a 36×24 compatibility matrix, ϵ , is necessary to fully define the relationship between the global displacements, \mathbf{D} , at the tip of each prong and actuation triangle and the local element deformations, \mathbf{v} , within each prong column and suspension line

$$\mathbf{v} = \begin{bmatrix} \mathbf{v}_{slA} \\ \mathbf{v}_{pcA} \\ \mathbf{v}_{slB} \\ \mathbf{v}_{pcB} \\ \mathbf{v}_{slC} \\ \mathbf{v}_{pcC} \end{bmatrix} = \begin{bmatrix} [\epsilon_{slA, tri}] & [\epsilon_{slA, prA}] & 0 & 0 \\ 0 & [\epsilon_{pcA, prA}] & 0 & 0 \\ [\epsilon_{slB, tri}] & 0 & [\epsilon_{slB, prB}] & 0 \\ 0 & 0 & [\epsilon_{pcB, prB}] & 0 \\ [\epsilon_{slC, tri}] & 0 & 0 & [\epsilon_{slC, prC}] \\ 0 & 0 & 0 & [\epsilon_{pcC, prC}] \end{bmatrix} \begin{bmatrix} \mathbf{D}_{tri} \\ \mathbf{D}_{prA} \\ \mathbf{D}_{prB} \\ \mathbf{D}_{prC} \end{bmatrix} = \epsilon \mathbf{D} \quad (2.9)$$

where $\epsilon_{i,j}$ refers to the 6×6 compatibility sub-matrix for “ i^{th} flexible element” with respect to globally defined displacements of the “ j^{th} location”.

These sub-matrices are derived by enforcing a virtual displacement of a single degree of freedom within the displacement vector, \mathbf{D} , while holding all other displacements fixed at zero and examining the resulting locally defined deformation of the flexible elements, \mathbf{v} . This process is greatly simplified by the purely local effects of the virtual displacement theorem which allows for the rapid recognition of empty compatibility sub-matrices since it is generally obvious which flexible elements are rigidly tied to each global degree of freedom. For example, if the chosen virtual displacement is within the \mathbf{D}_{prA} vector, no deformations of prong columns B and C or suspension lines B and C are generated resulting in the 4 empty sub-matrices in the second column of ϵ .

In general, ϵ is of size $6*n \times 6*s$ where n is the number of flexible elements (prong columns, suspension lines) in the structure, s is the number of prongs and actuation triangles, and assuming six displacements are required to define the positions of each prong and each actuation triangle. However, ϵ can be reduced in size if symmetric loading conditions are enforced, as will be shown for the specific models of engagement and retention behavior.

2.3.2. Engagement Model

Active Velcro is unique in that the engagement requires an intertwinement of the host and guest surfaces not required by existing distributed manipulation surfaces. Without a successful engagement, manipulation can not occur and in the worst case the guest may be lost. Thus a model which aids the designer in selecting host and guest surface geometries which achieve the desired engagement characteristics (maximum engagement force, depth at which engagement occurs, shape of the engagement force-deflection curve) is required. The engagement behavior is modeled for a single-post guest surface entering a single-cell host surface as depicted in Figure 2.12. By modeling a single-cell, a closed form expression incorporating the host and guest surface geometric variables could be obtained. To estimate the net engagement force for an entire guest surface, the results of the single-cell model are multiplied by the number of guest surface posts.

For this model, the engaging post is assumed to enter the cell vertically and centered, distributing any loads evenly amongst the three prongs of the cell. By coupling the assumption of a centered post with the axi-symmetric prong cell the number of degrees of freedom of the mechanism can be reduced to 4 by only considering the actuation triangle and a single prong

$$\mathbf{F}^{\text{sym}} = \begin{Bmatrix} F_{prA_z} \\ F_{prA_x} \\ M_{prA_y} \\ F_{tri_z} \end{Bmatrix} = \left[(\boldsymbol{\epsilon}^{\text{sym}})^T \mathbf{K}_u^{\text{sym}} \boldsymbol{\epsilon}^{\text{sym}} \right] \begin{Bmatrix} \Delta_{prA_z} \\ \Delta_{prA_x} \\ \Psi_{prA_y} \\ \Delta_{tri_z} \end{Bmatrix} = \mathbf{K}_{\text{net}}^{\text{sym}} \mathbf{D}^{\text{sym}}. \quad (2.10)$$

Since only loads and deformations in the XZ plane are now required, the unassembled stiffness matrix (Equation 2.8) and compatibility matrix (Equation 2.9) are simplified considerably to $\mathbf{K}_u^{\text{sym}}$ and $\boldsymbol{\epsilon}^{\text{sym}}$

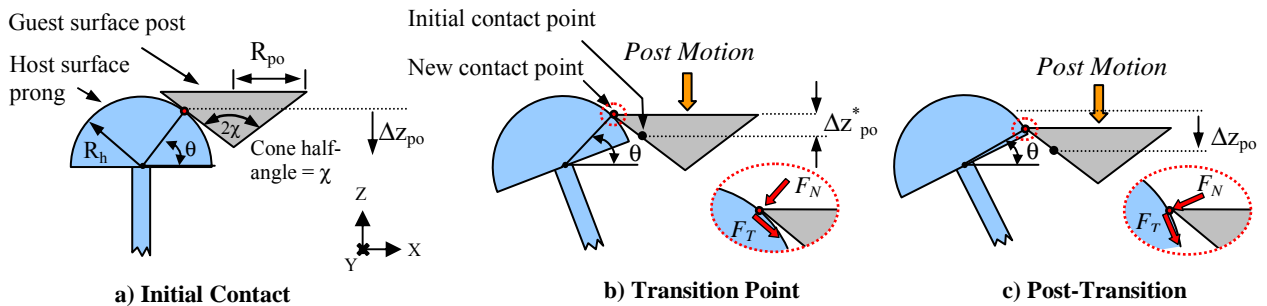


Figure 2.12: Engagement Phases. (only one prong shown for clarity) **a)** The location of the initial contact point is a function of the post shape, prong shape, and the diameter of the prong head. At this point the frictional loads are tangent to both the post and prong lead surfaces and remain tangent until the transition point is reached. **b)** A transition in the engagement behavior occurs when the maximum radius of the guest surface post, R_{po} , becomes the contact point between the post and prong. **c)** After the incoming post passes the transition point, the posts and prongs are no longer tangent to each other and thus frictional loads are no longer tangent to the post. Engagement behavior is no longer defined by the shape of the post's lead surface but rather the shape of the prong's lead surface.

$$\mathbf{p}_u^{\text{sym}} = \begin{bmatrix} N_{sl} \\ V_{sl_x} \\ M_{sl_y} \\ N_{pc} \\ V_{pc_x} \\ M_{pc_y} \end{bmatrix} = \begin{bmatrix} \frac{EA_{sl}}{L_{sl}} & 0 & 0 & 0 & 0 & 0 \\ 0 & \frac{12EI_{sl}}{L_{sl}^3} & \frac{-6EI_{sl}}{L_{sl}^2} & 0 & 0 & 0 \\ 0 & \frac{-6EI_{sl}}{L_{sl}^2} & \frac{4EI_{sl}}{L_{sl}} & 0 & 0 & 0 \\ 0 & 0 & 0 & \frac{EA_{pc}}{L_{pc}} & 0 & 0 \\ 0 & 0 & 0 & 0 & \frac{12EI_{pc}}{L_{pc}^3} & \frac{-6EI_{pc}}{L_{pc}^2} \\ 0 & 0 & 0 & 0 & \frac{-6EI_{pc}}{L_{pc}^2} & \frac{4EI_{pc}}{L_{pc}} \end{bmatrix} \begin{bmatrix} u_{zsl} \\ w_{xsl} \\ \psi_{ysl} \\ u_{zpc} \\ w_{xpc} \\ \psi_{ypc} \end{bmatrix} = \begin{bmatrix} a_{sl} & 0 & 0 & 0 & 0 & 0 \\ 0 & c_{sl} & d_{sl} & 0 & 0 & 0 \\ 0 & d_{sl} & e_{sl} & 0 & 0 & 0 \\ 0 & 0 & 0 & a_{pc} & 0 & 0 \\ 0 & 0 & 0 & 0 & c_{pc} & d_{pc} \\ 0 & 0 & 0 & 0 & d_{pc} & e_{pc} \end{bmatrix} \begin{bmatrix} u_{zsl} \\ w_{xsl} \\ \psi_{ysl} \\ u_{zpc} \\ w_{xpc} \\ \psi_{ypc} \end{bmatrix} = \mathbf{K}_u^{\text{sym}} \mathbf{v}_u^{\text{sym}} \quad (2.11)$$

$$\boldsymbol{\epsilon}^{\text{sym}} = \begin{bmatrix} 1 & 0 & 0 & 0 \\ 0 & 1 & -L_f - L_b & 0 \\ 0 & 0 & 1 & 0 \\ \sin(\alpha) & -\cos(\alpha) & L_b \cos(\alpha) - R_b \sin(\alpha) & -\sin(\alpha) \\ \cos(\alpha) & \sin(\alpha) & -R_b \cos(\alpha) - L_b \sin(\alpha) & -\cos(\alpha) \\ 0 & 0 & 1 & 0 \end{bmatrix}. \quad (2.12)$$

Note that each term of the unassembled symmetric stiffness matrix, $\mathbf{K}_u^{\text{sym}}$, in Equation 2.11 was redefined with shorthand, a_{sl} , c_{sl} , d_{sl} , a_{pc} , c_{pc} , and d_{pc} . This was done only to reduce the printed size of the final engagement, retention, and positioning equations for improved readability.

The shapes of the post and prong lead surfaces result in two distinct stages of the engagement process. In the first stage, the conical lead surface of the post slides along the hemispherical lead surface of the prong and the surfaces remain mutually tangent to each other. Transition occurs when the outer radius of the post, R_{po} , is reached. Beyond this point, the surfaces are no longer mutually tangent. Since the contact point on the post remains fixed at the maximum diameter after the transition, the engagement behavior switches from being defined by the shape of the *post*'s lead surface to the shape of the *prong*'s lead surface.

2.3.2.1. Loading Conditions

During engagement it is assumed that the SMA is not activated and the actuation triangle vertical force, F_{triz} , is zero. Engagement should occur at as low a force as possible to maximize the chances of a successful mating between the guest and host surfaces. Thus the SMA wires should not be energized since doing so closes the cells inhibiting engagement. For the purposes of this model it was assumed that the force on the actuation in the vertical direction, F_{triz} , is zero however a more complex approach including the stiffness of the unenergized SMA wire can be examined if more accurate results are required. The other external loads, F_{prAx} , F_{prAz} , and moment, M_{prAy} , are applied to the prong as a result of both the normal, F_N , and tangential, F_T , loads applied by the engaging post. To achieve a closed form solution, coulomb friction was assumed ($F_T = \mu_E F_N$) resulting in the following globally defined loads applied to the prong,

$$\mathbf{F}_{prA} = \begin{Bmatrix} F_{prA_z} \\ F_{prA_x} \\ M_{prA_y} \end{Bmatrix} = \begin{Bmatrix} F_N[-\sin(\theta) - \mu_E \cos(\theta)] \\ F_{prA_z} \frac{[-\cos(\theta) + \mu_E \sin(\theta)]}{[-\sin(\theta) - \mu_E \cos(\theta)]} \\ F_{prA_z} \frac{\mu_E R_h}{[-\sin(\theta) - \mu_E \cos(\theta)]} \end{Bmatrix}, \quad (2.13)$$

where R_h is the prong head radius, θ is the contact angle measured from the horizontal plane to the contact point, and μ_E is the coefficient of friction between the post and prong lead surfaces. Thus the load vector, \mathbf{F} , can be reduced to a single unknown, F_{prA_z} , leaving five unknowns (F_{prA_z} , Δ_{prA_z} , Δ_{prA_x} , Δ_{prA_y} , Δ_{triz}) with four equations captured by Equation 2.10

The horizontal prong displacement, Δ_{prA_x} , can be related to the vertical distance traveled by the engaging post relative to the initial contact point, Δz_{po} . Since the conical post and hemispherical prong remain mutually tangent up to the transition point of Figure 2.12b, the contact angle, θ , is defined solely by the post's conical half angle. After the transition point has been passed, the contact angle is a function of the current post position, Δz_{po} , relative to its position at the transition point, Δz_{po}^*

$$\theta = \begin{cases} \chi & 0 > \Delta z_{po} > \Delta z_{po}^* \\ \sin^{-1} \left(\frac{\Delta z_{po} - \Delta z_{po}^* + R_h \sin(\chi)}{R_h} \right), & \Delta z_{po} < \Delta z_{po}^* \end{cases} \quad (2.14)$$

where

$$\Delta z_{po}^* = \frac{-R_{po} + R_{cell} - R_h \cos(\chi)}{\tan(\chi)}. \quad (2.15)$$

Because the post has an idealized conical shape, the horizontal prong displacement for prong A, Δ_{prA_x} , is a simple function of the vertical post displacement, Δz_{po} . Just as with the expression for the contact angle, the expression defining how the prongs are deflected in response to an incoming post is also distinct over two ranges: from initial contact up to the transition point and from the transition point until engagement is completed

$$\Delta_{prA_x} = \begin{cases} \Delta z_{po} \tan(\chi) & 0 > \Delta z_{po} > \Delta z_{po}^* \\ -R_h \cos(\theta) + [R_{cell} - R_{po}], & \Delta z_{po} < \Delta z_{po}^* \end{cases}. \quad (2.16)$$

2.3.2.2. Final Engagement Model

By substituting in Equation 2.16 for Δ_{prA_x} , the global Equation 2.10 can be solved for the engagement force, F_E , as a function of the post displacement, Δz_{po}

$$F_E = 3F_{prA_z} = \begin{cases} \Delta z_{po} \tan(\chi) \frac{N_E}{D_E}, & 0 > \Delta z_{po} > \Delta z_{po}^* \\ (R_{cell} - R_{po} - R_h \cos(\theta)) \frac{N_E}{D_E}, & \Delta z_{po} < \Delta z_{po}^* \end{cases}, \quad (2.17)$$

where $N_E = 3 \begin{bmatrix} -c_{sl}d_{pc}^2 + c_{pc} \left\{ -d_{sl}^2 + c_{sl}(e_{sl} + e_{pc}) \right\} + \\ a_{sl} \left\{ -2d_{sl}^2 - d_{pc}^2 + (2c_{sl} + c_{pc})(e_{sl} + e_{pc}) - 4c_{sl}d_{pc}L_f + 2c_{sl}c_{pc}L_f^2 \right\} \\ -\cos(2\alpha) \left[(-a_{sl} + c_{sl})d_{pc}^2 + c_{pc} \left\{ d_{sl}^2 + (a_{sl} - c_{sl})(e_{sl} + e_{pc}) \right\} \right] \\ -4a_{sl}d_{sl}(d_{pc} - c_{pc}L_f)\sin(\alpha) \end{bmatrix}, \text{ and} \quad (2.18)$

$$D_E = \frac{F_x}{F_z} * \begin{bmatrix} d_{sl}^2 - (a_{sl} + c_{sl})(e_{sl} + e_{pc} - 2d_{pc}L_f + c_{pc}L_f^2) + \\ L_b \left\{ 2(a_{sl} + c_{sl})(d_{pc} - c_{pc}L_f) \right\} \\ -L_b^2 \left\{ 2a_{sl}c_{sl} + (a_{sl} + c_{sl})c_{pc} \right\} \end{bmatrix} + \\ \frac{M_y}{F_z} \left[(a_{sl} + c_{sl})(d_{pc} - c_{pc}L_f) - L_b \left\{ 2a_{sl}c_{sl} + (a_{sl} + c_{sl})c_{pc} \right\} \right] + \\ 2a_{sl}d_{sl} \left(2 \frac{F_x}{F_z} L_b + \frac{M_y}{F_z} \right) \sin(\alpha) + \cos(2\alpha) * \\ \begin{bmatrix} d_{sl}^2 \frac{F_x}{F_z} + (a_{sl} - c_{sl}) * \\ \left\{ \frac{F_x}{F_z} \left\{ e_{sl} + e_{pc} + (L_f + L_b) \left\{ -2d_{pc} + c_{pc}(L_f + L_b) \right\} \right\} \right\} + \\ \left\{ \frac{M_y}{F_z} \left\{ -d_{pc} + c_{pc}(L_f + L_b) \right\} \right\} \end{bmatrix} \quad (2.19)$$

Although Equation 2.17 appears rather complicated at first glance, the majority of the terms are simply dimensions of the mechanism. Only the load ratios, F_{prA_x}/F_{prA_z} and M_{prA_y}/F_{prA_z} vary throughout the engagement process as the contact angle changes according to Equation 2.14. Up to the transition point, Δz_{po}^* , the engagement force, F_E , increases linearly with post displacement, Δz_{po} . At this point the contact angle begins to decrease altering the direction of the normal and frictional applied loads. This results in a nonlinear decreasing relationship between the engagement force and further post displacement. Since the contact angle initially equals the conical half-angle of the post (a positive number) and decreases continuously approaching zero, the engagement force will be continuous with post displacement reaching a maximum shortly after transition occurs.

2.3.3. Retention Model

Once the guest surface engages the host surface it is retained by the trailing surfaces of the post and prong. The initial contact location, $R_{contact_i}$, on the prong is defined as the difference between the radius of the cell, R_{cell} , and the maximum radius of the post connection topology, R_{po} . As the post begins to separate from the prong cell, the tip of the post (R_{po})

translates along the trailing surface of the prong, causing the prong to deflect outward with a horizontal displacement, Δ_{prA_x} , as in Figure 2.13. Release of the post from the prong cell is achieved when the post tip reaches the outer radius of the prong, R_h or

$$-\Delta_{prA_x}^* = R_h - R_{contact_i} \quad (2.20)$$

2.3.3.1. Loading Conditions

The net stiffness matrix and compatibility matrix for retention are the same as for engagement (Equations 2.11 and 2.12) but naturally the loads applied to the prongs are different. The loads are transferred from the retreating post equally to the prongs through both the normal force, F_N , and the coulomb friction force $F_T = \mu_R F_N$

$$F_{prA} = \begin{bmatrix} F_{prA_z} \\ F_{prA_x} \\ M_{prA_y} \end{bmatrix} = \begin{bmatrix} F_N [\cos(\theta) + \mu_R \sin(\theta)] \\ F_{prA_z} \frac{[-\sin(\theta) + \mu_R \cos(\theta)]}{[\cos(\theta) + \mu_R \sin(\theta)]} \\ F_{prA_z} \frac{-R_{contact_i}}{[\cos(\theta) + \mu_R \sin(\theta)]} \end{bmatrix} \quad (2.21)$$

2.3.3.2. Final Retention Model

The contact angle, θ , is measured from the horizontal plane to the contact point and equal to the negative of the deflected prong angle, ψ_{prA_y} , which varies through the retention cycle. Similar to engagement, this reduces the global system of equations (Equation 2.10) leaving five unknowns (F_{prA_z} , Δ_{prA_z} , Δ_{prA_x} , Δ_{prA_y} , Δ_{triz}). This can be solved to cast the retention force as a function of ψ_{prA_y}

$$F_R = \psi_{prA_y} \frac{N_R}{D_R}, \quad (2.22)$$

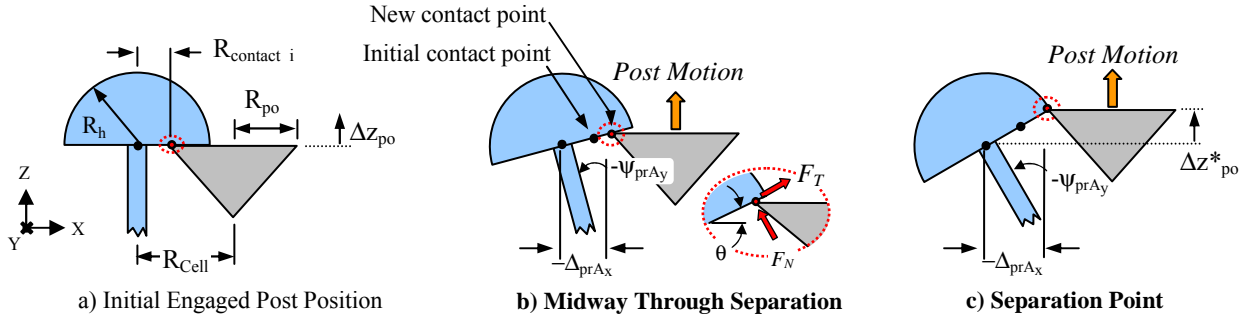


Figure 2.13: Retention. (only one prong shown for clarity) **a)** Initially the trailing surfaces of the post and prongs are parallel. The initial contact point, $R_{contact_i}$ is determined by the radius of the post, R_{po} , and the radius of the cell, R_{cell} . **b)** As the post retreats, the contact point slides towards the edge of the prong connection topology. **c)** Separation occurs when the post clears the prong.

$$\text{where, } N_R = 3 \begin{bmatrix} c_{sl}d_{pc}^2 + c_{pc}\{d_{sl}^2 - c_{sl}(e_{sl} + e_{pc})\} + \\ a_{sl}\{2d_{sl}^2 + d_{pc}^2 - (2c_{sl} + c_{pc})(e_{sl} + e_{pc}) + 4c_{sl}d_{pc}L_f - 2c_{sl}c_{pc}L_f^2\} + \\ \cos(2\alpha)\left[(-a_{sl} + c_{sl})d_{pc}^2 + c_{pc}\{d_{sl}^2 + (a_{sl} - c_{sl})(e_{sl} + e_{pc})\}\right] + \\ 4a_{sl}d_{sl}(d_{pc} - c_{pc}L_f)\sin(\alpha) \end{bmatrix}, \quad (2.23)$$

$$\begin{aligned} D_R = & \frac{F_x}{F_z} \left[(a_{sl} + c_{sl})(d_{pc} - c_{pc}L_f) - L_b \{2a_{sl}c_{sl} + c_{pc}(a_{sl} + c_{sl})\} \right] - \\ & \frac{M_y}{F_z} \left[2a_{sl}c_{sl} + (a_{sl} + c_{sl})c_{pc} \right] - \\ & \cos(\alpha) \left[(a_{sl} - c_{sl}) \left\{ d_{pc} \frac{F_x}{F_z} - c_{pc} \frac{F_x}{F_z} (L_f + L_b) + \frac{M_y}{F_z} \right\} \right] + \\ & \frac{F_x}{F_z} [2a_{sl}d_{sl} \sin(\alpha)] \end{aligned}, \quad (2.24)$$

where $\psi_{prA_y}^*$ is the angular rotation of prong A at the point of guest surface separation occurring at $\Delta_{prA_x}^*$ given in Equation 2.20 and is bounded by

$$0 \leq \psi_{prA_y} \leq \psi_{prA_y}^*. \quad (2.25)$$

Typically the angular displacement, ψ_{prA_y} , is not of significant interest; rather it is more desirable to relate the retention force, F_R , to the displacement of the post, Δz_{po} . Applying the small angle approximation for the angular prong rotation ψ_{prA_y} , the vertical post displacement Δz_{po} can be defined in terms of the initial contact radius, $R_{contact_i}$, the horizontal prong displacement, Δ_{prA_x} , and ψ_{prA_y}

$$\Delta z_{po} = -(R_{contact_i} - \Delta_{prA_x})\psi_{prA_y}. \quad (2.26)$$

Following the solution of Equation 2.10, Δ_{prA_x} , is known and Equation 2.26 can be solved.

The final retention model, Equation 2.22, is a smooth continuous function of the guest post displacement, Δz_{po} . Thus separation should occur with a smooth ramp up of force until the guest is released. Throughout the separation process, the contact point on the guest surface remains at the outermost radius of the post, R_{po} , and therefore it is the only guest surface parameter other than the friction coefficient, μ_R , to impact the retention behavior. First it determines how far the prongs must be deflected before separation occurs (Equation 2.20). Second it impacts the moments imparted on the prongs, M_{prA_y} , as the guest surface tries to separate from the host surface (Equation 2.21). Thus as the R_{po} increases the moments trying to deflect the prongs are reduced, increasing retention force, and the vertical post distance at transition is increased, further raising the retention force.

2.3.4. Multi-cell Positioning Model

Because the host surface is comprised of a repeated pattern of identical cells, it is straightforward to expand the single-cell model to a multi-cell model. Adding cells does not linearly increase the degrees of freedom for the surface because prongs are shared between adjacent cells. For example, a three-cell host surface (Figure 2.8) adds three displacement vectors for the new actuation triangle and two new prongs (\mathbf{D}_{tri_2} , \mathbf{D}_{prA_2} and \mathbf{D}_{prB_2}) instead of four because prong B_1 and C_2 are the same. Furthermore the three-cell surface is the simplest host surface capable of generating guest surface motion, thus representing a gait 1 translation (Figure 2.8). The three-cell positioning force model is presented in this section to demonstrate the ease of model expansion while providing further incite into the capabilities of Active Velcro mechanism.

Generally a new compatibility matrix, $\mathbf{\epsilon}$, must be derived for the three-cell host to convert the new displacements and those of the original single cell into the deformations of all the flexible elements in the surface, \mathbf{v}

$$\mathbf{v} = \begin{pmatrix} \mathbf{v}_{slA_1} \\ \mathbf{v}_{pcA_1} \\ \mathbf{v}_{slB_1} \\ \mathbf{v}_{pcB_1} \\ \mathbf{v}_{slC_1} \\ \mathbf{v}_{pcC_1} \\ \mathbf{v}_{slA_2} \\ \mathbf{v}_{pcA_2} \\ \mathbf{v}_{slB_2} \\ \mathbf{v}_{pcB_2} \\ \mathbf{v}_{slC_2} \end{pmatrix} = \begin{pmatrix} \begin{bmatrix} \mathbf{\epsilon}_{slA, tri} \end{bmatrix} & \begin{bmatrix} \mathbf{\epsilon}_{slA, prA} \end{bmatrix} & 0 & 0 & 0 & 0 & 0 \\ 0 & \begin{bmatrix} \mathbf{\epsilon}_{pcA, prA} \end{bmatrix} & 0 & 0 & 0 & 0 & 0 \\ \begin{bmatrix} \mathbf{\epsilon}_{slA, tri} \mathbf{R}_B \end{bmatrix} & 0 & \begin{bmatrix} \mathbf{\epsilon}_{slA, prA} \mathbf{R}_B \end{bmatrix} & 0 & 0 & 0 & 0 \\ 0 & 0 & \begin{bmatrix} \mathbf{\epsilon}_{pcA, prA} \mathbf{R}_B \end{bmatrix} & 0 & 0 & 0 & 0 \\ \begin{bmatrix} \mathbf{\epsilon}_{slA, tri} \mathbf{R}_C \end{bmatrix} & 0 & 0 & \begin{bmatrix} \mathbf{\epsilon}_{slA, prA} \mathbf{R}_C \end{bmatrix} & 0 & 0 & 0 \\ 0 & 0 & 0 & \begin{bmatrix} \mathbf{\epsilon}_{pcA, prA} \mathbf{R}_C \end{bmatrix} & 0 & 0 & 0 \\ 0 & 0 & 0 & 0 & \begin{bmatrix} \mathbf{\epsilon}_{slA, tri} \end{bmatrix} & \begin{bmatrix} \mathbf{\epsilon}_{slA, prA} \end{bmatrix} & 0 \\ 0 & 0 & 0 & 0 & 0 & \begin{bmatrix} \mathbf{\epsilon}_{pcA, prA} \end{bmatrix} & 0 \\ 0 & 0 & 0 & 0 & \begin{bmatrix} \mathbf{\epsilon}_{slA, tri} \mathbf{R}_B \end{bmatrix} & 0 & \begin{bmatrix} \mathbf{\epsilon}_{slA, prA} \mathbf{R}_B \end{bmatrix} \\ 0 & 0 & 0 & 0 & 0 & 0 & \begin{bmatrix} \mathbf{\epsilon}_{pcA, prA} \mathbf{R}_B \end{bmatrix} \\ 0 & 0 & \begin{bmatrix} \mathbf{\epsilon}_{slA, prA} \mathbf{R}_C \end{bmatrix} & 0 & \begin{bmatrix} \mathbf{\epsilon}_{slA, tri} \mathbf{R}_C \end{bmatrix} & 0 & 0 \end{pmatrix} = \mathbf{D}_{tri_1} \\ \mathbf{D}_{prA_1} \\ \mathbf{D}_{prB_1} \\ \mathbf{D}_{prC_1} \\ \mathbf{D}_{tri_2} \\ \mathbf{D}_{prA_2} \\ \mathbf{D}_{prB_2} \\ \mathbf{D}_{prC_2} = \mathbf{\epsilon} \mathbf{D} \quad (2.27)$$

The shaded portion of Equation 2.27 is exactly the compatibility matrix for the single-cell case (Equation 2.9), while the remainder of $\mathbf{\epsilon}$ contains sub-matrices for the new flexible prong columns and suspension lines. Application of the virtual displacement theory quickly identifies empty $\mathbf{\epsilon}_{ij}$ sub-matrices as it did in the single-cell model development. For example, displacing prong A_1 alone has no impact on the added prong columns and suspension lines thus all of the added sub-matrices in the second column of $\mathbf{\epsilon}$ are empty. However, displacing prong B_1 , will directly cause the deformation of suspension line C_2 (\mathbf{v}_{slC_2}) since it is shared; thereby necessitating the placement of the sub-matrix $\mathbf{\epsilon}_{slA, prA} \mathbf{R}_C$ into the third column of $\mathbf{\epsilon}$. Since all cells are identical, no new sub-matrices, $\mathbf{\epsilon}_{ij}$, need to be derived to complete $\mathbf{\epsilon}$.

In a similar manner, the unassembled stiffness matrix, \mathbf{K}_u , is expanded by including an additional \mathbf{K}_i sub-matrix (Equation 2.8) for each of the new flexible elements,

$$\mathbf{K}_u = \begin{bmatrix} \begin{bmatrix} \mathbf{K}_{sIA_1} \end{bmatrix} & \begin{bmatrix} \mathbf{K}_{pcA_1} \end{bmatrix} & & & & & & \\ & \begin{bmatrix} \mathbf{K}_{sIB_1} \end{bmatrix} & \begin{bmatrix} \mathbf{K}_{pcB_1} \end{bmatrix} & & & & & \\ & & \begin{bmatrix} \mathbf{K}_{sIC_1} \end{bmatrix} & \begin{bmatrix} \mathbf{K}_{pcC_1} \end{bmatrix} & & & & \\ & & & \begin{bmatrix} \mathbf{K}_{sIA_2} \end{bmatrix} & \begin{bmatrix} \mathbf{K}_{pcA_2} \end{bmatrix} & & & \\ & & & & \begin{bmatrix} \mathbf{K}_{sIB_2} \end{bmatrix} & \begin{bmatrix} \mathbf{K}_{pcB_2} \end{bmatrix} & & \\ & & & & & \begin{bmatrix} \mathbf{K}_{sIC_2} \end{bmatrix} & & \\ & & & & & & \begin{bmatrix} 0 \end{bmatrix} & \\ & & & & & & & 0 \end{bmatrix} \quad (2.28)$$

As with the compatibility matrix, this does not grow linearly since $K_{pcC_2} = K_{pcB_1}$. Likewise, every prong column is identical and every suspension line is identical; therefore K_u only has two unique sub-matrices, one for the prong column and one for the suspension line (Equation 2.8). Again the shaded portion of Equation 2.28 represents the unassembled stiffness matrix for a single-cell.

Combining the compatibility and unassembled stiffness matrices, yields the force-deflection relationship, in this case for a three-cell host surface,

$$\mathbf{F} = \begin{Bmatrix} \mathbf{F}_{tri_1} \\ \mathbf{F}_{prA_1} \\ \mathbf{F}_{prB_1} \\ \mathbf{F}_{prC_1} \\ \mathbf{F}_{tri_2} \\ \mathbf{F}_{prA_2} \\ \mathbf{F}_{prB_2} \end{Bmatrix} = \left[\boldsymbol{\epsilon}_2^T \mathbf{K}_u \boldsymbol{\epsilon}_2 \right] \begin{Bmatrix} \mathbf{D}_{tri_1} \\ \mathbf{D}_{prA_1} \\ \mathbf{D}_{prB_1} \\ \mathbf{D}_{prC_1} \\ \mathbf{D}_{tri_2} \\ \mathbf{D}_{prA_2} \\ \mathbf{D}_{prB_2} \end{Bmatrix} = \mathbf{K}_{net} \mathbf{D} . \quad (2.29)$$

However, during idealized three-cell positioning, the host surface behavior is symmetric about the guest surface post and the model can be simplified greatly reducing the degrees of freedom from 42 to 24 (Figure 2.14). Thus only a single-cell model and appropriately defined loading conditions are required to completely capture the response of the three-cell host surface positioning behavior. Accordingly, only the shaded portions of Equation 2.27 and 2.28 are used resulting in the reduced positioning model,

$$\mathbf{F}^{sym} \begin{Bmatrix} \mathbf{F}_{tri_1} \\ \mathbf{F}_{prA_1} \\ \mathbf{F}_{prB_1} \\ \mathbf{F}_{prC_1} \end{Bmatrix} = \left[\boldsymbol{\epsilon}^T \mathbf{K}_u \boldsymbol{\epsilon} \right] \begin{Bmatrix} \mathbf{D}_{tri_1} \\ \mathbf{D}_{prA_1} \\ \mathbf{D}_{prB_1} \\ \mathbf{D}_{prC_1} \end{Bmatrix} = \mathbf{K}_{net}^{sym} \mathbf{D}^{sym} \quad (2.30)$$

where K_u and ϵ are defined by Equations 2.8 and 2.9 respectively.

2.3.4.1. Loading Conditions

Frictional effects were considered at two locations during guest positioning (Figure 2.14). First, at the interface between the tops of the prongs and the guest surface base where frictional

forces are generated due to the load carried by the guest surface (μ_{Load}). In an environment with gravity this load is the net weight of the guest surface and its carrying load, W . Second, friction was considered at the interface between the outer radius of the prong connection topology and the post support column. Friction is generated here as the interfering prongs are deflected out of the way by a moving post (μ_{Int}). To generate motion, the two SMA wires are energized creating a vertical load on the actuation triangles, F_{SMA} , resulting in the following loads on prongs A₁, B₁, C₁, and the Actuation Triangle,

$$\mathbf{F} = \begin{Bmatrix} F_{prA_{1z}} \\ M_{prA_{1z}} \\ F_{prA_{1x}} \\ M_{prA_{1y}} \\ F_{prA_{1y}} \\ M_{prA_{1x}} \\ F_{prB_{1z}} \\ M_{prB_{1z}} \\ F_{prB_{1x}} \\ M_{prB_{1y}} \\ F_{prB_{1y}} \\ M_{prB_{1x}} \\ F_{prC_{1z}} \\ M_{prC_{1z}} \\ F_{Cx} \\ M_{prC_{1y}} \\ F_{prC_{1y}} \\ M_{prC_{1x}} \\ F_{tri_{1z}} \\ M_{tri_{1z}} \\ F_{tri_{1x}} \\ M_{tri_{1y}} \\ F_{tri_{1y}} \\ M_{tri_{1x}} \end{Bmatrix} = \begin{Bmatrix} -W/3 \\ F_{Ay} \frac{\mu_I R_h}{[-\sin(\theta) + \mu_{Int} \cos(\theta)]} + \mu_{Load} R_h \frac{W}{3} \left[1 - \frac{\cos(\theta)}{[-\sin(\theta) + \mu_{Int} \cos(\theta)]} \right] \\ F_{Ay} \frac{[-\cos(\theta) - \mu_{Int} \sin(\theta)]}{[-\sin(\theta) + \mu_{Int} \cos(\theta)]} - \mu_{Load} \frac{W}{3} \left[\frac{[-\cos(\theta) - \mu_{Int} \sin(\theta)]}{[-\sin(\theta) + \mu_{Int} \cos(\theta)]} \cos(\theta) + \sin(\theta) \right] \\ 0 \\ \text{unknown} \\ 0 \\ \left\{ \begin{array}{c} -W/3 \\ 0 \\ \text{unknown} \\ 0 \\ 0 \\ 0 \end{array} \right\} \\ \left\{ \begin{array}{c} 0 \\ 0 \\ 0 \\ 0 \\ 0 \\ 0 \end{array} \right\} \\ \left\{ \begin{array}{c} F_{SMA} \\ 0 \\ 0 \\ 0 \\ 0 \\ 0 \end{array} \right\} \end{Bmatrix} \quad (2.31)$$

where θ is the contact angle from the direction of post travel to the contact point on Prong A₁. The contact angle varies from an initial value of 60° before loads are applied to 90° at the transition point where the post begins to enter the next cell.

Since Prong A is constrained to follow the perimeter of the post support column as it is being manipulated, the X and Y displacement of Prong A₁ can be defined in terms of the X displacement of Prong B₁. Thus the X and Y positions of Prong A are defined by

$$\Delta_{prA_{1x}} = R_{Po-sc} [\sin(60^\circ) - \sin(\theta)] + \Delta_{prB_{1x}} \quad (2.32)$$

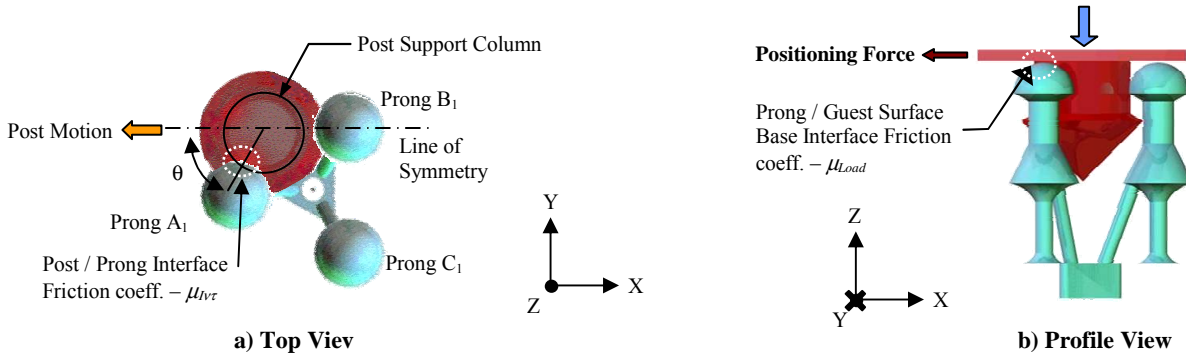


Figure 2.14: Positioning Force. During positioning, Prong A_1 slides around the support column of the post. Coulomb friction is assumed at this interface with coefficient μ_{Int} , to model the frictional effects of the interference between the post and prongs. As the guest surface is manipulated its base slides along the tops of the prongs. Coulomb friction is assumed at this interface with coefficient μ_{Load} to model the frictional losses due to the load.

$$\Delta_{prA_{1y}} = R_{po-sc} [\cos(60^\circ) - \cos(\theta)] \quad (2.33)$$

where R_{po-sc} is the radius of the post support column.

2.3.4.2. Final Positioning Model

These relative displacements are sufficient along with the enforcement of the known forces of Equation 2.31 to fully define the forces and displacements of the guest surface post as a function of the contact angle, θ . The net force available for the positioning of the guest surface post, $F_{Positioning}$, is then defined as

$$F_{Positioning} = F_{prB_{1x}} - 2 * F_{prA_{1x}}. \quad (2.34)$$

The positioning force can be solved for using analytical methods as was done for the engagement and retention force (Equations 2.17 and 2.22). While the solution is closed form, it is very complex and long and thus is not given here. Positioning behavior is smooth beginning with a large locked force and tapering linearly towards zero force when the prongs are fully deflected. Qualitatively, the transition point of the guest post between the current cell and the adjacent cell is dependent on the friction levels for the surfaces. For high friction surfaces, large actuation triangle displacements are required and the positioning force suffers. Fortunately, losses due to friction are dominated by the effects of μ_{Load} and not μ_{Int} . Recalling Figure 2.14, μ_{Load} is the coefficient of friction at the interface between the tops of the prongs and the guest surface base. These surfaces are the most exposed and easiest to finish smoothly. In contrast, the post support columns and the sides of the prong connection topologies (surfaces impacted by μ_{Int}) are more difficult to finish and thus rely more heavily on the smoothness of the fabrication process.

2.3.5. Experimental Model Validation

A series of experimental tests were conducted to progressively explore the accuracy of the analytical model using three operational scenarios: single-cell free deflection, three-cell

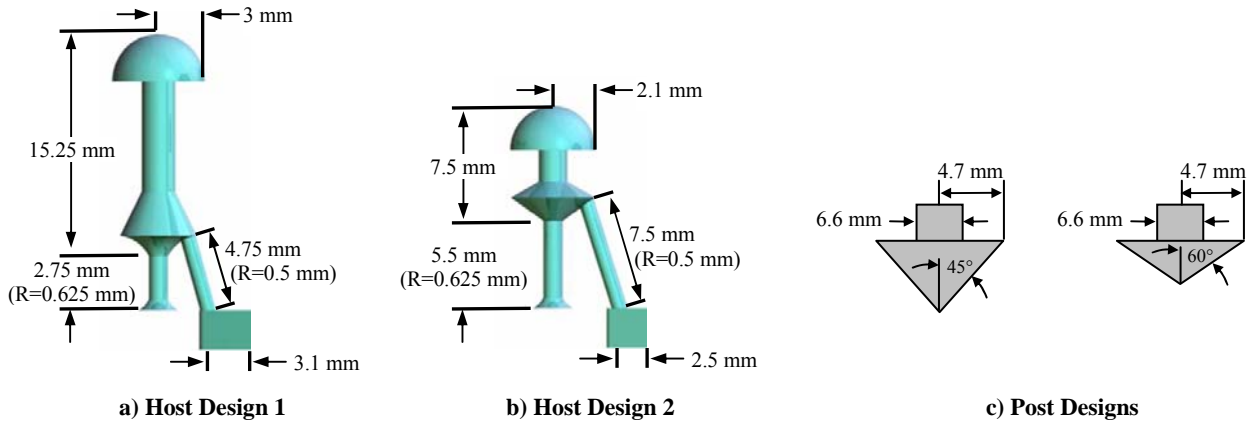


Figure 2.15: Experimental Test Sample Designs. Two different designs were fabricated for experimental testing. **a)** Design 1 is modeled after the prototype tested in prior research¹² **b)** Design 2 is the result of refinement to reduce the prongs' height while maintaining the same prong spacing and reducing stress levels. **c)** Two post designs, differing only in the conical half-angle, were used to examine the engagement behavior. A 4.7 mm maximum post radius, R_{po} , was used for both samples while the lead surface conical half-angles were 45° and 60°.

positioning, and single-cell engagement/retention. To begin, the free deflection of a single-cell surface was validated without considering the interactions between cells or the effects of friction. The cell interactions were examined in the positioning force experiments with a three-cell host surface and the frictional effects were examined during the engagement and retention of a guest surface into a single-cell host surface.

2.3.5.1. Test Samples

For these experiments two topological designs (Figure 2.15) were used for both single-cell and three-cell host surface test samples. Design 1 was based on the reduced-scale test bed with 18 mm tall prongs spaced 6.35 mm from the center of the actuation triangle. Design 2 was the result of optimization using the analytical model to reduce stress levels while maintaining the same prong spacing and reducing the prong height. Design 2 uses longer suspension lines and prong columns while reducing the overall prong height to only 13 mm. Other changes in geometry are presented in Figure 2.15. Examination of the single cell engagement and retention behaviors were accomplished using two guest surface designs each with the same radius, $R_{po} = 4.7$ mm, but differing lead surface half-angles, 60° and 45°. All guest and host surfaces were fabricated with a 3D-Systems SLA-250/40 stereolithography machine using Somos 8110 resin. After the part was created, it was cleaned using a Branson 3200 Ultrasonic cleaner to remove any uncured resin. The layered building process inherent to stereolithography produces a very rough surface finish on the prototypes, which increases the engagement force and impedes motion due to excessive friction. To improve this finish, liquid resin was hand applied to the connection elements of the cleaned prototype. The prototype was then cured for 15 minutes in a 3D-Systems Post-Cure Apparatus (PCA). A second coat of liquid resin was applied to the connection elements and the prototype was cured for 60 additional minutes (Figure 2.16).



a) Unfinished Rough Surface b) Finished Smooth Surface

Figure 2.16: Surface Finish Improvement. Two coats of uncured Somos 8110 resin were hand applied to the lead surfaces of the connection elements to minimize friction during engagement and motion generation. The finished surfaces were then fully cured in a 3D-Systems PCA.

2.3.5.2. Experimental Procedure

Similar laboratory setups and procedures were used for the different operational scenario experiments. To examine the kinematics and stiffness of the mechanism, an experimental setup capable of measuring the load on the actuation triangle and prong tip deflection in response to applied actuation triangle displacements was constructed. Displacements were applied to the actuation triangle using a Newport UMR 12.40 single-axis load bearing stage (Figure 2.17). By affixing a 25 lb Cooper Industries LPM 530 force transducer between the stage and the actuation triangle, the load on the actuation triangle could be measured simultaneously with the applied displacement. The prong's position in space was measured using an aluminum probe mounted to a Newport 462-XYZ-M three-axis precision stage via a 5g Cooper Industries LPM 620 force transducer. The aluminum probe was positioned using the three-axis stage until contact was made at the center of the prong connection topology allowing its position to be measured in three



a) Single-Cell Test b) Three-Cell Test

Figure 2.17: Experimental Test Setup. For both the single and three-cell tests displacements were imparted on the actuation triangles using a precision Newport single-axis stage. **a)** The single-cell free deflections of the prongs were measured using an aluminum probe attached to a three-axis Newport precision sage. This probe was attached to the stage through a 5 g force probe to insure that the prong position was measured accurately without loading the prongs significantly. For engagement and retention testing the aluminum probe was replaced with a single-post guest surface. **b)** For the three-cell samples the force at the tip of the Prong B₁ (Figure 2.19) was measured using an aluminum probe. The probe was mounted via a 10 lb Cooper Instruments force probe to a three-axis Newport precision stage. The probe was positioned using the three-axis stage to map out the force-deflection curve for the three-cell samples.

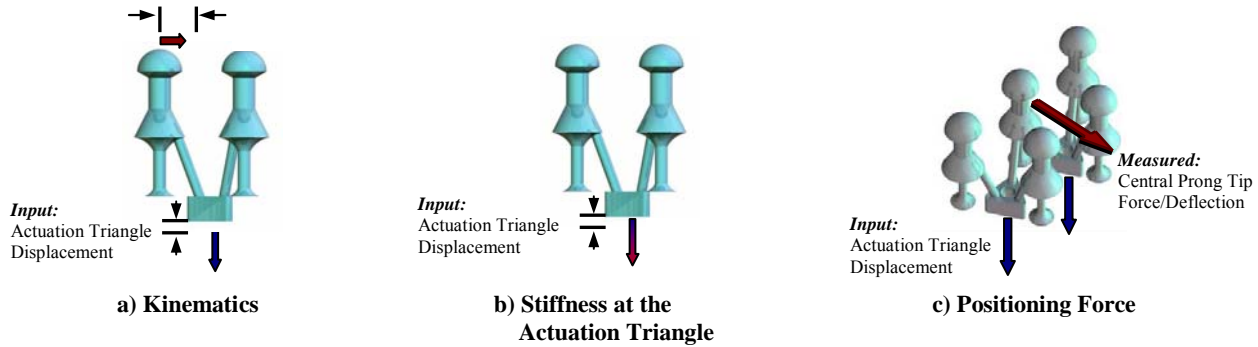


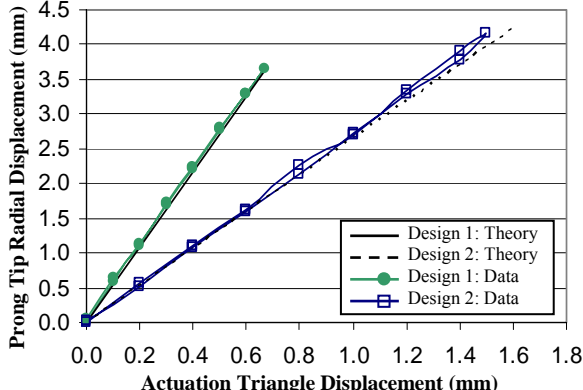
Figure 2.18 Experimental Input/Output Parameters. **a)** To examine the kinematics of the mechanism, the relationship between the input displacement at the actuation triangle and the resulting displacement of the prong tips was experimentally measured. **b)** The models ability to accurately account for the stiffness of the prong column and suspension lines was examined by measuring the force required to enact deflection of the actuation triangle. **c)** The potential positioning force was examined using a three cell host surface verifying the model's ability to capture cell interactions.

dimensions. To insure that the aluminum probe did not significantly alter the prong position, the force imparted by the probe was minimized using the sensitive 5 g force transducer.

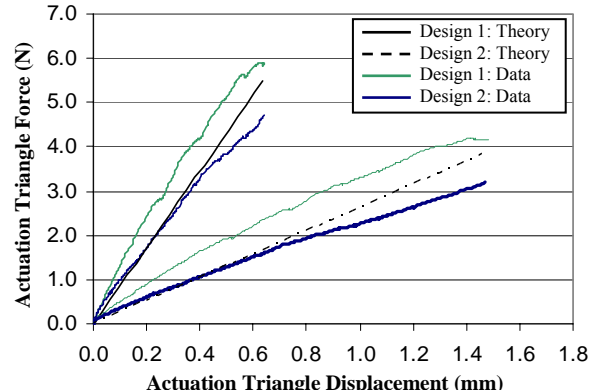
The setup was modified slightly to permit the examination of the single-cell engagement and retention behaviors by removing the aluminum probe and replacing it with a single-post guest surface. By mounting the guest surface to the Newport 462-XYZ-M via a 10 lb Cooper Industries LPM 530 force transducer, both the position and force imparted in the guest surface could be measured simultaneously. For the engagement and retention tests, the actuation triangles were separated from the single-axis UMR 12.40 stage to permit their free deflection in response to the guest surface motions.

2.3.5.3. Single-Cell Behavior Experimental Results

The free deflection kinematics of the mechanism (Figures 2.18a) was examined to verify the accuracy of the model in the absence of cell interactions and frictional effects. As observed in Figure 2.19a, the model captured the prong deflection extremely well with an average error of 1.7 % between both cases. More importantly it was demonstrated that the design could be tailored to the requirements of the intended actuation source. Design 1 required approximately 0.64 mm of actuation deflection and 6.1 N of force to fully deflect the prongs thus representing a low stroke, moderate force actuator requirement. In contrast design 2 requires a moderate stroke, low force actuation system with 1.6 mm of required deflection and 4.5 N of force. It is important to note that the two designs require differing degrees of prong deflection to reach the fully deflected state where the prongs are all touching each other. Since the prongs are typically deflected as far as possible during operation this state was used as the comparison point between the designs. Also of note is that the tip deflection of the prong was linear with respect to the input displacement of the actuation triangle. This is not often the case with compliant mechanisms and can be highly beneficial when developing a control system for the design.



a) Kinematics



b) Stiffness at Actuation Triangle

Figure 2.19: Single Cell Kinematics and Stiffness at the Actuation Triangle Experimental Results. a)

Prong tip radial deflection in response to displacements imparted to the actuation triangle was measured to verify the accuracy of the model's kinematics predictions without considering the build material modulus. A linear prong response for both designs was measured with design 1 requiring 0.6 mm of actuation stroke to generate 3.6 mm of prong deflection and design 2 requiring 1.5 mm of actuation stroke to generate 4.2 mm of prong deflection. The model accurately captured the prong deflection with an average error of 1.7% from the experimentally measured response. b) The force-deflection relationship at the actuation triangle was measured to determine if the model accurately captured the material behavior of the build material. Nonlinearity in the force-measurements was observed as a result of plastic deformations of the prong columns and the suspension lines. With displacement applied rapidly over 2 seconds, the response was linear, if applied over 60 seconds, over 23% depression of the force was observed. In the case of applying the deflection over 60 seconds, 18% error in the force measurements was obtained.

The stiffness at the actuation triangle was measured to determine if the material was modeled correctly and particularly if it exhibited any nonlinearities (Figure 2.18b). Because the actuators will be attached to the actuation triangle, an accurate estimate of the stiffness at this location is important for stiffness matching the actuator for maximum energy transmission. The force-deflection relationship for Design 1 (Figure 2.19b) demonstrates the plastic deformations occurring in the prong columns and suspensions as the force required to maintain a given prong deflection decreased with time. When the displacement was applied rapidly over 2 seconds, the response was linear but when applied slowly over 60 seconds, a 23% depression in the force at the actuation triangle was observed. This plastic deformation resulted in an average error of 18% from theory (Equation 2.10). After the tests, residual displacements of the actuation triangle were up to 13% of the applied deflections indicating elevated stress levels leading to plastic deformation during the testing. The stress and plastic deformation can be mitigated through proper selection of dimensions.

2.3.5.4. Engagement Experimental Results

Frictional effects were examined by the introduction of the post in a single-cell host surface. Single-cell engagement testing demonstrated that successful attachment of guest and host surfaces could be accomplished with minimal force (< 0.58 N) even in the presence of friction (Figure 2.20). The general shape of the engagement behavior was captured well with a linear initial stage up to the transition point, and a nonlinear response after the transition point with the slope of the curve decreasing until engagement is complete. Generally the model was

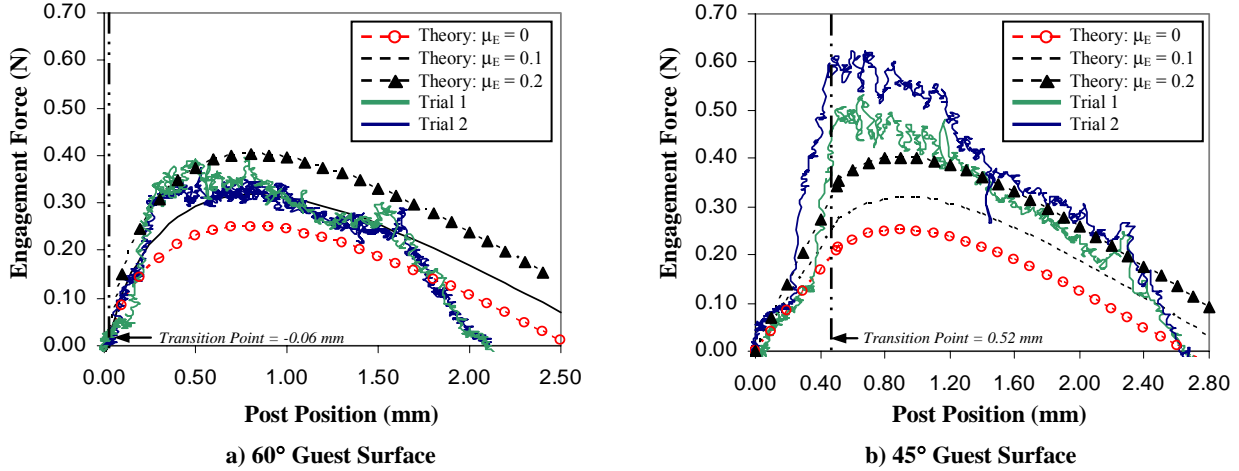


Figure 2.20: Engagement Force Experimental Results. The relationship between the engagement force and the imparted guest surface post displacement was examined and compared to model predictions. Two guest surfaces were fabricated with identical 4.7 mm radius conical lead surface but varied cone half-angles, 60° and 45°. The 60° guest surface required an average force of 0.39 N to engage compared to the predicted force of 0.32 N and 0.40 N for estimated friction levels of $\mu_E = 0.1$ and $\mu_E = 0.2$ respectively. The 45° guest surface response was not predicted accurately due to excess levels of friction and unsmooth guest and host surfaces. This caused the engagement response to increase sharply after about 0.25 mm of post displacement. Up to this point the model predicted the response accurately. An average force of 0.58 N was required to engage the 45° guest surface well above the predicted force of 0.32 N for $\mu_E = 0.1$ and 0.40 N for $\mu_E = 0.2$.

accurate up to about 1.6 mm of post displacement for the 60° half-angle guest surface with an average error of 9.8% from the $\mu_E = 0.1$ theory and 15.6% from the $\mu_E = 0.2$ theory. After 1.6mm the force dropped off due to deviations in the prong shape from the idealized hemispherical shape. Over two trials, the 60° guest surfaces required an average maximum force of 0.39 N to engage compared to a predicted maximum of 0.32N for an estimated $\mu_E = 0.1$ and 0.40 N for $\mu_E = 0.2$. Inconsistent friction levels were evidenced by the jagged force measurements and the overall trend in the data where it tracked the $\mu_E = 0.2$ theory well up to 0.35 mm of post displacement before dropping down to the $\mu_E = 0.2$ theory line.

Testing of the 45° half-angle guest surface yielded interesting results that highlighted the sensitivity of the design to manufacturing defects. Up to a post displacement of 0.25 mm the response tracked theory well with an average error of only 6.7% for an estimated $\mu_E = 0.1$ and 7.6% for $\mu_E = 0.2$. At 0.25 mm of post displacement the prong and post began to stick together instead of sliding smoothly across each other and the force rose sharply requiring a maximum force of 0.58 N to engage compared to a predicted maximums of 0.32N and 0.40 N for estimated friction levels of $\mu_E = 0.1$ and $\mu_E = 0.2$ respectively. The deviations from the predicted behavior are the result of three factors stemming from the shortcomings of the stereolithography fabrication method employed: the prong is not perfectly hemispherical, the post is not perfectly conical, and the friction levels are not constant across the surfaces.

2.3.5.5. Retention Experimental Results

Frictional variances also played an important role in the observed retention behavior. The hand coating process employed on the leading surface was not applied to the trailing edge

surface. For all samples, the surfaces were sanded with 200 and 400 grit sand paper until they felt smooth to the touch but clearly the ridges were not completely eliminated or new ridges were introduced in the finishing process. However it was difficult to fully smooth the surface without affecting the shape. Doing so resulted in post and prong trailing surfaces that were not mutually parallel.

Experimental testing of the retention behavior clearly indicates that the trailing surface were not smooth as the force-deflection response was quite jagged. Even with the jagged response the general trend is still clear throughout the separation process (Figure 2.21). Two test runs were performed resulting in an average maximum recorded retention force of 2.1 N compared to a predicted value of 2.2 N for the frictionless case and 2.85 N for a low friction case of $\mu_R = 0.05$. The experimentally observed retention force was up to 5.4 times greater than the engagement force for identical surfaces. This feature of the Active Velcro technology allows the engagement forces to be kept small to insure a successful attachment while simultaneously creating a substantial retention force to prevent undesired guest surface separation.

As evident in the theory lines of Figure 2.21 the retention behavior is highly sensitive to friction. Furthermore the evenly spaced “teeth” in the measured response highlight the minute ridges present on the post and prong trailing surfaces from the stereolithography process. Prior to the sanding, the ridges were sufficient to prevent separation of the guest surface post without damaging the prongs, hence creating a significant retention force. Preliminary testing with unfinished surfaces generated retention forces in excess of the 25 lb Cooper force probe’s limitations.

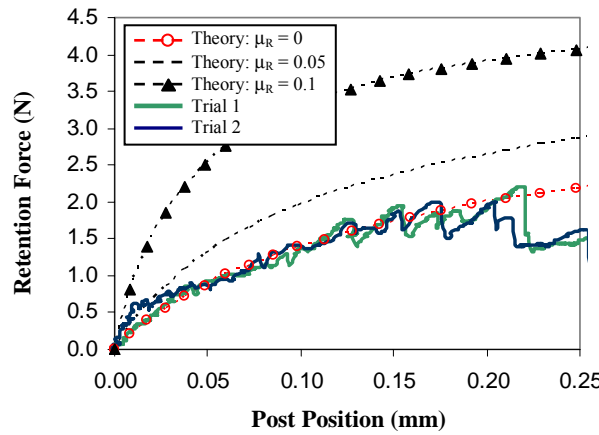


Figure 2.21: Retention Force Experimental Results. The relationship between the retention force and the imparted guest surface post displacement was examined and compared to model predictions. Three trial runs were performed using the same host and guest surfaces resulting in an average maximum recorded retention force of 2.1 N compared to a predicted value of 2.2 N for the frictionless case and 2.85 N for a low friction case of $\mu_R = 0.05$. Retention was highly sensitive to friction levels particularly at the onset of surface separation. For friction coefficients above approximately $\mu_R = 0.13$, the theory predicts that the surface will not separate.

2.3.5.6. Positioning Force Experimental Results

The ability to manipulate an engaged guest surface without releasing is the primary benefit of the Active Velcro surface when compared to the current state of the art. To begin examining the potential forces available for object manipulation, the positioning force was examined for a gait 1 translation (Figure 2.8) of a single post. A three-cell Design 1 sample was mounted to the laboratory bench between two vises. The two actuation triangles were mounted to a Newport UMR 12.40 single axis stage which was utilized to apply known deflections to the actuation triangles (Figures 2.17b, 2.18c). A single guest surface post ($R_{po-sc} = 3.3$ mm, $\chi = 45^\circ$, $R_{po} = 4.5$ mm, Figure 2.15c) was mounted to a Newport 462-XYX-M three-axis stage via a Cooper Industries LPM 530 force transducer (replacing the aluminum probe of Figure 2.17b). The guest post was initially engaged into the central prong cell depicted above in Figure 2.8. The actuation triangles were deflected 0.6 mm and held at this position through the test. This is the deflection that would result in the prongs fully deflecting under free-deflection (i.e. no prong tip loads) boundary conditions. The post position was varied from the initial position centered within the cell to the free-deflection position while the force imparted on the post was recorded, thus generating a force-deflection curve for the post response as it was positioned out of the central cell.

Three trials were performed using the same host and guest surfaces. The force-deflection response was approximately linear reaching an average blocked positioning force of 0.6 N and an average free deflection of 2.8 mm (Figure 2.22). The model successfully captured the force-deflection response of the single-post guest surface with an average error of only 3.3% with $\mu_{Int} = 0.2$ and 3.5 % for $\mu_{Int} = 0.4$. The closeness of the three theory lines plotted on Figure 2.22

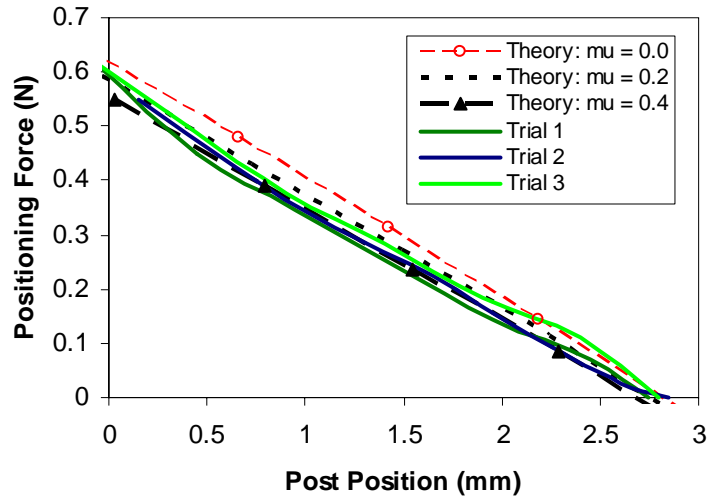


Figure 2.22: Positioning Force Experimental Results. The relationship between the positioning force and the imparted guest surface post displacement was examined and compared to model predictions. Three trial runs were performed using the same host and guest surfaces resulting in an average measured blocked force of 0.6 N and an average measured free-deflection of 2.8 mm. Since the coefficient of friction between the post and prongs was not experimentally measured, three different theory lines were included for friction coefficients of $\mu_{Int} = 0$, 0.2, and 0.4. The model accurately predicted the measured response with an average error of 6.5%, 3.3%, and 3.5% for $\mu_{Int} = 0$, 0.2, and 0.4 respectively. It is assumed that the actual friction coefficient is approximately 0.2 based on the test results.

highlight the insensitivity of the design to friction levels between the post and the prongs during translation. Even for a large friction coefficient of $\mu_{Int} = 0.4$ the blocked positioning force drops by only 10% when compared to the frictionless case. Here, the blocked force is defined as the maximum force the host can apply to a guest post when it is centered within the prong cell. Thus it is the available holding force of the host. However, when positioning is desired the post must be translated until the post's equator passes through to the next cell.

2.4. PROOF OF CONCEPT DEMONSTRATION AND EVALUATION

To demonstrate and evaluate the primary functions of the Active Velcro several different prototypes were designed, fabricated and experimentally characterized. Initially a large scale prototype was built from off-the-shelf components to confirm the general functions of engagement, retention and positioning. While this prototype provided useful qualitative assessment, it was too large for quantitative evaluation. Therefore, reduce-scale prototypes were fabricated and integrated with a basic stamp control system to experimentally evaluate loading along with basic path planning operations. For a proper connection, motion and stress levels in all the prototypes, it was critical to select the correct parameters for the surface. As such a pattern refinement simulation was developed to help reduce interference during rotation and select the proper spacing and dimensions for the surfaces. This section provides an overview to the pattern refinement along with description of the fabrication and experimental testing of both types of prototypes.

2.4.1. Pattern Refinement

There are three important criteria which should be imposed on a guest surface meant for both translation and rotation. First it should experience a minimum of resistive interference during both translation and rotation to reduce the loss of positioning force to frictional. This interference is the result of contact between the head of each prong (radius R_h) and the post's support column (radius R_{po-sc}) and is affected by the distance between each post, Δ_{po} . Second, the levels of interference should be similar regardless of the guest orientation and position to ensure that positioning force and torque applied to the guest surface is consistent across the entire host array. Finally, the patterns must ensure that each post remains in contact with at least one prong at all times time to prevent undesired guest surface release.

To guide in the selection of surface parameters, a basic simulation program was developed based upon an approximation of the force and torque using the undeformed host surface shape. During a translation, the posts must force their way between any interfering prongs. This results in a net force, \vec{F} , on the guest calculated by summing the individual forces imparted by each of the n interfering prongs as they are deflected a distance x_i ,

$$\vec{F} = \sum_i^n k \vec{x}_i . \quad (2.35)$$

minimal normal forces ($F_N = 0.09N$ for Design 1 and $\mu_I = 0.1$) generated between the post and interfering prongs A_1 and A_2 . In contrast, the normal forces created during both engagement ($F_N = 0.27N$ for $\mu_E = 0.1$) and retention ($F_N = 1.5N$ for $\mu_R = 0.1$) are significantly higher and thus more impacted by frictional variances. The experimentally measured 0.6N blocked force is one to two orders of magnitude greater than those of current MEMS based systems (Table 1.1) demonstrating a significant improvement in positioning force capability. If multiple posts are used, several Newton's of force are possible making it a viable technology for complex motion generation in the low gravity environment of space, the turbulent underwater environment, or aboard moving ground, sea and air vehicles.

Proof-of-concept prototypes were fabricated at two scales: one at a large-scale (26 x 22.5 x 6 cm) using off-the-shelf components, and a second at a reduced-scale (12 x 10 x 6.3 cm) utilizing stereolithography. Experimental testing has verified that the Active Velcro surface is capable of full planar translation and 360-degree rotation with translation speeds of up to 3.7 mm/s on the large-scale prototype and 2.8 mm/s on the reduced-scale prototype. Rotational speeds were similar for both test-beds at 2.3 deg/s for the large-scale and 2.5 deg/s for the reduced-scale systems. The Active Velcro surface as a whole is capable of generating motion at a faster rate than the individual actuators that comprise the surface by utilized phased activation. Utilizing a redundant system of SMA actuators, an effective increase in the surface bandwidth of up to three-fold was observed when compared to the bandwidth of the individual SMA wires. This response is due to the fact that the wires are not required to fully cool before a guest surface post can be passed between individual prong groupings (translation increments). A basic stamp control hardware running the A* path-planning algorithm successfully found the shortest path between any initial guest position and orientation and the final destination. The entire portable system ran off two 1.2 V NiMH with several hours of expected continuous operation.

This research demonstrated this new technology and established the necessary engineering models to extend this to other applications and modes (locomotion, morphing). It is critical for unstable environments (space, fluidic, moving, vibration, etc) where active connection and motion is simultaneously required. No other connection device has the ability to generate such large planar motion and no other distributed manipulation surface has the connection ability. Active Velcro is unique in this aspect and represents a complete paradigm shift in how we connect our world.

2.6. REFERENCES, SECTION 2

Ataka, M., Omodaka, A., Takeshima, N., Fujita, H., 1993, "Fabrication and Operation of Polyimide Bimorph Actuators for a Ciliary Motion System," *Journal of Microelectromechanical Systems*, Dec, Vol. 2, No. 4, pp 146 - 150.

Bohringer, K.F., Donald, B.R., MacDonald, N.C., 1999, "Programmable Force Fields for Distributed Manipulation, with Applications to MEMS Actuator Arrays and Vibratory Parts Feeders," *International Journal of Robotics Research*, Feb., Vol. 18, No. 2, p 168 – 200.

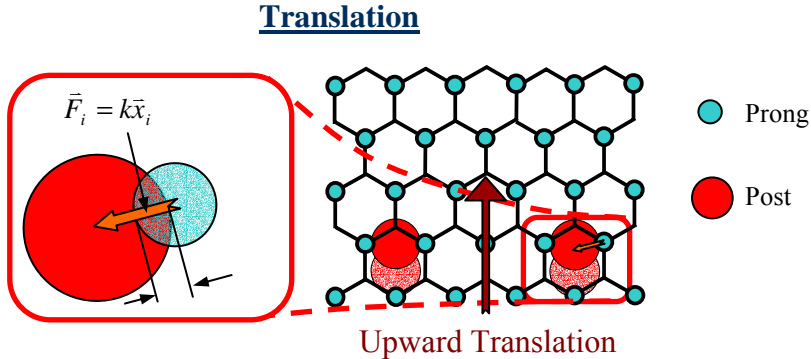


Figure 2.23: Interference During Translation. As the guest surface translates through the host surface prong field interference is created between the posts and prongs. This interference force is summed for all interfering prongs and can be either be resistive in that it fights the desired translation, or beneficial in that it aids the desired translation.

For this estimation it was assumed that the prongs could be modeled as linear springs of stiffness, k , as depicted in Figure 2.23. The assumption of a linear stiffness was experimentally validated in *Section 2.3.5.3 Single-Cell Behavior*.

Similarly, the net interference torque, \vec{T} , was calculated by estimating the net torque imparted by the guest surface to all interfering prongs to deflect them out of the way during rotation,

$$\vec{T} = \sum_i^n \vec{R}_i \times \vec{F}_i. \quad (2.36)$$

This estimation assumed that one post would act as a pivot point, therefore the radius of rotation, \vec{R}_i , was defined as the distance from the pivot point to the location of interference for

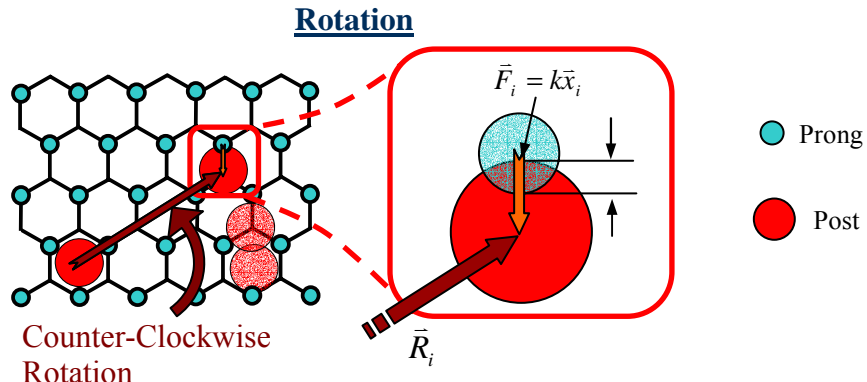


Figure 2.24: Interference During Rotation. As the guest surface rotates through the host surface prong field interference is created between the posts and prongs. This interference torque is calculated using the cross products of the force vector and the vector from the instant center of rotation to the contact point summed for all interfering prongs. This torque can either be resistive in that it fights the desired rotation, or beneficial in that it aids the desired rotation.

each i^{th} , prong as depicted in Figure 2.24. Therefore with a two-post guest surface, \vec{R}_i is equal to Δ_{po} . An equivalent four-post surface is obtained by reflecting this two-post surface through 60° and 120° creating a symmetric guest similar to that of Figure 2.5b.

A Matlab routine was developed to calculate both the net interference torque and force resisting rotation/translation as a guest is first rotated through 60° and then translated a single step. Since the host surface was already constructed, its geometry was held constant while R_{po_sc} and Δ_{po} were allowed to vary. Both unknowns were incrementally changed until a solution was found that is translatable, had consistent resistive torque throughout rotation, and insured contact between each guest post and the host prongs at all times. This simple approach quantified the interference torque and force encountered by a manipulated guest surface and was used to find near optimal solutions but the determination of an absolute optimal solution was not guaranteed.

Figure 2.25 depicts the routine's output for a two-post large-scale guest surface as it rotates through 60 degrees and translates one step. The upper graph displays the torque encountered by the guest surface during rotation. The second graph displays the number of prongs contacting the post at any given time. At all times there should be at least one prong contacting each post, to insure that the guest surface is retained throughout the motion. The third graph displays the forces encountered by the guest surface during translation. Negative values of torque/force represent beneficial interference that aids the intended motion, while positive values represent resistance to motion.

This was applied for the large and reduced scale prototype. For the 6.35 mm prong connection topology and 13.9 mm prong cell radius of the large-scale host surface, it was determined that a post radius of 9.5 mm was optimal. The optimal post separation was 66.2 mm even though this spacing does not place each post exactly in the center of a prong grouping. This spacing results in the second prong being 6 mm away from the center of its prong grouping. For the reduced-scale test bed with 3.0 mm prong connection topologies and a 6.35mm prong cell radius, the refined guest surface consisted of two 3.6 mm radius posts placed 21 mm apart. Thus, the guest surface spacing places the second post 1.0 mm from the center of its prong grouping.

2.4.2. Large-Scale Prototype Test Bed

A large-scale prototype was originally designed and constructed to demonstrate the motion generation capabilities of the Active Velcro surface. The system was developed as a basic proof-of-concept and was not optimized for minimal power consumption, speed of motion, or maximum motion resolution. However, the prototype is highly adjustable and easily serviceable because it is composed of discrete parts. These features facilitated the large-scale prototype being an effective original test bed for examining translation and rotation techniques.

2.4.2.1. Large-Scale Prototype Fabrication

The large-scale prototype test bed was fabricated using off-the-shelf components chosen based on the availability of materials and ease of construction. The host surface was constructed of a hexagonal array of 75 prongs mounted to a 13 mm thick polyethylene plate via 0.81 mm

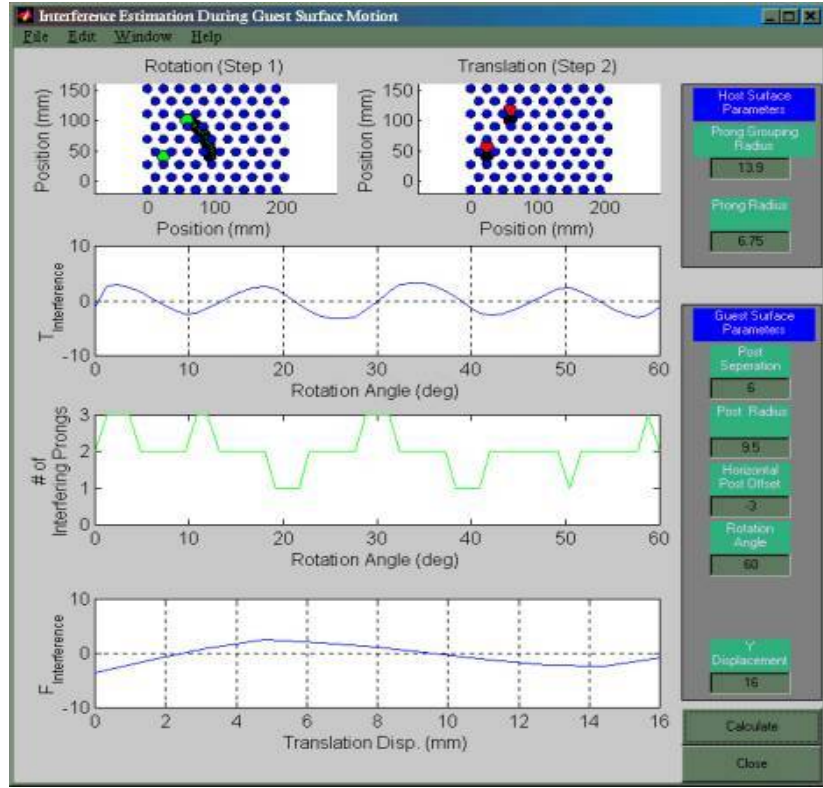


Figure 2.25: Sample Results of Pattern Refinement. A Matlab routine was developed to find the optimal post column diameter and spacing for improved rotation through the current large-scale test bed resulting with a diameter of 9.5 and a spacing 66.2 mm. The upper plot displays the torque encountered by the guest surface during a 60-degree rotation. The middle plot displays the number of prongs which are in contact with the rotating guest surface at any given time. The lowest plot displays the forces encountered by guest surface during translation of a single step.

steel music wire. The music wire served as a flexure hinge allowing the otherwise rigid PVC prong (6.35 mm diameter, 50 mm tall) to pivot when actuated. Each prong was finished by adhering a wooden cap (.3 mm diameter, 5.6 mm tall) to the top of the prong to form the required connection topology.

Prongs were spaced 26 mm apart and arranged into groups of three forming the individual prong cells. At the center of each cell was an actuation circle (functionally identical to an actuation triangle) fabricated from a 17.5 mm diameter Delrin rod with a 3.5mm center drilled hole. The rod was diced into 2.5 mm thick circles and three axi-symmetric grooves were machined into the bottom into which three steel wires were fitted. The free ends of the steel wires were attached to the bottom of three adjacent prongs, suspending the actuation circle in the center of the prong cell. This assembly serves to transfer the work of the SMA wires to the prongs.

A second 13 mm thick polyethylene plate was used to serve as a lower anchoring point for the SMA wire. Holes of 5.5 mm diameter were drilled through both the top and bottom polyethylene plates to allow the SMA wire to pass through. A total of 61 SMA wires were

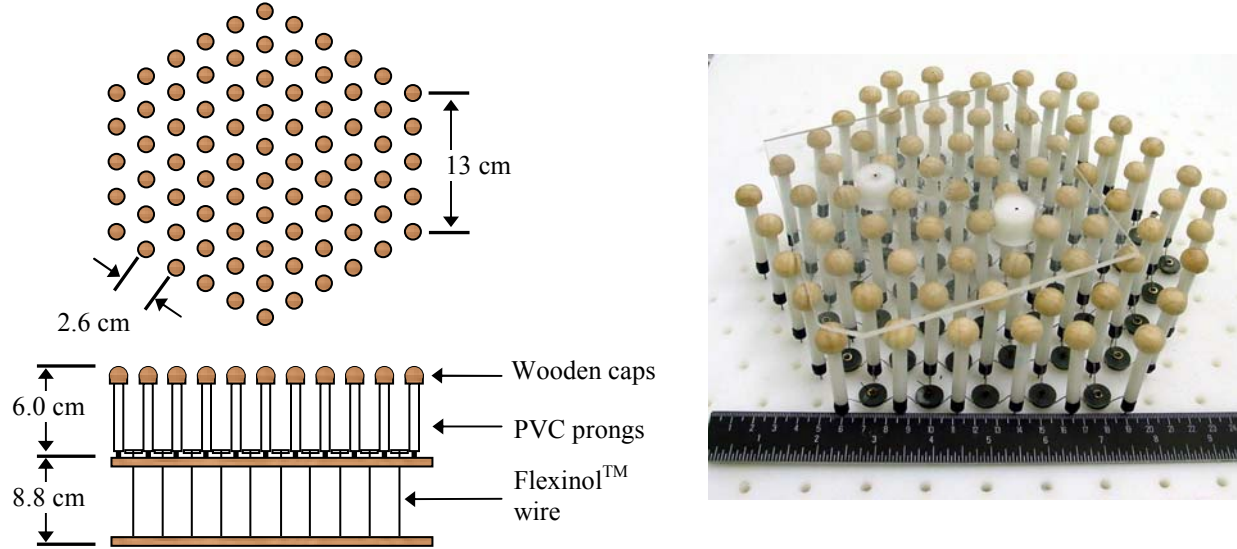


Figure 2.26: Large-Scale Prototype. A large-scale prototype was fabricated using off-the-shelf components to prove the motion generation capabilities of Active Velcro.

strung from the actuation circles through the lower base. The SMA wire was held in place at the actuation circles using the lead-holding mechanism from a 0.3 mm mechanical pencil and with a pin vise at the lower base. The 0.38 mm diameter Flexinol™ SMA wire (purchased from Dynalloy) was rated for a maximum pulling force of 2000 grams with a transition temperature of 90°C. The active length of SMA wire for the completed large prototype test bed was 82 mm (Figure 2.26).

Several representative guest surfaces were constructed with varying numbers of posts (1, 2, 3, 4, 7). All guest surfaces were constructed in a similar manner using 142 mm square Plexiglas plates and mounting 24 mm diameter conical end topology posts (fabricated using stereolithography or machined Delrin rods). Rotation tests were performed using the two-post guest surface while the one and three-post guest surfaces were used for translation. Further translation testing using the Phased Activation approach was performed using the four and seven-post surfaces.

2.4.2.2. Procedure

For all positioning tests, the SMA wires were energized by shorting the output of a Samlex PSA-310 power supply across the subset of SMA wires specified by the gait and desired guest surface motion. When possible, each wire received approximately 2.75 A resulting in a 4.9 W of power draw per wire. However, the 10A limit of the Samlex supply impacted the results when more than three SMA wires were energized simultaneously. In that case the 10 A was divided equally amongst all energized wires. Reduced current slowed the SMA response time but still permitted resistive heating to raise the temperature of the SMA wires above the transition temperature, thereby causing the SMA wires to contract. Under the room temperature conditions of the lab, the application of 2.75 A to each wire resulted in heating and cooling times of approximately 0.7 and 9.0 seconds respectively.

Table 2.2: Performance Metrics for the Large-Scale Test Bed

| | |
|---------------------------------|------------------|
| Step Size (1/resolution) | 17 mm |
| Linear Speed | 3.7 mm/s |
| Rotational Speed | 2.3 deg/s |
| Input Power (per wire) | 4.9 W |

2.4.2.3. Translation Experimental Results

Planar translations were successfully demonstrated using the large-scale prototype with both single-post and three-post guest surfaces (Table 2.2). The lengths of translations were limited only by the size of the host surface (single-post tests) and the number of SMA wires integrated into the host surface (three-post tests). Positioning occurred by incrementally moving an engaged post from one cell to the next, resulting in 17 mm steps per activation cycle. This large step size is the distance between adjacent cell centers and is representative of the minimum controllable translational increment using simple ON/OFF control of the SMA wires. An average linear translational speed of 3.7 mm/s was recorded when positioning a single-post guest. Because of the hexagonal prong array, a true linear translation was not possible and the saw-toothed approximation to linear motion depicted in Figure 2.4b was performed. Thus the quoted linear speed was computed based on the Euclidian (straight line) distance between the starting and ending points of translation and time was extracted from the examination of a digital video recording taken during the experiment. The speed does not include the extraneous distance traveled due to the saw-toothed motion.

2.4.2.4. Rotation Experimental Results

Planar rotation was demonstrated using a two-post guest surface achieving a maximum orientation speed of 2.3 deg/s. Rotation testing was performed in two manners. First, the guest surface was pivoted about one of the posts. For this fixed center-of-rotation testing, the prongs engaging the pivot post were not deflected while the prongs engaging the second post were deflected. It was not necessary to apply an external load to the pivot post to prevent it from moving during testing. This fixed center-of-rotation testing yielded a maximum repeatable rotation of approximately 40°. Sixty degrees of rotation was obtained, but was not repeatable due to excessive interference between the moving post and the host surface prong array above 40 degrees due solely to the selected test bed geometry. In the second method, the pivot point location was allowed to vary. For rotation about points other than a post location, the prongs engaging both posts were deflected simultaneously. The variable center-of-rotation testing yielded a full 360 degrees of rotation demonstrating the essential orientation property of the Active Velcro mechanism.

2.4.2.5. Discussion

While the large-scale prototype is considerably larger than the final system should be for most applications, there are a number of important observations that can be made. The repeatable planar translation and rotation capabilities demonstrated the viability of the motion generation method on the large-scale and the promise of Active Velcro. The motion generation was repeatable using a hand built prototype with off-the-shelf components despite flaws in the

construction, such as differences in the height and spacing of the prongs, asymmetries in the actuation circle and its three suspension lines, and variations in the overall stiffness of each prong. While the errors in construction have not been quantified, the repeatable translations and rotation obtained despite the errors reveal an insensitivity of the system design to flaws in construction. The overall power was high, 4.9 W, due to the large scale of the prototype. However, this is not a constant power draw and the prototype was able to run off of eight AA batteries.

The translation speed of 3.7 mm/s equates to approximately 0.3 translation steps per second, or 0.3 Hz. However, testing on the same 15 mil diameter SMA wires revealed a much lower 0.1 Hz bandwidth under similar room temperature conditions with no forced airflow (0.7 seconds heating, 9 seconds cooling). Therefore by integrating the SMA wires into the distributed Active Velcro surface, a three-fold increase in effective surface bandwidth was achieved. It is important to note that this performance increase is not due to the phased activation approach, although it has a similar effect. In this case, a given SMA wire may be energized on sequential steps but the wire need only *partially* cooled between these sequential steps. In contrast, the phased activation approach prevents any given wire from being energized on sequential steps thereby eliminating the need to cool a wire at all between steps which could increase translation speed to as high as 18 mm/s.

2.4.3. Reduced-Scale Unified-Host Test Bed

While the large-scale test bed successfully demonstrated motion capabilities, two significant concerns remained; its scale was significantly larger than that desired for many applications such as satellite docking and its fabrication methods required extensive time and skill due to a very large part count and necessary symmetry in construction. To address these concerns a refined reduced-scale test bed was developed to more accurately represent the final Active Velcro design by reducing the scale of the test bed. The stereolithography process was employed to improve the construction of the prototype for a higher degree of precision and accuracy while simplifying assembly by reducing the part count. Additionally, an electrical bus system was incorporated to simplify the integration of the host surface SMA wires and the control system.

2.4.3.1. Reduced-Scale Prototype Fabrication

The reduced-scale prototypes were fabricated with a 3D-Systems SLA-250/40 stereolithography machine using Somos 8110 resin (Young's modulus \sim 317 MPa, flexural modulus \sim 310 MPa, elongation to failure \sim 27%). After the part was created, it was cleaned using a Branson 3200 Ultrasonic cleaner to remove any uncured resin. The prototype was finished using the techniques depicted in Figure 2.16 above.

The reduced-scale prototype was built at approximately 1/3 the scale of the large-scale prototype. The host surface was fabricated in two pieces: the upper surface containing the prongs, connection topology, flexure mechanism, and the backbone / the lower surface acting as an anchoring point for the SMA wires. A separate base was utilized for testing purposes only and could have easily been fabricated along with the upper base in a single piece. The separate lower base was attached to the upper host surface using adjustable spacers, which were used to rapidly alter the active length of the SMA wire. As with the large-scale prototype, the lead-

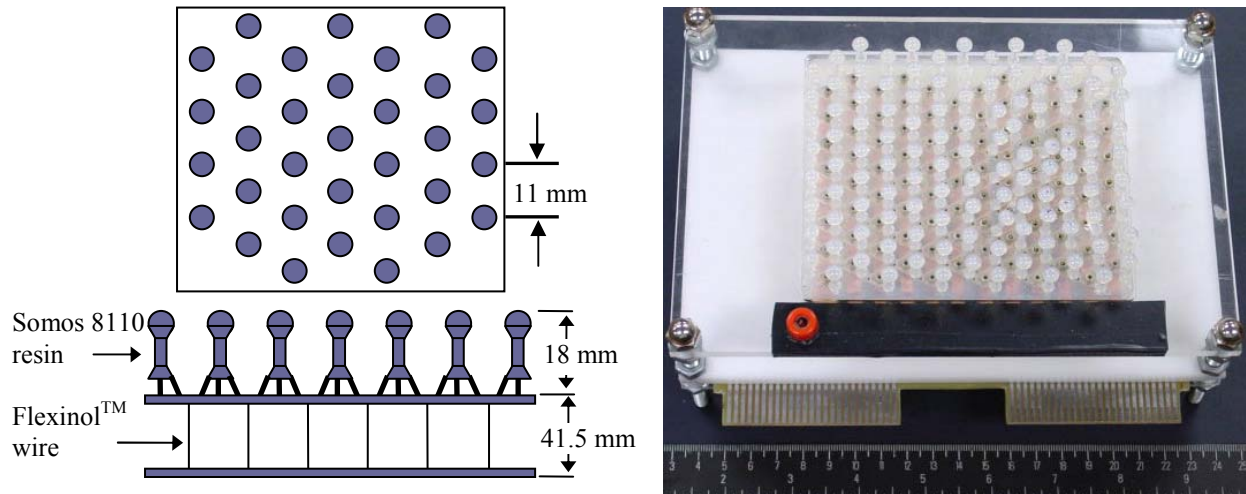


Figure 2.27: Reduced-Scale Test Bed. The reduced-scale prototype was fabricated with stereolithography using Somos 8110 resin at approximately 1/3 the scale of the large-scale prototype. The prototype successfully demonstrated translation and rotation capabilities while retaining the manipulated surface.

holding mechanism from a mechanical pencil was used to attach the SMA wire at the actuation triangle. The wires were secured beneath the base with 7.2 mm collars.

The stereolithography fabricated upper host surface measured 120 x 100 mm and contained 114 prongs as pictured in Figure 2.27. Each cell consisted of three 18 mm tall prongs spaced 11 mm apart in an equilateral triangular pattern. A 3.0 mm radius hemispherical connection topology built into the top of the prongs provided the engagement/retention capabilities. Three 1.5 mm diameter suspension lines suspended each actuation triangle from the prongs at a height even with the base. The lower host surface was mounted 30 mm below the upper surface, yielding an active SMA wire length of 41.5 mm. All testing was performed using a one-piece single-post guest surface. Single and two-post one-piece guest surfaces were fabricated and finished using the same techniques employed for the host surface (Figure 2.28). All guest surface posts were identical to insure comparable engagement/retention behavior and included 4.75 mm radius lead surfaces with a cone half-angle of 45° and horizontal trailing surfaces. Each post had a 3.6 mm radius support column and was spaced 21 mm apart in the case of the two-post guest surface.

2.4.3.2. *BASIC Stamp Control System*

A portable control system was developed with the ability to enact translation and rotation of multi-post guest surfaces to demonstrate the autonomous positing and orienting capabilities of the Active Velcro mechanism (Figure 2.29). This system was based around a BASIC stamp II (BS2-IC) chip, a micro controller with 16 fully programmable I/O pins capable of running programs written in a modified form of BASIC (Parallax BASIC) at approximately 4000 operations per second. The stamp was mounted to a Parallax designed board (Model: Board of Education, www.parallaxinc.com) which included a 5V power regulator designed to run off of a 9

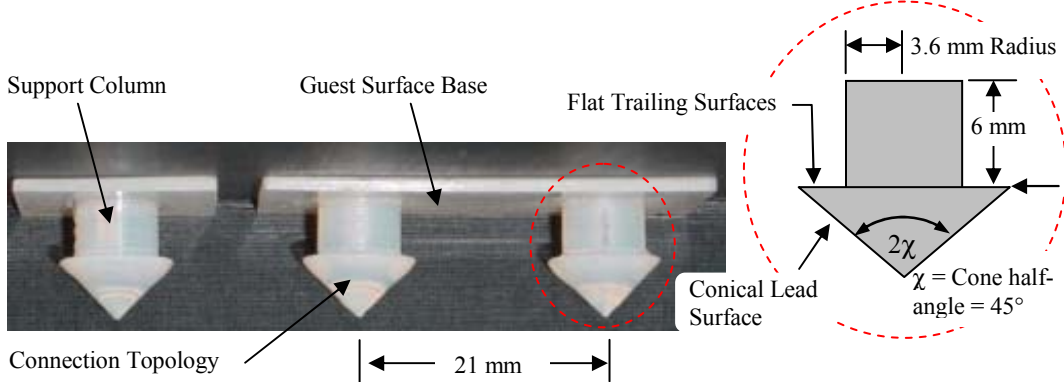


Figure 2.28: Demonstration Guest Surfaces. Two guest surfaces were fabricated using stereolithography and SOMOS 8110 resin to demonstrate the translation and rotation capabilities of the Active Velcro mechanism. Both guest surfaces used identical flat trailing surfaces and 4.75 mm radius 45° half-angle conical lead surfaces to insure comparable engagement and retention behavior. The 3.6 mm radius of the prong support column and 21 mm post separation was chosen to minimize interference to rotation.

V battery or external AC/DC power converter, a serial bus for downloading new routines to an embedded EEPROM memory chip from a PC, a small proto board, and connections to stamp's pins.

To demonstrate the capabilities of the Active Velcro design, two routines were programmed into the BS2 micro-controller, representing translation of a single-post guest surface and translation/rotation of a two-post guest surface under a typical docking scenario. The first step was to incorporate path-planning strategies to determine the route that the guest should take from a random initial position and orientation to the desired locking location. This task was accomplished through the implementation of A* path-planning algorithms first developed by Hart, Nilsson and Raphael, 1968. The algorithms were encoded within Matlab and are applicable for any feasible Active Velcro host surface geometries and two-post guest surface geometries. The current implementation guarantees that a successful path will be efficiently identified if one exists and returns a set of scripted motion to be enacted by the controller.

These scripted motions were sent to the SMA wires through a set of custom hand-soldered circuit boards: one decoder board and six amplifier stages. Figure 2.30 depicts the data and power flow throughout the control system. In short, control signals are sent from the BS2-IC to the decoder board containing a 4 to 16 DM74LS154N demultiplexer using a five-line bus: four of which are data lines and the fifth is a command line. The four data lines define which one of the sixteen octal latches the BS2-IC is to send signals to using basic binary logic. Thus to send a signal to the first octal latch, termed latch 0, a command signal of 0000 is sent using low power transistor-transistor logic (TTL) signals: 0V for the “0” signal, and 5V for the “1” signal. To send signals to the last octal latch, termed, latch 15, a signal of 1111 is sent. The demultiplexer takes the four-line input signal and activates one of its 16 output pins based on the signal sent. The signal from the command line is then assigned to this output pin. The command signal serves to turn on the desired octal latch for writing.

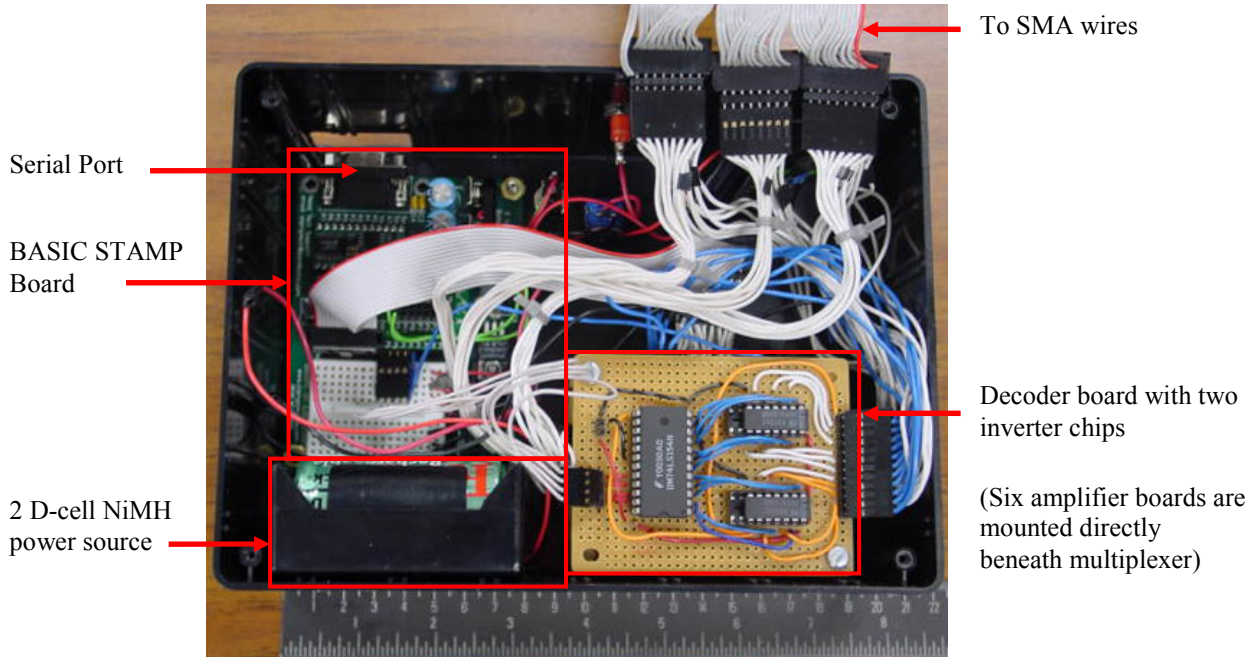


Figure 2.29: Control Unit. The control system is based around a BASIC Stamp controller that is capable of storing user-programmed routines using a serial port interface with a standard. Commands are sent from the BASIC Stamp board to the decoder, which disperses the signal to the correct amplifier boards. The amplifier boards then drive the SMA wires through two 50-pin ribbon cables. (only one cable is connected in the photograph).

Two DM74LS373 octal latches are included on each amplifier stage. Attached to each latch are eight IRLD110 MOSFET amplifiers. These are the amplifiers that eventually drive the SMA wires. Each latch can store commands for up to eight SMA wires. The desired state (on or off) for each of these eight SMA wires is sent to the amplifier boards using another TTL data bus from the BS2. In this bus, each line represents a single SMA wire with a “0” signal representing a wire to be energized. This eight-line data bus is attached to all latches simultaneously but only the single latch enabled for writing by the demultiplexer can be written to. The BS2 then cycles through each of the 16 octal latches until it has stored the entire set of SMA wires to be energized within the octal latches. Each latch holds the individual signal for its specific SMA wire and is capable of holding the signals while the controller determines the appropriate time to energize the wires. While the latches are holding the command signals, the BS2 is free to assign data to other latches, receive input signals from sensors or switches, or continue running its programmed routines. At the appropriate time an *output enable* signal is sent from the BS2 to all latches simultaneously, which send their signals to the MOSFET amplifier to supply the power to the desired SMA wire.

In operation, the SMA wires were driven by applying a common positive potential through the jack (visible in Figure 2.27) to the upper end of the SMA wires but activation occurred only when the control system forced the opposite end of the SMA wire to ground (driving the low side), thereby inducing current flow through the SMA. Resistive heating raised the temperature of the SMA wires above the transition temperature, thereby causing the SMA

wires to contract. Without control system input, the lower end of the SMA simply *floated* at the same potential as the upper end of the SMA wire and no activation occurs.

For the portable demonstration NiMH batteries were used to power the MOSFET and in turn the SMA wires. However, batteries cannot maintain a constant potential under high current loading conditions such as those experienced when driving multiple SMA wires simultaneously.

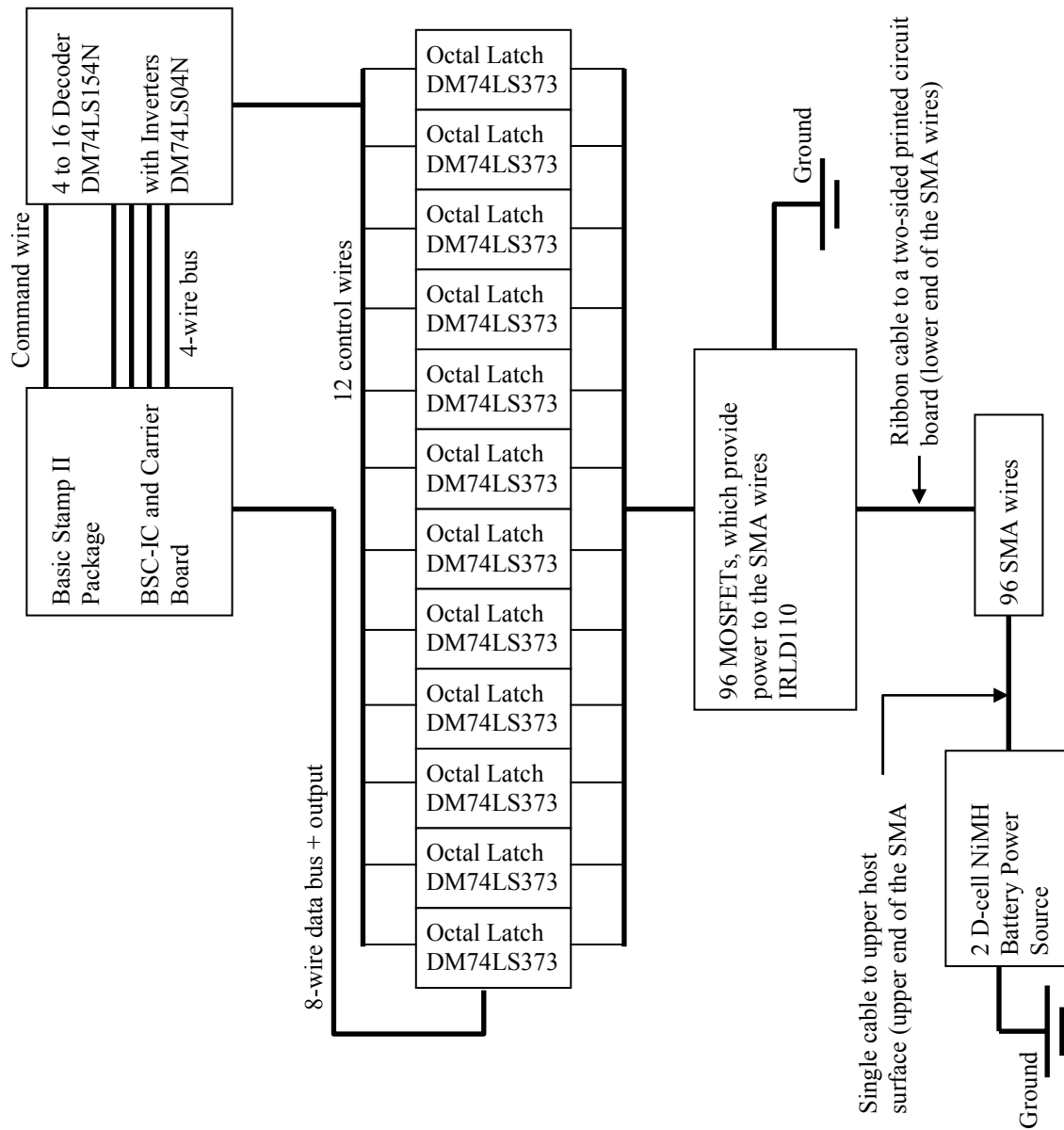


Figure 2.30: Control System Flow Chart. Two motion patterns were programmed in BASIC and downloaded to the BASIC stamp chip (BS2-IC). SMA control signals were sent from BS2-IC through a 4 wires bus to a 4-16 demultiplexer. The demultiplexer disperses the signal to the correct latch which stores the on or off signal for each SMA wire. Upon receiving an enable signal from the BASIC Stamp, the latches data is sent to the SMA wires through the MOSFET amplifiers.

Table 2.3: Performance Metrics for the Reduced-Scale Test Bed

| | |
|-------------------------------------|--------------------|
| Step Size (1/resolution) | 6.35 mm |
| Linear Speed | 2.8 mm/s |
| Rotational Speed | 2.5 deg/s |
| Engagement Force | 0.39 N/post |
| Retention Force | 2.1 N/post |
| Manipulation Force (blocked) | 0.6 N/post |
| Input Power (per wire) | 1.1 W |

The degree of voltage drop increases with the number of concurrently energized SMA wires. To insure that enough voltage was available to heat the SMA wires (note: the wires are actually driven by current, but this current is generated by driving a potential difference across the SMA) two 1.2 V D-cell batteries were wired in series. This resulted in 2.4 V available under minimal loading. However, 2.4 Volts is well in excess of the required 1.2 volts necessary to induce the 1 amp of current for 1 second activation of the 41.5 mm long 0.2 mm diameter SMA wires. Thus the *output enable* command sent from the BS2 to all the latches was pulse width modulated (PWM) with a duty cycle determined by the number of wires to be energized simultaneously. So a duty cycle of 50% results in the application of 1.2 V, while a duty cycle of 100% results in the application of all 2.4 V. For the manipulation of single and double post guest surfaces, a lookup table of duty cycles was generated to maintain relatively consistent levels of voltage (and thus current) regardless of the number of SMA wires being energized. This prevented excess current from being sent to the SMA wires during low load single-post manipulations while maintaining sufficient current levels during high load multiple-post guest surface manipulations.

2.4.3.3. Experimental Procedure and Results

By activating the reduced-scale prototype in an identical manner as large-scale prototype, repeatable translations of a single-post guest surface were achieved. Again, the number of sequential translation was limited only by the size of the prototype. A step size of 6.35 mm was utilized to demonstrate about a factor of three reduction in scale with respect to the large-scale prototype. The host surface successfully generated full planar translation of both one and two-post guest surfaces at speeds up to 2.8 mm/s (Table 2.3), 75% of the large-scale prototype's speed, while providing approximately 2.67 times more translation resolution. Using the same two-post guest surface, full 360-degree rotation was achieved at up to 2.5 deg/s. Both translation and rotation were possible regardless of the guest surface position and orientation on the host surface prong array.

Speed measurements were obtained by examining a digital video recording taken during experimentation. Power consumption, when compared to the large-scale prototype, was reduced by 77% to 1.1 W per wire with the application of 0.9 A to each SMA wire. To measure the required engagement force, a single-cell host surface was mounted to the laboratory bench between two vices while a guest post was mounted to a three-axis Newport stage via a Cooper Industries LPM 530 force transducer. Using the stage, the post was slowly guided into the center of the prong cell while the force transducer recorded the force until engagement was completed. The process was reversed to determine the retention force on the guest post. A maximum

recorded engagement force of 0.58 N per post was observed while retention forces exceeded 2.1 N per post.

2.4.3.4. Discussion

The reduced-scale prototype demonstrated the ability to fabricate the prongs, connection topologies, flexure mechanism, and backbone in a single piece while improving the accuracy and symmetry in the prototype. Because the stereolithography process is capable of rapidly fabricating complex three-dimensional structures, the construction of a single piece upper host surface was possible. This significantly reduced assembly time and insured that every prong was evenly spaced and aligned perfectly, something that was difficult to achieve with the hand fabricated large-scale prototype.

The A* path-planning algorithm employed in the research successfully finds the shortest path between any initial guest position and orientation to many potential goal positions if a path does exist. While many different goal positions and orientations are feasible, it is wise to align the goal orientation with the symmetry of the host prong array. This is recommended because of the coupling between guest translations and rotations that often occurs with an applied set of prong motions. With a goal orientation not aligned with one of the six preferred directions, depicted in Figure 2.31, it may be difficult to achieve both the goal position and orientation simultaneously. However, if the goal orientation is aligned with the array this problem is avoided by allowing guest translation without altering guest orientation. Additionally it is recommended that the goal position be located at the center of a prong cell since the guest posts are typically near the center of a cell when at a preferred orientation. Fortunately, during engagement, the topology will guide the guest into one of these preferred orientations.

The control system was successful at addressing all connected SMA wires in any pattern that was programmed into the BASIC Stamp controller. Desired motions could be programmed

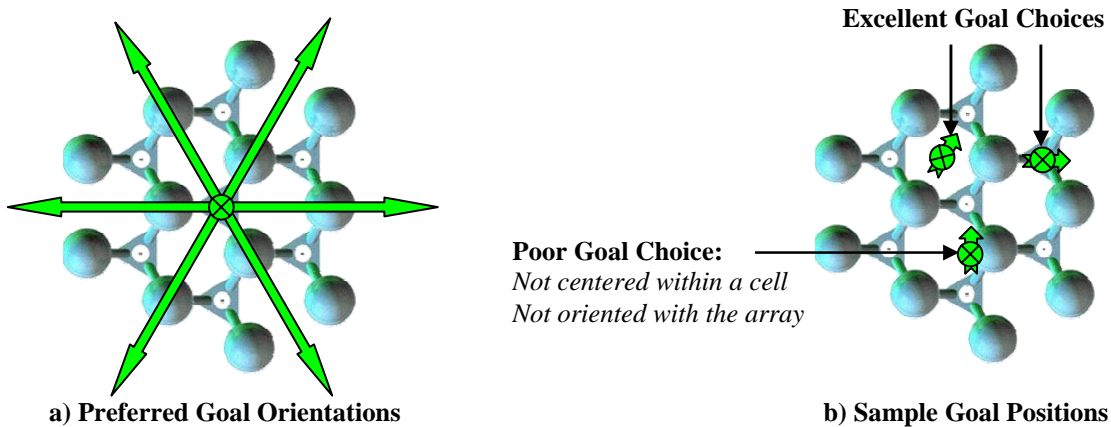


Figure 2.31: Preferred Goal Orientations. **a)** Whenever possible the goal location should be oriented in one of the six directions available for translation. This allows the guest to translate without altering its orientation. Without this condition, it is possible that the desired goal position and orientation can not be obtained simultaneously. This restriction does not need to be applied to the initial guest orientation, all are acceptable. **b)** Because each guest post will typically be near the center of a cell when at equilibrium, the goal position should be centered within a prong cell to increase the final positional accuracy.

quickly, downloaded to the prototype, and run in a matter of minutes. The system successfully enacted single and multi-post translations as well as full 360° rotation, meeting the goal of a fully operational small-scale demonstration system. Battery life for both the 9 V battery operating the electronics, and the two 1.2 V NiMH batteries proving power to the SMA wires has not been accurately determined but is on the order of two to three hours. Pulse width modulation of the power signals maintained consistent output voltage levels regardless of the number of energized SMA wire eliminating the overheating of the SMA wires during low power draw motions. Besides preventing damage to the SMA wires, damage to the prongs was also reduced because SMA strains are reduced to the designed strain levels of 3-4%. In contrast, an overheated wire can strain in excess of 8% thus causing the prongs to deflect over twice as far as they were designed to handle.

The translation speed of the reduced-scale prototype was approximately 75% of that of the large-scale prototype. This reduction stems from the smaller step size of the reduced-scale prototype, 6.35 mm, compared to 17 mm for the large-scale prototype. Therefore, each cycle of the SMA wire produces only 6.35 mm of deflection, or approximately 37% of the deflection obtained per cycle with the large-scale prototype. However, the smaller 200 μm (8 mil) SMA wires can be cooled quicker due to their reduced thermal mass (1 second heating, 2.2 second cooling) thereby increasing an individual wire's bandwidth to approximately 0.3 Hz, triple that of the large-scale prototype. When the wires are configured in the distributed Active Velcro surface, the effective bandwidth is increased to approximately 0.55 Hz. Again, this gain is not due to the phased activation approach. Instead, an SMA wire is still energized on sequential steps, but is only partially cooled between steps. Using the phased activation approach speeds as high as 5 mm/s may be obtained.

The analytical model was analyzed to estimate the stresses generated throughout the two flexible elements of the mechanism: the prong column and the suspension line. As suspected the stresses in both the suspension line and the prong column exceeded the material's yield strength. Stress levels in the suspension line were estimated at 27% above the yield strength and in the prong column almost 10% above the yield strength of the Somos 8110 resin, thus explaining the presence of large plastic deformations observed in Figure 2.19b. While the yield strength of the Somos resin was exceeded, this was due to its very low strength of only 18 MPa. This material was used for the prototype because it was the material available at the time of the research. The maximum stress levels experienced by the current prototype are well below the yield strength of many materials such as brass, aluminum, steel and plastics such the polycarbonate, polyketone, or nylon series. However, the current Somos build material can still be used by designing a new host surface topology experiences stress levels below the 18 MPa yield strength during operation. Not surprisingly, fatigue failures were also observed during testing of the demonstration system. Utilizing the derived analytical models, a proposed host surface topology design was identified with stress levels below the yield strength of the Somos resin (Figure 2.32).

The newly proposed design was obtained through optimization to minimize the overall height of the host surface while minimizing the stress levels. Additional constraints were added to insure that the design could be fabricated using the relatively out of date SLA 250 stereolithography that this research had access to. Thus to insure reliable fabrication, the minimum feature size was limited to one mm. Even with the feature size limitation stress was

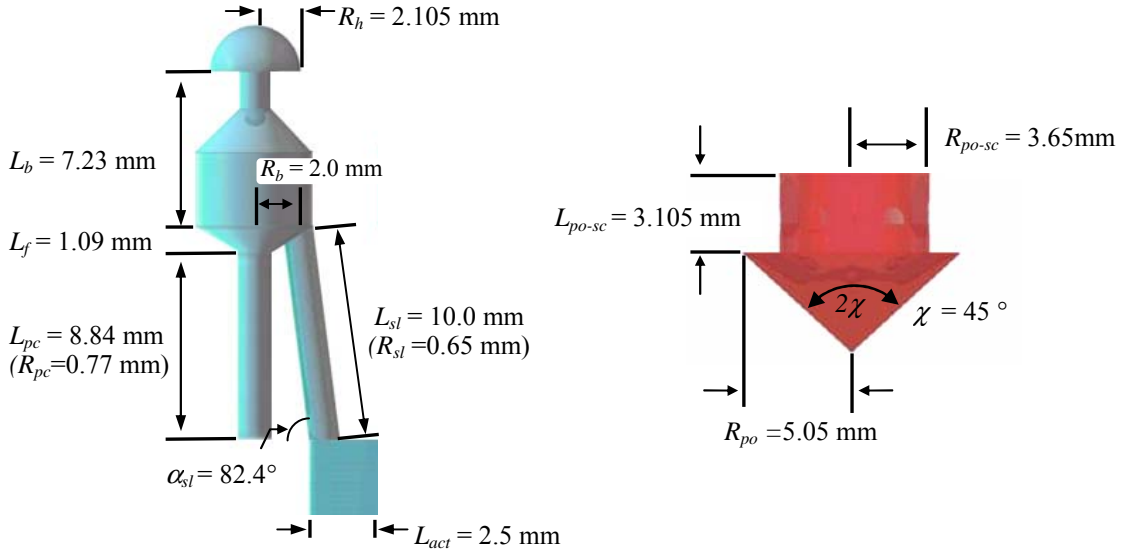


Figure 2.32: Refined Host Surface Topology. The current host surface topology experienced stress levels in excess of the build material yield strength. Stress levels at the base of the suspension lines exceeded the yield strength by 27% leading to plastic deformation during operation. A refined topology design was identified through optimization of the derived models to maximize the positioning force while limiting the maximum stress levels to the flexural strength of the Somos build resin (11 MPa). The proposed design is has up to 52% less stress while generating 36% more positioning force.

reduced by over 45% while increasing positioning force by 36% and the maximum carrying load by 25% (Table 2.4). Therefore a more compact design with increased positioning accuracy and reduced stress levels was obtained through topology changes alone without altering the build material or fabrication techniques demonstrating the usefulness of the models.

2.5. CONCLUSIONS

This research successfully laid the foundation for a unique technology that represents a paradigm shift in connection methodology. Smart Attachment Mechanisms or SAMs were introduced that have the ability to actively connection (engage, retain, release) and manipulate (translate, rotate) two surfaces. This is useful for any environment, such as low gravity, fluidic, vibration, etc, that requires connection simultaneously with motion generation. This research met three primary objectives: creation of new technology, development of predictive operational models and demonstration and evaluation of a Proof-Of-Concept system.

Active Velcro was invented during this effort as a “docking” mode SAM. The original motivation for this device was the autonomous docking of micro-/nano-satellites to a mother satellite in space. Active Velcro consists of two surfaces: an active host with SMA actuated compliant prongs arranged in cells and an inactive guest with a sparse arrangement of posts. These surfaces snap fit together and then translate/rotate upon energizing the SMA wires to position the guest surface relative to the host.

Table 2.4: Host Surface Refinement Results:

| | | | |
|--------------------------|--------|---------------------------|---------|
| Stress | | Geometry | |
| Prong Column - | ↓ 52 % | Prong Height - | ↑ 13% |
| Suspension Line - | ↓ 45 % | Motion Resolution - | ↑ 8.6 % |
| Performance | | Input Requirements | |
| Max. Carrying Load - | ↑ 25 % | Actuator Stroke - | ↑ 18 % |
| Max. Positioning Force - | ↑ 36 % | Actuator Force - | ↓ 5.6 % |

A quasi-static analytical model was developed to capture the complex behavior of the highly redundant compliant host surface mechanism. The model incorporated the post/prong geometry, three-dimensional flexure mechanism, friction at the post/prong interfaces and interactions between adjacent prong groupings. This is a generalized model and specific cases were highlighted for the main operating scenarios: engagement, retention and positioning force. While the primary model development was based upon a single-cell, the methodology to expand the model for multiple cells was provided with a three-cell example given.

Several experiments were conducted to progressively examine the accuracy of the derived models and the behavior of the Active Velcro technology. In free-deflection experiments, the analytical model captured the kinematics of single-cell host surfaces with an average error of only 1.7%. Two different test samples were employed, demonstrating the ability to tailor the input requirements of the mechanism to desired actuator specifications. The observed prong displacement was linear with respect to the actuation inputs, which is uncommon for high displacement, compliant mechanisms. The large displacements however did lead to as much as 23% plastic deformation. However, later optimization of the surfaces was able to reduce the stresses and eliminate this problem.

It was observed in both the engagement and retention experiments that the model captures the general shape of the response curve well. As designed, engagement occurs at a low force (< 0.58 N) even for non-ideal surfaces and the retention forces are significantly higher than the engagement forces, 3.7 - 5.4 times higher for the samples tested. Despite the post-processing methods created, irregularities in friction levels were observed in both the engagement and retention tests leading to errors on average of 19%. These frictional variances stemmed from the layered stereolithography fabrication method employed to build the test samples and was exasperated by the relatively thick minimum layer size of 150 μ m for the SLA-250/40 utilized in this research. In addition, the shapes of the heads of the post and prong were not ideal. In light of the manufacturing difficulties and unknown frictional surfaces, the model captured the overall performance well, typically within 9.8% for surfaces resembling the assumed post and prong connection topology shapes.

Multi-cell tests were performed to validate the model in the presence of cell interactions. The model was capable of capturing the positioning force with fewer than 3.5% error. Interestingly, it was demonstrated that the friction levels between the prongs and post have little impact on the available positioning forces. Even for a large level of friction ($\mu_l = 0.4$) the blocked positioning force drops only by 4.7% from the frictionless case. This is a result of the

Bohringer, K.F., Donald, B.R., Mihailovich, R., MacDonald, N.C., 1994, "A Theory of Manipulation and Control for Microfabricated Actuator Arrays," in *Proc. of the IEEE Workshop on Micro Electro Mechanical Systems*, Jan. 25-28, pp 102 – 107.

Bohringer, K.F., Suh, J.W., Donald, B.R., Darling, R.B., Kovacs, G.T.A., 1997, "Vector Fields for Task-level Distributed Manipulation: Experiments with Organic Micro Actuator Arrays," in *Proc. of the IEEE Conference on Robotics and Automation*, Albuquerque, NM, April 20-25, Vol. 2, pp 1779 – 1786.

Clement, J.W. and Brei, D.E., 2001, "Proof-of-Concept Investigation of Active Velcro for Smart Attachment Mechanisms," in *Proc. of the 42nd AIAA/ASME/ASCE/AHS/ASC Structures, Structural Dynamics, and Materials Conference*, Seattle, WA.

Ebefors, T., Mattsson, J.U., Kalvesten, E., Stemme, G., 1999, "A Robust Micro Conveyer Realized by Arrayed Polyimide Joint Actuators," in *Proc. of the IEEE International Conference on Micro Electro Mechanical Systems*, Jan. 17-21, pp 576 – 581.

Hart, P.E., Nilsson, N.J., Raphael, B., 1968, "A Formal Basis for the Heuristic Determination of Minimum Cost Paths," *IEEE Transactions of Systems Science and Cybernetics*, July, Vol. 4, No. 2, pp 100-107.

Iizuka, T., Fujita, H., 1997, "Precise Positioning of a Micro Conveyor Based on Superconducting Magnetic Levitation," in *Proc. of the IEEE International Symposium on Micromechatronics and Human Science*, Oct. 5-8, pp 131 – 135.

Konishi, S., Fujita, H., 1994, "A Conveyance System Using Air Flow Based on the Concept of Distributed Micro Motion Systems," *Journal of Microelectromechanical Systems*, June, Vol. 3, No. 2, pp 54 - 58.

Langlet, P., Collard, D., Akiyama, T., Fujita, H., 1997, "A Quantitative Analysis of Scratch Drive Actuation for Integrated X/Y Motion System," *International Conference on Solid State Sensors and Actuators*, June 16-19, Vol. 2, pp 773 – 776.

Luntz, J.E., Messner, W., and Choset, H., 1999a, "Discrete Actuator Array Vectorfield Design for Distributed Manipulation," in *Proc. of the IEEE Conference on Robotics and Automation*, Detroit, MI, May 10-15, Vol. 3, pp 2235 - 2241.

Luntz, J.E., Messner, W., and Choset, H., 1999b, "Open-Loop Orientability of Objects on Actuator Arrays," in *Proc. of the IEEE Conference on Robotics and Automation*, Detroit, MI, May 10-15, Vol. 3, pp 2242 - 2248.

Luntz, J.E., Messner, W., and Choset, H., 2000, "Closed-Loop Operation of Actuator Arrays," in *Proc. of the IEEE Conference on Robotics and Automation*, San Francisco, CA, April 24-28, Vol. 4, pp 3666 – 3672.

Nakazawa, H., Watanabe, Y., Morita, O., Edo, M., Yonezawa, E., 1997, "The Two-Dimensional Micro Conveyer: Principles and Fabrication Process of the Actuator," *International Conference on Solid State Sensors and Actuators*, June 16-19, Vol. 1, pp 33 – 36.

Pestel, E.C. and Leckie, F.A., 1963, "Matrix Methods in Elastomechanics," McGraw Hill Publishing Co., Inc., New York.

Suh, J.W., Darling, R.B., Bohringer, K.F., Donald, B.R., Baltes, H., Kovacs, G.T.A., 1999, "CMOS Integrated Ciliary Actuator Array as a General-Purpose Micromanipulation Tool for Small Objects," *Journal of Microelectromechanical Systems*, Dec, Vol. 8, No. 4, pp 483 – 496.

Tadokoro, S., Fuji, S., Fushimi, M., Kanno, R., Kimura, T., Takamori, T., Oguro, K., 1998, "Development of a Distributed Actuation Device Consisting of Soft Gel Actuator Elements," *in Proc. of the IEEE Conference on Robotics and Automation*, Leuven, Belgium, May 16-20, Vol. 3, pp 2155 – 2160.

Yim, M, Duff, D.G., Roufas, K.D., 2000, "PolyBot: a Modular Reconfigurable Robot," *in Proc. of the IEEE Conference on Robotics and Automation*, San Francisco, CA, April 24-28, Vol. 1, pp 514 – 520.

SECTION 3. PUBLICATIONS, TECHNICAL REPORTS, AND INVENTIONS

Papers submitted or published under ARO sponsorship during this reporting period.

(a) Papers published in peer-reviewed journals

Bharti, S., and Frecker, M., 2003, "Optimal Design and Experimental Characterization of a Compliant Mechanism Piezoelectric Actuator for Inertially Stabilized Rifle," *Journal of Intelligent Material Systems and Structures* (in press).

(b) Papers published in non-peer-reviewed journals or in conference proceedings

Bharti, S., and Frecker, M., 2002, "Topology Optimization and Detailed Finite Element Modeling of Piezoelectric Actuators: Effect of External Loads and Detail Geometry on Actuator Output," *SPIE 9th International Symposium on Smart Structures and Materials*. San Diego, California.

Bharti, S., and Frecker, M., 2003, "Compliant Mechanical Amplifier Design Using Multiple Optimally Placed Actuators," *ASME International Mechanical Engineering Congress and Exposition, Adaptive Structures Symposium*, Washington, DC, pp. 16-21.

Brei, D., Vendlinski, J., Frecker, M., and Bharti, S., 2003, "Actuation Development and Evaluation for INSTAR Inertially Stabilized Rifle," *SPIE 10th International Symposium on Smart Structures and Materials*, San Diego, California.

Brei, D., Vendlinski, J., Lindner, D.K., Zhu, H., and LaVigna, C., 2003. "Development and Demonstration of INSTAR Inertially Stabilized Rifle," *SPIE 10th International Symposium on Smart Structures and Materials*, San Diego, California.

Clement, J.W. and Brei, D., 2001, "Proof-of-Concept Investigation of Active Velcro for Smart Attachment Mechanisms," *AIAA-01-1503, 42nd AIAA/ASME/ASCE/AHS/ASC Structures, Structural Dynamics and Materials Conference and Exhibit*, Long Beach, CA, Vol. 4, pp. 2388-2398.

Clement, J.W. and Brei, D., 2003, "Force-Deflection Behavior of a Smart Attachment Mechanism," *AIAA-03-1638, 44th AIAA/ASME/ASCE/AHS/ASC Structures, Structural Dynamics and Materials Conference and Exhibit*, Norfolk, VA.

Frecker, M., and Bharti, S., 2001, "Toward the Design of Compliant Actuators with a Specified Force and Stroke," *Proceedings 2001 ASME Design Engineering Technical Conferences*, DETC2001/DAC-21054, Pittsburgh, PA.

Lindner, D.K., Brei, D., and LaVigna, C., 2001, "Intertially Stabilized Rifle Using Active Compliant Transmissions," *Proceedings of the 16th Annual Technical Meeting of the American Society for Composites*, Blacksburg, VA.

Lindner, D.K., 2001, "Efficient Amplifiers for Smart Structure Actuators," *Proceedings of the Canada-US CanSmart Workshop on Smart Materials and Structures*, Montreal, Quebec, Canada, pp. 69-75.

Lindner, D.K., Zhu, H., Song, C., Huang, W., Cheng, D., 2002, "Low Input Voltage Switching Amplifiers for Piezoelectric Actuators," *Proceedings of SPIE's 2002 North American Symposium on Smart Structures and Materials: Industrial and Commercial Applications of Smart Structures Technologies*, San Diego, CA.

Lindner, D.K., Brei, D., and LaVigna, C., 2002, "Intertially Stabilized Rifle Using Smart Materials," *Proceedings of the European Workshop on Smart Structures in Engineering and Technology*, SPIE Vol. 4763, Presqu'ile de Giens, France, pp. 95-100.

Lindner, D.K., Zhu, H., Brei, D., Vindlinski, J., LaVigna, C., 2002, "Internally Stabilized Rifle Using Recurve Actuators," *Proceeding of 2002 ASME International Mechanical Engineering Congress & Exposition*, New Orleans, LA.

(c) Papers presented at meetings, but not published in conference proceedings

None

(d) Manuscripts submitted, but not published

Bharti, S., and Frecker, M., 2003, "Compliant Mechanical Amplifier Design Using Multiple Optimally Placed Actuators," Submitted to *Journal of Intelligent Material Systems and Structures* (9/03).

(e) Technical reports submitted to ARO

Brei, D., and Clement, J.W., 2001, "Proof-of-Concept Investigation of Active Velcro for Smart Attachment Mechanisms," Final Report II, pp. 1-51.

Brei, D., and Clement, J.W., 2002, "Proof-of-Concept Investigation of Active Velcro for Smart Attachment Mechanisms," Final Report III, pp. 1-48.

Brei, D., Lindner, D.K., Frecker, M. and LaVigna, C., 2001, "Electrically Integrated Active Compliant Transmission (ACT) Actuation Technologies," Progress Report.

Inventions during this reporting period.

Brei, D. and Clement, J. W., 2001, "Attachment Mechanism," US Patent 09/847,373, Filed September 13, 2001.

SECTION 4. SCIENTIFIC PERSONNEL

This grant has supported the following students/support level:

James Vendlinski, University of Michigan, 50% research assistantship, graduated with a Masters in mechanical engineering

Ganesh Balasubramanian, University of Michigan, 50% research assistantship, graduated with a Masters in mechanical engineering

Tony Lin, University of Michigan, 50% research assistantship, graduated with a Masters in mechanical engineering

Joseph Clement, University of Michigan, 50% research assistantship, Ph.D. Candidate

Smita Bharti, Pennsylvania State University, 50% research assistantship, graduated with a Masters in mechanical engineering

Danling Cheng, Virginia Tech, 100% research assistantship

Weixing Huang, Virginia Tech, 50% research assistantship